Máster en Matemática Industrial

2019 – 2020

Trabajo Fin de Máster

Modeling and reconstruction of Temperature, Wind, and Atmospheric Pressure fields in a 2D area from the information provided by the cartography of the interested region.

Fabián Milián Echazábal

Fecha presentación: 20 de julio
Tutor/a académico/a: Andrés Prieto Aneiros
Empresa: Microflown Technologies
Tutor/a empresa: Graciano Carrillo Pousa

Contents

Abstract

In the present work, the temperature, wind, and atmospheric pressure fields were calculated in a two-dimensional area by using a model for laminar and incompressible flow with heat transfer. The Navier-Stokes and energy equations were numerically solved by using finite element methods with Fenics, which is an open-source computing platform for solving partial differential equations. The computational domains were generated with Gmsh; an open-source finite element mesh generator with a built-in CAD engine and post-processor. The code was validated by comparing the finite element solutions with known problems studied by other authors. More complex domains were generated from a topography dataset provided by OpenTopography and the code was run imposing more realistic boundary conditions, such as velocity and temperature profiles. A workflow was developed to show the steps to generate the physical domain from a dataset since, together with a Python script, it solves the model for laminar and incompressible flow with heat transfer in the selected area.

Chapter 1

Introduction

Microflown Technologies is a Dutch company that developed a particle velocity sensor in 1994, which is an acoustic sensor. It is the first sensor in the world that allows to directly measure particle velocity as a physical quantity. The particle velocity sensors can be used as extremely compact Acoustic Vector Sensors (AVS), capable of detecting, localising, identifying and tracking sound sources in 3D space.

At any point in space, a sound field can be described completely by its two quantities; the scalar value, and the vector value. The scalar value, sound pressure, is well known and well measured. But the other quantity in acoustics, the vector value acoustic particle velocity, only recently became a directly measurable quantity with the invention of the Microflown sensor.

In this context, it is necessary to study the propagation of sound in air, emphasizing the parameters that affect its propagation. The propagation of sound in air is affected by the wind velocity and sound speed in the atmosphere, which depends on the temperature, ratio of specific heats, the gas constant, and specific humidity. Also, the absorption coefficient is very important in wave propagation depending on the temperature, humidity, acoustic frequency, and atmospheric pressure.

Microflown Technologies has proposed this project, in order to get important properties of a specific area, such as the velocity, pressure, and temperature fields. These results will be used in later works to study the propagation of acoustic waves. As a contact person in the company, Graciano Carrillo Pousa has been appointed and as the tutor of the project, Andrés Prieto Aneiros.

1.1 Objectives

The main objective is to provide the company with a Python script capable of numerically solve the Navier-Stokes, and the conservation of energy equations in a computational domain, given by the cartography data. These equations need to be solved with a set of boundary conditions. In this case, the fluid is air and it will be imposed that there will be no appreciable changes in density. The problem to solve is a laminar and incompressible flow model coupled with the temperature. Boussinesq approximation will be also implemented, which states that the mass density is constant except in the buoyancy term present in the Navier-Stokes equations.

An important goal of this work is to provide a workflow for the company to correctly solve the velocity, pressure, and temperature fields in any two-dimensional region, regardless of terrain difficulty. This workflow will detail how to extract spatial data such as latitude, longitude, and altitude from a GeoTIFF file [26] (which can also include data such as temperature profile, pressure profile, and others) to create the physical domain where the calculations will be made.

1.2 Overview

Chapter 2 gives an overview of the governing equations to model the behavior of laminar and incompressible flow with heat transfer. In addition, the boundary conditions involved in each problem to be solved will be described, as well as the variational formulation of the problem. Chapter 3 will show the discrete methods used in this work to find an approximate solution to the variational problem using the finite element method. Furthermore, Newton's method will be used to linearize the convective terms present in the resulting nonlinear system of equations. An algorithm will be shown in a schematic that summarizes the fully-discretized problem of the model for laminar and incompressible flow with heat transfer. Numerical validations will be discussed in Chapter 4, where four different studies will be considered for the two-dimensional case and one study for the three-dimensional case. The tests will be of forced, mixed, and natural convection. The results will be discussed and compared with those obtained by previous authors. In Chapter 5, the velocity, pressure, and temperature fields were calculated for four scenarios using more realistic velocity and temperature profiles. For the last scenario, the physical domain consisted of a set of actual altitude data obtained from a GeoTIFF data file. A workflow diagram is shown that explains the step-by-step process for creating the physical domain, obtaining the velocity, pressure, and temperature fields, as well as display results. Finally, in Chapter 6 the present work then concludes with a summary and suggestions for future work.

Chapter 2

Mathematical models

The Navier–Stokes and energy equations are the governing equations of the fluid flow. They model the conservation of mass, momentum, and energy describing how the velocity, pressure, temperature, and density of the fluid are related. In this Chapter, a nondimensional system of partial differential equations will be shown to model the behavior of laminar and incompressible flow with heat transfer.

2.1 Navier-Stokes equations

The motion of fluids is governed by the Navier-Stokes equations, which can be seen as Newton's second law of motion for fluids. These equations can be written as (see [28] for a detailed discussion)

$$\rho\left(\frac{\partial \mathbf{u}}{\partial t} + (\mathbf{u}\cdot\nabla)\,\mathbf{u}\right) = -\nabla p + \mathbf{div}\,\tau + \rho\mathbf{g}, \tag{2.1}$$

where ρ is the fluid mass density, μ is the dynamic viscosity, $\mathbf{g}$ is the acceleration of gravity, $\mathbf{u}$ is the fluid velocity vector, and p is the fluid pressure. The viscous stress tensor is denoted by

$$\tau = \mu\left[\nabla\mathbf{u} + (\nabla\mathbf{u})^T - \frac{2}{3}(\operatorname{div}\mathbf{u})\,\mathbf{I}\right], \tag{2.2}$$

where $\mathbf{I}$ is the unit matrix.

These equations are always solved together with the continuity equation. The Navier-Stokes equations represent (2.1)-(2.2) the conservation of momentum, while the continuity equation represents the conservation of mass

$$\frac{\partial \rho}{\partial t} + \operatorname{div}(\rho\mathbf{u}) = 0. \tag{2.3}$$

2.2 Laminar and incompressible flow

For an incompressible flow, there will be no appreciable changes in the mass density, so it can be assumed that $\rho = \rho_0$. Hence, the continuity equation (2.3) yields to [7]

$$\operatorname{div}\mathbf{u} = 0.$$

For a low Reynolds number, the flow will be laminar and it will no be necessary to use a turbulence model. The Navier-Stokes equations (2.1)-(2.2) for laminar and incompressible flow reduce to

$$\rho\left(\frac{\partial \mathbf{u}}{\partial t} + (\mathbf{u}\cdot\nabla)\,\mathbf{u}\right) = -\nabla p + \mu\operatorname{div}\epsilon(\mathbf{u}) + \rho\mathbf{g}.$$

where $\epsilon(\mathbf{u})$ is the strain-rate tensor denoted as

$$\epsilon(\mathbf{u}) = \frac{1}{2}\left(\nabla u + (\nabla u)^T\right).$$

2.3 Boussinesq approximation

Boussinesq approximation will be also implemented, which states that the mass density can be assumed constant except in the buoyancy term $\rho\mathbf{g}$, present in the Navier-Stokes equations. The mass density is replaced by a constant ρ_0 in the inertial term, being ρ_0 the reference value for the mass density; and by $(\rho_0 + \delta\rho)\mathbf{g}$ in the buoyancy term

$$\rho_0\left(\frac{\partial \mathbf{u}}{\partial t} + (\mathbf{u}\cdot\nabla)\,\mathbf{u}\right) = -\nabla p + \mu\,\mathrm{div}\,\epsilon(\mathbf{u}) + (\rho_0 + \delta\rho)\,\mathbf{g},$$
$$\delta\rho\mathbf{g} = (\rho - \rho_0)\,\mathbf{g} = -\rho_0\beta\,(T - T_0)\,\mathbf{g},$$

where $\delta\rho$ is the mass density variation with respect to ρ_0, β is the coefficient of thermal expansion, and T_0 is the reference temperature. Finally, the Navier-Stokes equations for laminar and incompressible flow are expressed by

$$\rho_0\left(\frac{\partial \mathbf{u}}{\partial t} + (\mathbf{u}\cdot\nabla)\,\mathbf{u}\right) = -\nabla p + \mu\,\mathrm{div}\,\epsilon(\mathbf{u}) + \rho_0\mathbf{g} - \rho_0\beta\,(T - T_0)\,\mathbf{g}.$$

2.4 Conservation of energy

To calculate the temperature field, we must solve the Navier-Stokes and the continuity equations by coupling the conservation of energy [7]

$$\rho C_p\frac{\partial T}{\partial t} + \rho C_p\,(\mathbf{u}\cdot\nabla T) = \mathrm{div}\,(\kappa\nabla T) + Q + \Phi,$$

being C_p the specific heat at constant pressure, κ the thermal conductivity, Q the internal energy generation, and Φ the viscous dissipation. It will be considered that there will be no internal heat generation and the viscous dissipation effects will be neglected. The mass density is replaced by the reference mass density following analogous arguments used in the Boussinesq approximation. Then, the conservation of energy can be expressed as

$$\frac{\partial T}{\partial t} + \mathbf{u}\cdot\nabla T = \alpha\Delta T,$$

where α is the thermal diffusivity

$$\alpha = \frac{\kappa}{\rho_0 C_p}.$$

2.5 Model for laminar and incompressible flow with heat transfer

Finally, the system of partial differential equations [17] to solve is

$$\mathrm{div}\,\mathbf{u} = 0, \tag{2.4}$$
$$\frac{\partial T}{\partial t} + \mathbf{u}\cdot\nabla T = \alpha\Delta T, \tag{2.5}$$
$$\rho_0\left(\frac{\partial \mathbf{u}}{\partial t} + (\mathbf{u}\cdot\nabla)\,\mathbf{u}\right) = -\nabla p + \mu\,\mathrm{div}\,\epsilon(\mathbf{u}) + \rho_0\mathbf{g} - \rho_0\beta\,(T - T_0)\,\mathbf{g}, \tag{2.6}$$

where $\mathbf{u}$, p and T are the unknowns to be solved.

The equations (2.4)-(2.6) can be written in the Eulerian frame of reference, with indices $i, j = 1, 2, 3$, and applying the Einstein convention [28] on repeated indices

$$\begin{aligned}
&\frac{\partial u_i}{\partial x_i} = 0, \\
&\frac{\partial T}{\partial t} + u_j \frac{\partial T}{\partial x_j} = \alpha \frac{\partial}{\partial x_j}\left(\frac{\partial T}{\partial x_j}\right), \\
&\rho_0 \left(\frac{\partial u_i}{\partial t} + u_j \frac{\partial u_i}{\partial x_j}\right) = -\frac{\partial p}{\partial x_i} + \mu \frac{\partial}{\partial x_j}\left(\frac{\partial u_i}{\partial x_j} + \frac{\partial u_j}{\partial x_i}\right) + \rho_0 g_i - \rho_0 g_i \beta \left(T - T_0\right),
\end{aligned}$$

for $i = 1, 2, 3$.

These equations will be expressed in a more efficient way to reduce the number of parameters and increase the usefulness of the solutions. This can be accomplished by nondimensionalizing the system (2.4)-(2.6) and their boundary conditions. The flow properties will be taken as references to define dimensionless variables.

Let U be denoted as the reference velocity, L as the reference length, and the properties of the fluid $(p_0, \rho_0, T_0, \mu_0, \alpha_0)$ as reference properties. Thus, dimensionless variables can be defined as

$$\begin{aligned}
x_i^* &= \frac{x_i}{L}, \qquad & t^* &= \frac{tU}{L}, \qquad & u_i^* &= \frac{u_i}{U}, \qquad & p^* &= \frac{p - p_0}{\rho_0 U^2}, \\
\rho^* &= \frac{\rho}{\rho_0}, \qquad & \mu^* &= \frac{\mu}{\mu_0}, \qquad & \alpha^* &= \frac{\alpha}{\alpha_0}, \qquad & T^* &= \frac{T - T_0}{T_\mathrm{w} - T_0},
\end{aligned} \tag{2.7}$$

where T_w denotes another reference temperature, so the temperature difference $(T_\mathrm{w} - T_0) > 0$ will be the final temperature reference.

The dimensionless variables (2.7) are substituted into the system (2.4)-(2.6) resulting in the following nondimensional equations of motion

$$\frac{\partial u_i^*}{\partial x_i^*} = 0, \tag{2.8}$$

$$\frac{\partial T^*}{\partial t^*} + u_j^* \frac{\partial T^*}{\partial x_j^*} = \frac{1}{\mathrm{Re}\,\mathrm{Pr}} \frac{\partial}{\partial x_j^*}\left(\frac{\partial T^*}{\partial x_j^*}\right), \tag{2.9}$$

$$\frac{\partial u_i^*}{\partial t^*} + u_j^* \frac{\partial u_i^*}{\partial x_j^*} = -\frac{\partial p^*}{\partial x_i^*} + \frac{1}{\mathrm{Re}} \frac{\partial}{\partial x_j^*}\left(\frac{\partial u_i^*}{\partial x_j^*} + \frac{\partial u_j^*}{\partial x_i^*}\right) + \frac{1}{\mathrm{Fr}} g_i^* \left(1 - T^*\right), \tag{2.10}$$

where the superscript $(^*)$ will be removed to ease the reading of equations. The Reynolds number (Re), Prandtl number (Pr), Froude number (Fr), Grashof number (Gr), and Rayleigh number (Ra) have been defined by

$$\begin{aligned}
\mathrm{Re} &= \frac{\rho_0 U L}{\mu_0}, \\
\mathrm{Pr} &= \frac{\mu_0 C_p}{\kappa}, \\
\mathrm{Fr} &= \frac{U^2}{gL}, \\
\mathrm{Gr} &= \frac{g\beta\rho_0^2 (T_w - T_0) L^3}{\mu_0^2}, \\
\mathrm{Ra} &= \frac{g\beta\rho_0 (T_w - T_0) L^3}{\mu_0 \alpha_0}.
\end{aligned}$$

These dimensionless numbers are related by

$$\mathrm{Ra} = \mathrm{Gr}\,\mathrm{Pr}, \qquad \mathrm{Fr} = \mathrm{Re}^2\,\mathrm{Gr}^{-1}, \qquad \mathrm{Ri} = \mathrm{Gr}\,\mathrm{Re}^{-2}, \tag{2.11}$$

where Ri is the Richardson number.

2.6 Boundary conditions

Boundary conditions of four different studies will be considered for the two-dimensional case, and the fourth study also for a three-dimensional case. Notice that all boundary conditions will be taken as dimensionless.

Forced and mixed convection flow past a heated circular cylinder will be the first tests to be computed. Finally, the last test will be referred to natural convection in a square enclosure with a circular cylinder. These tests will be analyzed in-depth in the Chapter 4. Dimensionless boundary conditions will be the same for almost all configurations, except in some cases that will be specified.

The velocity, pressure, and temperature fields are set to 0 at all points in the domain. Uniform flow is imposed at the inlet, where the horizontal velocity component is set to $u = 1$ for cases that refer to forced and mixed convection flow past a heated circular cylinder. The vertical velocity component is set to $v = 0$, which will also be set to zero for the entire domain. Also, an uniform temperature profile is set as $T = 0$ at the inlet for all these cases. At the top and bottom walls, symmetry boundary conditions are imposed, setting the velocity and temperature gradients to $v = \partial u/\partial y = \partial T/\partial y = 0$. At the outlet, the pressure, velocity gradient and temperature gradient are set to $v = p = \partial u/\partial x = \partial T/\partial x = 0$. Finally, at the surfaces of the obstacles, the no-slip condition $u = v = 0$ and a uniform temperature $T_{\mathrm{w}} = 1$ will be imposed.

For the case of natural convection in a square enclosure with a circular cylinder for the two-dimensional case, at the walls and at the cylinder surface, the no-slip condition will be imposed: $u = v = 0$. The hot wall temperature is imposed on the cylinder surface: $T_h = 1$, and the cold wall temperature is imposed on the walls of the square enclosure: $T_c = 0$. For the three-dimensional case, now it will be 6 walls instead of 4 walls and the velocity w for the z-component will be added. At the walls and at the cylinder surface, the no-slip condition will be imposed: $u = v = w = 0$. The hot wall temperature is imposed on the cylinder surface: $T_h = 1$, and the cold wall temperature is imposed on the walls of the square enclosure: $T_c = 0$.

2.7 Variational formulation

The system (2.8)-(2.10) can be rewritten using (2.11). Similar arguments to those ones used in references [8],[17] will be used in what follows. Firstly, from the original system of equations:

$$\mathrm{div}\,\mathbf{u} = 0, \tag{2.12}$$

$$\frac{\partial T}{\partial t} + \mathbf{u}\cdot\nabla T = \frac{1}{\mathrm{Re}\,\mathrm{Pr}}\Delta T, \tag{2.13}$$

$$\frac{\partial \mathbf{u}}{\partial t} + (\mathbf{u}\cdot\nabla)\,\mathbf{u} - \frac{2}{\mathrm{Re}}\,\mathrm{div}\,\epsilon(\mathbf{u}) + \nabla p = -\frac{\mathrm{Gr}}{\mathrm{Re}^2}T\mathbf{g}. \tag{2.14}$$

Let Ω denote the spatial domain, and $\Gamma = \partial\Omega$ the boundary of Ω. Then, the boundary conditions [8],[16] to consider are

$$\begin{aligned} \mathbf{u} &= \mathbf{u}_D && \text{on } \Gamma_D^{\mathbf{u}}, \\ T &= T_D && \text{on } \Gamma_D^{T}, \\ \sigma \cdot \mathrm{n} &= \sigma_N && \text{on } \Gamma_N^{\mathbf{u}}, \\ \alpha \nabla T \cdot \mathrm{n} &= g_N && \text{on } \Gamma_N^{T}, \end{aligned} \tag{2.15}$$

where the subscript D and N denote the Dirichlet and Neumann boundary data respectively, such that $\partial\Omega = \partial\Omega_D \cup \partial\Omega_N$, with $\partial\Omega_D \cap \partial\Omega_N = \emptyset$. At the boundary, $\mathbf{u}_D$ is the velocity, T_D the temperature, g_N the heat flux, and σ_N the stress vector or traction, being $\sigma = 2\mu\epsilon(\mathbf{u}) - p\mathbf{I}$ and n the outward unit normal at the boundary.

It is necessary to define some functional spaces to write the system (2.12)-(2.14) as a finite element variational problem. The test function spaces [11] will be defined as follows

$$\begin{aligned} \hat{V} &= \{v \in H^1(\Omega) : v = 0 \ \text{ on } \partial\Omega\}, \\ \hat{E} &= \{\eta \in H^1(\Omega) : \eta = 0 \ \text{ on } \partial\Omega\}, \\ \hat{Q} &= L^2(\Omega), \end{aligned}$$

with $H^1(\Omega)$ denoting the well-known Sobolev space where functions v, v^2, $|\nabla v|^2$ have finite root mean-square over Ω and the space $L^2(\Omega)$ is a function $f : \Omega \to \mathbb{R}$ that is square-integrable, which means that the integral of $|f|^2$ is finite. The trial function spaces [8] will be defined as

$$\begin{aligned} V &= \{v \in H^1(\Omega) : v = u_D \ \text{ on } \partial\Omega\}, \\ E &= \{\eta \in H^1(\Omega) : \eta = T_D \ \text{ on } \partial\Omega\}, \\ Q &= \{q \in L^2(\Omega) : \int_\Omega q \, \mathrm{d}\Omega = 0, \ \text{ if } \Gamma_N^{\mathbf{u}} = \emptyset\}, \end{aligned}$$

Now the test function space can be defined as Q for the pressure field, E for temperature field, and $\mathbf{V} = V \times V$ for the velocity field in the two-dimensional case, or $\mathbf{V} = V \times V \times V$ in the three-dimensional case. Considering the relationships (2.11), it will be introduced the following multilinear forms to write the variational formulation of the boundary-value problem (2.12)-(2.15)

$$a(\mathbf{u}, \mathbf{v}) = \frac{2}{\mathrm{Re}} \int_\Omega \epsilon(\mathbf{u}) : \epsilon(\mathbf{v}) \, \mathrm{d}\Omega, \tag{2.16}$$

$$b(q, \mathbf{v}) = \int_\Omega q \, \mathrm{div}\, \mathbf{v} \, \mathrm{d}\Omega, \tag{2.17}$$

$$c(\mathbf{u}, \mathbf{v}) = \int_\Omega \left[(\mathbf{u} \cdot \nabla)\, \mathbf{u}\right] \cdot \mathbf{v} \, \mathrm{d}\Omega, \tag{2.18}$$

$$d(\eta, \mathbf{v}) = \mathrm{Ri} \int_\Omega \eta \hat{\mathbf{g}} \, \mathrm{d}\Omega, \tag{2.19}$$

$$e(T, \eta) = \frac{1}{\mathrm{Re}\,\mathrm{Pr}} \int_\Omega \nabla T \cdot \nabla \eta \, \mathrm{d}\Omega, \tag{2.20}$$

$$\beta(\mathbf{u}, T, \eta) = \int_\Omega \eta \mathbf{u} \cdot \nabla T \, \mathrm{d}\Omega, \tag{2.21}$$

$$\gamma(\mathbf{v}) = \int_{\Gamma_N^{\mathbf{u}}} \sigma_N \cdot \mathbf{v} \, \mathrm{d}\Gamma, \tag{2.22}$$

$$\lambda(\eta) = \int_{\Gamma_N^{T}} \eta g_N \, \mathrm{d}\Gamma, \tag{2.23}$$

where $\mathbf{u} \in \mathbf{V}$, $p \in Q$, $T \in E$, $\mathbf{v} \in \hat{V}$, $q \in \hat{Q}$, and $\eta \in \hat{V}$. The vector $\hat{\mathbf{g}}$ in $d(\eta, \mathbf{v})$ denotes the normalized acceleration vector due to gravity.

The variational formulation of the problem (2.12)-(2.14) can be written as follows: Assuming that the unknown fields are smooth in time, for each fixed time t, find $(\mathbf{u}(t,\cdot), p(t,\cdot), T(t,\cdot)) \in \mathbf{V} \times Q \times E$, such that

$$b(q, \mathbf{u}) = 0, \tag{2.24}$$

$$\left(\frac{\partial T}{\partial t}, \eta\right) + \beta\left(\mathbf{u}, T, \eta\right) + e\left(T, \eta\right) = \lambda(\eta), \tag{2.25}$$

$$\left(\frac{\partial \mathbf{u}}{\partial t}, \mathbf{v}\right) + c\left(\mathbf{u}, \mathbf{v}\right) + a\left(\mathbf{u}, \mathbf{v}\right) - b\left(p, \mathbf{v}\right) + d\left(T, \mathbf{v}\right) = \gamma(\mathbf{v}), \tag{2.26}$$

for all $\mathbf{v} \in \hat{\mathbf{V}}$, $q \in \hat{Q}$, $\eta \in \hat{E}$, and the initial values $\mathbf{u}^0$, p^0, T^0 are known.

Chapter 3

Discrete methods

The Navier-Stokes and the continuity equations (2.6) and (2.4) respectively, will be numerically solved to calculate the velocity and pressure field by applying the Crank Nicolson scheme. These equations will also be coupled with the conservation of energy (2.5) to obtain the temperature field. In this section, an algorithm for the numerical simulation of the system (2.4)-(2.5) will be presented, which will be based on Prof. Jaroslav Hron implementation [12] using FEniCS [18]. The implementation was improved by making it possible for the code to compute not only forced convection problems but also mixed and natural convection problems. This was accomplished by coupling the Navier Stokes equations with the conservation of energy equation using the Boussinesq approximation. Also, the code allows reading any computational domain and is capable of identifying all the subdomains involved, which makes it easier to assign the boundary conditions.

3.1 Time semi-discretization

Let $\mathbf{x}(t)$ be a functional field depending on time, which is solution of the following nonlinear time-dependent differential equations [8]

$$\frac{\partial \mathbf{x}}{\partial t} = F\left(\mathbf{x}, t\right).$$

This system can be approximated numerically by using the θ-Method time-marching scheme of the form

$$\frac{1}{\Delta t}\left(\mathbf{x}^n - \mathbf{x}^{n-1}\right) = \theta F\left(\mathbf{x}^n, t^n\right) + (1-\theta) F\left(\mathbf{x}^{n-1}, t^{n-1}\right), \tag{3.1}$$

In this equation, $\theta \in [0,1]$ denotes the implicitness parameter. The time derivative has been approximated using backward difference formula, where $\mathbf{x}^n$ is a simpler way of expressing $\mathbf{x}(t^n)$, being $t^n = n\Delta t$ and Δt the time step for a uniform partition $[0,\tau]$, with $\tau > 0$ denoting the final time.

In the present work, calculations will be made for $\theta = 0.5$ known as the Crank Nicolson scheme [29], which is consistent with second-order consistency, unconditionally stable, and therefore convergent with second-order accuracy. This scheme has been used to solve convection-diffusion problems, and many authors have demonstrated its stability and convergence, as can be demonstrated in Wei and Liang's work [22].

The θ-Method (3.1) will be applied to system (2.24)-(2.26) to calculate $\mathbf{u}^n$, p^n, T^n at each time level

t^n, which are the velocity, pressure, and temperature fields respectively

$$b(q, \mathbf{u}^n) = 0, \tag{3.2}$$

$$\begin{aligned}\frac{1}{\Delta t}\left(T^n - T^{n-1}, \eta\right) &+ \theta\beta\left(\mathbf{u}^n, T^n, \eta\right) + (1-\theta)\beta\left(\mathbf{u}^{n-1}, T^{n-1}, \eta\right) \\ &+ \theta e\left(T^n, \eta\right) + (1-\theta)e\left(T^{n-1}, \eta\right) = \theta\lambda^n\left(\eta\right) + (1-\theta)\lambda^{n-1}\left(\eta\right),\end{aligned} \tag{3.3}$$

$$\begin{aligned}\frac{1}{\Delta t}\left(\mathbf{u}^n - \mathbf{u}^{n-1}, \mathbf{v}\right) &+ \theta c\left(\mathbf{u}^n, \mathbf{v}\right) + (1-\theta)c\left(\mathbf{u}^{n-1}, \mathbf{v}\right) + \theta a\left(\mathbf{u}^n, \mathbf{v}\right) + (1-\theta)a\left(\mathbf{u}^{n-1}, \mathbf{v}\right) \\ &- \theta b\left(p^n, \mathbf{v}\right) - (1-\theta)b\left(p^{n-1}, \mathbf{v}\right) + \theta d\left(T^n, \mathbf{v}\right) + (1-\theta)d\left(T^{n-1}, \mathbf{v}\right) \\ &= \theta\gamma^n\left(\mathbf{v}\right) + (1-\theta)\gamma^{n-1}\left(\mathbf{v}\right),\end{aligned} \tag{3.4}$$

for all $\mathbf{v} \in \hat{\mathbf{V}}$, $q \in \hat{Q}$, $\eta \in \hat{E}$, and the initial values $\mathbf{u}^0$, p^0, T^0 are known.

3.2 Finite element approximation

The continuous problem (3.2) - (3.4) defines the solution $(\mathbf{u}^n, p^n, T^n)$ in the infinite-dimensional function space $\mathbf{V} \times Q \times E$. To find an approximate solution of this variational problem it is necessary to apply the finite element method, with which the spaces $V, \hat{V}, Q, \hat{Q}, E, \hat{E}$ and $\mathbf{V}, \hat{\mathbf{V}}$ will be replaced by the finite-dimensional spaces $V_h \subset V$ and $\hat{V}_h \subset \hat{V}$ for the velocity space, $Q_h \subset Q$ and $\hat{Q}_h \subset \hat{Q}$ for the pressure space, $E_h \subset E$ and $\hat{E}_h \subset \hat{E}$ for the temperature space, $\mathbf{V}_h \subset \mathbf{V}$ and $\hat{\mathbf{V}}_h \subset \hat{\mathbf{V}}$ for the vector velocity space.

For this purpose, a mesh $\mathcal{K}$ of the domain Ω will be created, where K represents a set of elements such that $\Omega = \cup_{K \in \mathcal{K}} K$. The elements of $\mathcal{K}$ will be triangles for the two-dimensional case and tetrahedrons for the three-dimensional case. On each element, the functions (v, q, η) are required to belong to an appropriate polynomial space P. Then, the discrete function spaces for the test functions spaces $\hat{V}, \hat{Q}, \hat{E}$ can be defined as

$$\begin{aligned}\hat{V}_h &= \{v \in \hat{V} : v|_K \in P_2, \forall K \in \mathcal{K}\}, \\ \hat{Q}_h &= \{q \in \hat{Q} : q|_K \in P_1, \forall K \in \mathcal{K}\}, \\ \hat{E}_h &= \{\eta \in \hat{E} : \eta|_K \in P_1, \forall K \in \mathcal{K}\},\end{aligned}$$

where P_1 denotes the linear Lagrange finite element and P_2 the quadratic Lagrange finite element. This space discretization is known as standard Taylor–Hood finite elements [16]. The discrete function spaces for the trial functions spaces V, Q, E will be define as

$$\begin{aligned}V_h &= \{v \in V : v|_K \in P_2, \forall K \in \mathcal{K}\}, \\ Q_h &= \{q \in Q : q|_K \in P_1, \forall K \in \mathcal{K}\} \\ E_h &= \{\eta \in E : \eta|_K \in P_1, \forall K \in \mathcal{K}\}.\end{aligned}$$

The continuous problem (3.2)-(3.4) becomes a full-discretized problem: Find $(\mathbf{u}_h^n, p_h^n, T_h^n) \in \mathbf{V}_h \times Q_h \times E_h$,

such that

$$b(q,\mathbf{u}_h^n)=0, \tag{3.5}$$

$$\begin{aligned}\frac{1}{\Delta t}\left(T_h^n-T_h^{n-1},\eta\right)+\theta\beta\left(\mathbf{u}_h^n,T_h^n,\eta\right)+(1-\theta)\beta\left(\mathbf{u}_h^{n-1},T_h^{n-1},\eta\right)\\ +\theta e\left(T_h^n,\eta\right)+(1-\theta)e\left(T_h^{n-1},\eta\right)=\theta\lambda^n\left(\eta\right)+(1-\theta)\lambda^{n-1}\left(\eta\right),\end{aligned} \tag{3.6}$$

$$\begin{aligned}\frac{1}{\Delta t}\left(\mathbf{u}_h^n-\mathbf{u}_h^{n-1},\mathbf{v}\right)+\theta c\left(\mathbf{u}_h^n,\mathbf{v}\right)+(1-\theta)c\left(\mathbf{u}_h^{n-1},\mathbf{v}\right)+\theta a\left(\mathbf{u}_h^n,\mathbf{v}\right)+(1-\theta)a\left(\mathbf{u}_h^{n-1},\mathbf{v}\right)\\ -\theta b\left(p_h^n,\mathbf{v}\right)-(1-\theta)b\left(p_h^{n-1},\mathbf{v}\right)+\theta d\left(T_h^n,\mathbf{v}\right)+(1-\theta)d\left(T_h^{n-1},\mathbf{v}\right)\\ =\theta\gamma^n\left(\mathbf{v}\right)+(1-\theta)\gamma^{n-1}\left(\mathbf{v}\right).\end{aligned} \tag{3.7}$$

The following sets of vector and scalar basis functions will be introduced to compute the finite element approximations $(\mathbf{u}_h^n,p_h^n,T_h^n)$. Let $\{\boldsymbol{\varphi}_i\}_{i=1}^m$ be denoted as the basis for $\mathbf{V}_h$ and $\{\chi_j\}_{j=1}^s$ the basis for Q_h and E_h, where m and s are the interior nodes within the mesh. Then, the finite element method (3.5)-(3.7) is equivalent to

$$b(\chi_j,\mathbf{u}_h^n)=0, \tag{3.8}$$

$$\begin{aligned}\frac{1}{\Delta t}\left(T_h^n-T_h^{n-1},\chi_j\right)+\theta\beta\left(\mathbf{u}_h^n,T_h^n,\chi_j\right)+(1-\theta)\beta\left(\mathbf{u}_h^{n-1},T_h^{n-1},\chi_j\right)\\ +\theta e\left(T_h^n,\chi_j\right)+(1-\theta)e\left(T_h^{n-1},\chi_j\right)=\theta\lambda^n\left(\chi_j\right)+(1-\theta)\lambda^{n-1}\left(\chi_j\right),\end{aligned} \tag{3.9}$$

$$\begin{aligned}\frac{1}{\Delta t}\left(\mathbf{u}_h^n-\mathbf{u}_h^{n-1},\varphi_i\right)+\theta c\left(\mathbf{u}_h^n,\varphi_i\right)+(1-\theta)c\left(\mathbf{u}_h^{n-1},\varphi_i\right)+\theta a\left(\mathbf{u}_h^n,\varphi_i\right)+(1-\theta)a\left(\mathbf{u}_h^{n-1},\varphi_i\right)\\ -\theta b\left(p_h^n,\varphi_i\right)-(1-\theta)b\left(p_h^{n-1},\varphi_i\right)+\theta d\left(T_h^n,\varphi_i\right)+(1-\theta)d\left(T_h^{n-1},\varphi_i\right)\\ =\theta\gamma^n\left(\varphi_i\right)+(1-\theta)\gamma^{n-1}\left(\varphi_i\right),\end{aligned} \tag{3.10}$$

where $(\mathbf{u}_h^n,p_h^n,T_h^n)$ can be written as the following linear combinations

$$\mathbf{u}_h^n=\sum_{p=1}^m\xi_p^n\varphi_p,\qquad p_h^n=\sum_{q=1}^s\psi_q^n\chi_q,\qquad T_h^n=\sum_{r=1}^s\phi_r^n\chi_r, \tag{3.11}$$

where $\vec{\xi}^{\,n},\vec{\psi}^{\,n},\vec{\phi}^{\,n}$ are $(m\times 1)$, $(s\times 1)$, and $(s\times 1)$ vectors denoting the unknown degrees of freedom of $(\mathbf{u}_h^n,p_h^n,T_h^n)$ respectively. In this work, all the cases were computed neglecting the heat flux g_N and the traction σ_N at the boundary $\partial\Omega$, so that the terms $\lambda\left(\chi_j\right)$ and $\gamma\left(\varphi_i\right)$ can be deleted from (3.9) and (3.10). By inserting expressions (3.11) into system (3.8)-(3.10), it turns out

$$A\vec{\xi}^{\,n}=0, \tag{3.12}$$

$$B\vec{\phi}^{\,n}+\theta\Delta t\left[C\left(\vec{\xi}^{\,n}\right)+D\right]\vec{\phi}^{\,n}=B\vec{\phi}^{\,n-1}+(\theta-1)\Delta t\left[C\left(\vec{\xi}^{\,n-1}\right)+D\right]\vec{\phi}^{\,n-1}, \tag{3.13}$$

$$\begin{aligned}G\vec{\xi}^{\,n}+\theta\Delta t\left[H\left(\vec{\xi}^{\,n}\right)+J\right]\vec{\xi}^{\,n}+\theta\Delta t\left[-K\vec{\psi}^{\,n}+M\vec{\phi}^{\,n}\right]\\ =G\vec{\xi}^{\,n-1}+(\theta-1)\Delta t\left[H\left(\vec{\xi}^{\,n-1}\right)\vec{\xi}^{\,n-1}+J\vec{\xi}^{\,n-1}-K\vec{\psi}^{\,n-1}+M\vec{\phi}^{\,n-1}\right].\end{aligned} \tag{3.14}$$

Further, the following notation has been used

$$\begin{aligned}&A_{pj}^T=b(\chi_j,\varphi_p),\quad B_{rj}=(\chi_r,\chi_j),\quad C_{rj}\left(\vec{\xi}_p^{\,n}\right)=\beta\left(\vec{\xi}_p^{\,n}\varphi_p,\chi_r,\chi_j\right),\quad D_{rj}=e(\chi_r,\chi_j),\\ &K_{qi}=b(\chi_q,\varphi_i),\quad G_{pi}=(\varphi_p,\varphi_i),\quad H_{pi}\left(\vec{\xi}_p^{\,n}\right)=c\left(\vec{\xi}_p^{\,n}\varphi_p,\varphi_i\right),\quad J_{pi}=a(\varphi_p,\varphi_i),\\ &M_{ri}=d(\chi_r,\varphi_i),\end{aligned} \tag{3.15}$$

where A, K, M are $(m \times s)$ matrices, B, C, D are $(s \times s)$ matrices and G, H, J are $(m \times m)$ matrices. System (3.12)-(3.14) can be written in matrix form, reducing the problem to find the unknown degrees of freedom $(\vec{\xi}^{\,n}, \vec{\psi}^{\,n}, \vec{\phi}^{\,n})$ of $(\mathbf{u}_h^n, p_h^n, T_h^n)$ as follows

$$\begin{bmatrix} A^T & 0 & 0 \\ 0 & 0 & B + \theta\Delta t \left[C\left(\vec{\xi}^{\,n}\right) + D \right] \\ G + \theta\Delta t \left[H\left(\vec{\xi}^{\,n}\right) + J \right] & -\theta\Delta t K & \theta\Delta t M \end{bmatrix} \begin{bmatrix} \vec{\xi}^{\,n} \\ \vec{\psi}^{\,n} \\ \vec{\phi}^{\,n} \end{bmatrix} = \begin{bmatrix} \vec{0} \\ \vec{h_2}\left(\vec{\xi}^{\,n-1}, \vec{\phi}^{\,n-1}\right) \\ \vec{h_3}\left(\vec{\xi}^{\,n-1}, \vec{\psi}^{\,n-1}, \vec{\phi}^{\,n-1}\right) \end{bmatrix} \tag{3.16}$$

where the right-hand-side terms in (3.16) are defined as

$$\begin{aligned} &\vec{h_2}\left(\vec{\xi}^{\,n-1}, \vec{\phi}^{\,n-1}\right) = B\vec{\phi}^{\,n-1} + (\theta - 1)\Delta t \left[C\left(\vec{\xi}^{\,n-1}\right) + D \right] \vec{\phi}^{\,n-1}, \\ &\vec{h_3}\left(\vec{\xi}^{\,n-1}, \vec{\psi}^{\,n-1}, \vec{\phi}^{\,n-1}\right) = G\vec{\xi}^{\,n-1} + (\theta - 1)\Delta t \left[H\left(\vec{\xi}^{\,n-1}\right) \vec{\xi}^{\,n-1} + J\vec{\xi}^{\,n-1} - K\vec{\psi}^{\,n-1} + M\vec{\phi}^{\,n-1} \right]. \end{aligned} \tag{3.17}$$

3.3 Newton's Method

The nonlinear system of equations (3.16) will be solved in FEniCS using Newton's method to linearize the convective terms. To apply this method, the system of equations is expressed as $\mathcal{F}(\vec{w}) = 0$, being $\vec{w}^n = (\vec{\xi}^{\,n}, \vec{\psi}^n, \vec{\phi}^{\,n}) \in W_h = \mathbf{V}_h \times Q_h \times E_h$ the current unknown time step, such that $\mathcal{F} : W_h \to W_h$. To advance the solution from time t_{n-1} to t_n, the iteration will start for $\vec{w}^0 = (\vec{\xi}^{\,0}, \vec{\psi}^0, \vec{\phi}^{\,0})$, which is the known initial value at t_{n-1}. Newton's method will be applied until convergence is reached by solving the following in each iteration n for each time step Δt

$$D_w\mathcal{F}\left(\vec{w}^k\right)\Delta\vec{w}^k = -\mathcal{F}\left(\vec{w}^k\right), \tag{3.18}$$

where $\Delta\vec{w}^k = \vec{w}^{k+1} - \vec{w}^k$ and the linear operator $D_w\mathcal{F}$ represents the Jacobian of $\mathcal{F}$. Then it can be summarized the full-discretized problem of the model for laminar and incompressible flow with heat transfer as shown in algorithm (1).

Algorithm Incompressible Navier-Stokes-Boussinesq

set $\vec{w}^0 = \left(\vec{\xi}^{\,n-1}, \vec{\psi}^{n-1}, \vec{\phi}^{\,n-1}\right)$ ▷ previous known time step
while $t < t_{end}$ **do**
  for $k = 0, 1, 2...$ **do**
    solve $D_w\mathcal{F}\left(\vec{w}^k\right)\Delta\vec{w}^k = -\mathcal{F}\left(\vec{w}^k\right)$
    get $\Delta\vec{w}^k$
    set $\vec{w}^{k+1} = \vec{w}^k + \Delta\vec{w}^k$
    if $\|\Delta\vec{w}^k\| < \epsilon$ **then** ▷ predefined tolerance ϵ
      stop
    end if
  end for
  update $\vec{w}^0 = \vec{w}^{k+1}$
  update $t = n\Delta t$ ▷ move to next time step
end while

Chapter 4

Numerical validations

To validate the code, four different studies will be considered for the two-dimensional case, and the fourth study also for a three-dimensional case. Many authors have studied the flow past a circular cylinder at low Reynolds numbers, therefore the validation will focus on this type of configuration, although other geometries will be studied. The first study will be the flow past a heated circular cylinder neglecting the effects of buoyancy forces ($\mathrm{Ri} = 0$) for a range of Reynolds number from 10 to 40, and the second one considering the influence of buoyancy forces ($\mathrm{Ri} \neq 0$) for $\mathrm{Re} = 10$ and $\mathrm{Re} = 45$ at Richardson numbers $\mathrm{Ri} = 1$, $\mathrm{Ri} = 1.5$, and $\mathrm{Ri} = 2$. It can be noticed that the system of partial differential equations (2.12)-(2.14) where $\mathrm{Ri} = \mathrm{Gr}/\mathrm{Re}^2$ becomes an uncoupled system by setting the Richardson number to zero. The third study will be the flow past a heated circular cylinder for a Reynolds number of 100 and 200.

The last configuration corresponding to the two and three-dimensional case will be the study of natural convection in a square enclosure with a circular cylinder for a Reynolds number of $\mathrm{Re} = 1$ and a Rayleigh number of $\mathrm{Ra} = 10^4$. This configuration has been chosen because it is a stationary study and will only be calculated in a single time step, which greatly reduces the computation time. First, a two-dimensional model will be calculated and then compared to a slice of the center of the three-dimensional domain.

4.1 Forced convection flow past a heated circular cylinder for a range of Reynolds number from 10 to 40

A schematic representation of the flow past a heated circular cylinder is shown in Figure 4.1, where D is the diameter of the circular cylinder, U_∞ is the uniform incoming velocity, T_∞ is the inlet fluid temperature, and T_w is the uniform cylinder temperature. The center of the cylinder is located at L_ϕ from the inlet and is surrounded by a fluid of mass density ρ, dynamic viscosity μ, and thermal conductivity κ. The diameter D, uniform inlet velocity U_∞, and uniform cylinder temperature T_w will be taken as the length scale, velocity scale, and temperature scale of the problem, respectively.

The computational domain used for this study had a dimensionless size of $L_\phi = 10D$, $L = 25D$, and $H = 20D$. In this problem, the velocity, temperature, and pressure fields will be studied for a range of Reynolds number (Re) from 10 to 40 and Prandtl number $\mathrm{Pr} = 0.7$, under forced convection over a heated circular cylinder, which means that the convective effects dominate over the buoyancy effects and the Richardson number (Ri) can be taken as zero. This configuration has been studied by Takami and Keller [27], Biswas et al. [5], and Redal et al. [25].

The grid used for computations is shown in Figure 4.2. Small triangular elements were generated around the cylinder and in the wake region, whereas the size of the elements becomes thicker in the rest of the domain. The grid is made up of 30,337 elements and 15,372 nodes. The mesh size on the cylinder surface was $0.014D$ and this size of the elements gradually varied to $0.049D$ in a radius of $1.5D$. In the

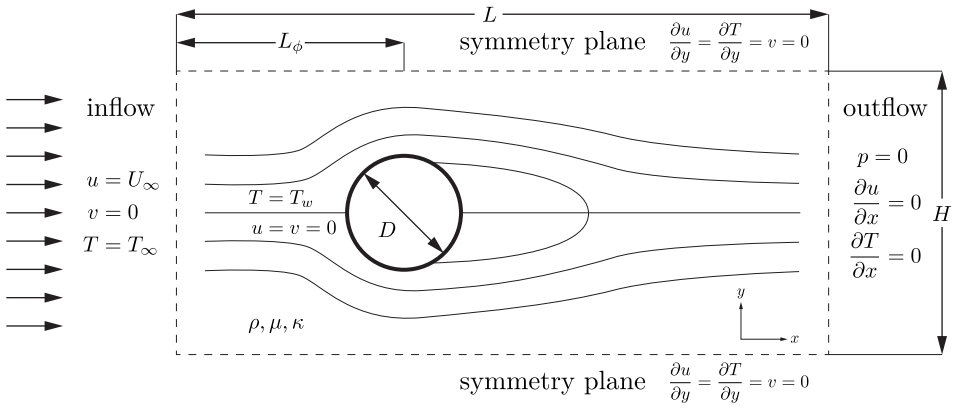

Figure 4.1: Dimensional physical domain with boundary conditions for the first three studies.

rest of the domain, the element size was less than $0.52D$. This mesh generation was based on the work of Redal et al. [25] in order to obtain the same results.

The iterative method was carried out using a tolerance of $\epsilon = 10^{-10}$ as the stopping criterion, with a maximum number of iterations of 20 and a final dimensionless time of 10 with a time step of 0.1.

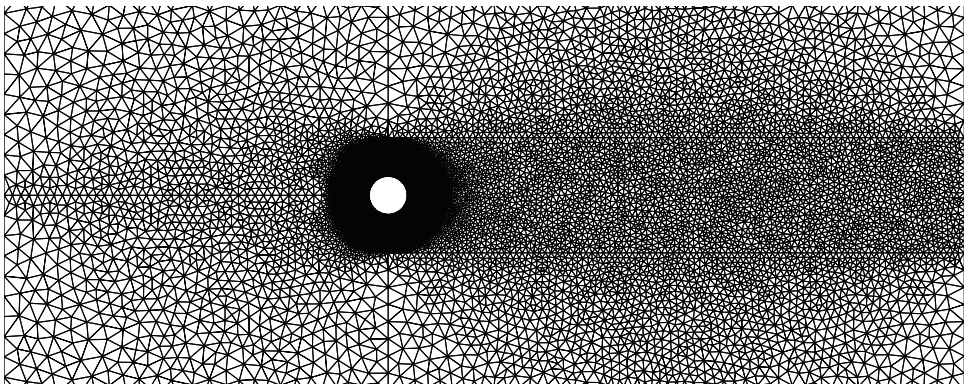

Figure 4.2: Closer view of the grid used for computation for the first three studies.

4.1.1 Test results and discussion

The simulations were carried out for a range of Reynolds number from 10 to 40. Figure 4.5 shows the streamlines for each Reynolds number and it can be seen the formation of a symmetric steady wake, which is the typical bubble geometry of the flow, represented in Figure 4.3. It can be noticed that the higher the Reynolds number the more the recirculation zone grows. The results for the pressure contours are depicted in Figure 4.6, where it is shown that the lowest pressure can be located near the upper E and lower F separation points. The highest pressure is reached at the front stagnation point A. The contours are symmetrical about the horizontal line that cuts the front stagnation point A and the rear of the cylinder B.

Figure 4.7 shows the temperature contours around the heated cylinder for each Reynolds number, where it can be seen symmetrical isotherms concerning the horizontal line that cuts the front stagnation point A and the rear of the cylinder B. The higher the Reynolds number, the steeper the temperature

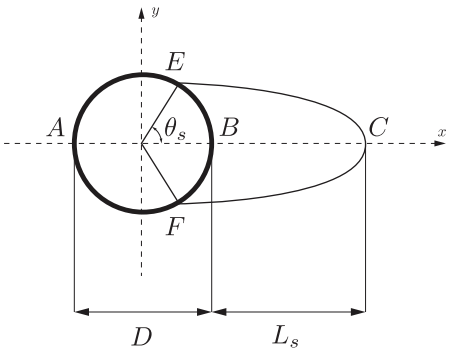

Figure 4.3: Schematic of the wake-bubble geometry.

contours in the wake region, which means that heat transfer enhances due to high velocity.

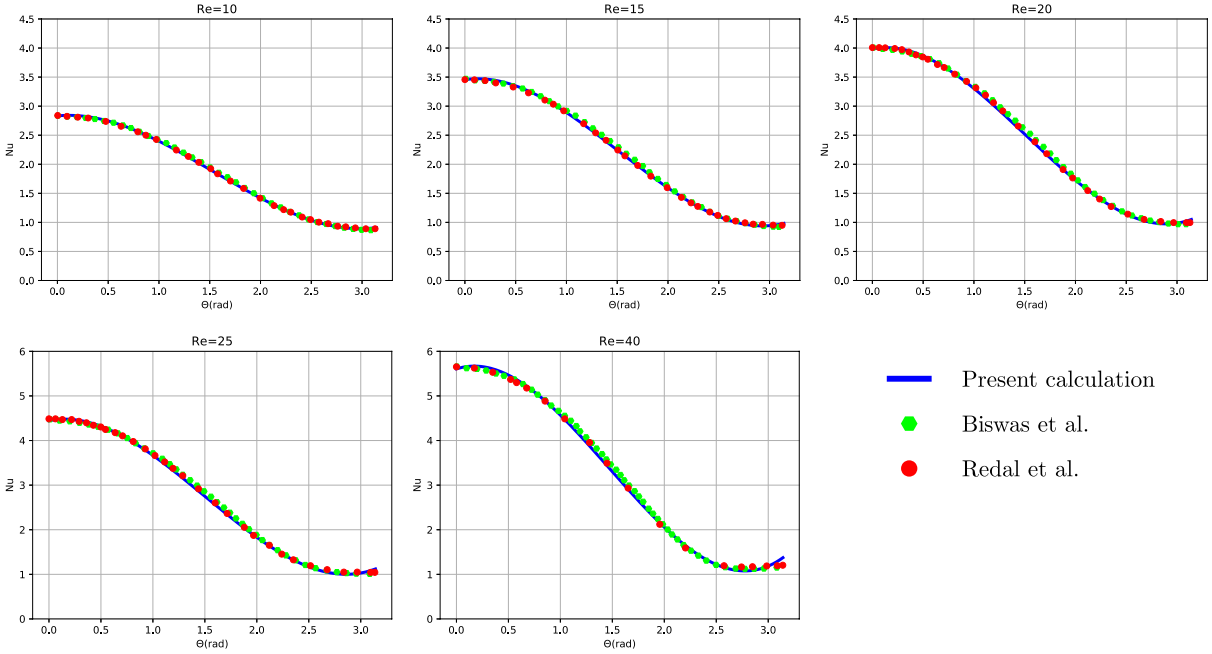

Figure 4.4: Variation of local Nusselt number on the cylinder surface for Re = 10, Re = 15, Re = 20, Re = 25, and Re = 40.

The eddy length L_s and the separation angle θ_s were calculated to compare our solutions. The eddy length is measured from the rear of the cylinder B to the wake stagnation point C and the separation angle from the rear stagnation point B to the upper E or lower F separation points.

Table 4.1 shows the results obtained in the present work and compared to the values obtained by Takami and Keller [27], Biswas et al. [5], and Redal et al. [25]. The eddy length is reported dimensionless, taken the cylinder radius $R = 2D$ as the length scale to match previous references. The results show a very good agreement with the values obtained by other authors, with an absolute error that does not exceed 3%. The local Nusselt number was calculated, which indicates the local heat lost by heat

Table 4.1: Comparison of the eddy length (L_s) and the separation angle θ_s

Variable	**Re**	**Present calculation**	[25]	[5]	[27]
$2L_s/D$	10	0.536	0.512	0.521	0.500
	15	1.236	1.227	1.189	1.162
	20	1.906	1.866	1.865	1.844
	25	2.560	2.548	2.517	-
	40	4.576	4.480	4.424	4.650
$\theta_s\,(^\circ)$	10	29.40	28.57	29.12	29.30
	15	38.60	38.57	38.57	38.60
	20	43.67	43.58	43.64	43.65
	25	46.80	47.14	46.89	-
	40	52.27	51.43	53.10	53.55

conduction and is defined as

$$\mathrm{Nu} = -\frac{\partial T}{\partial \mathrm{n}},$$

where n denotes the normal direction to the cylinder surface. The local Nusselt number distribution was calculated for a range of Reynolds numbers from 10 to 40 shown in Figure 4.4 and was compared with the results obtained by Biswas et al. [5], and Redal et al. [25], showing a good agreement.

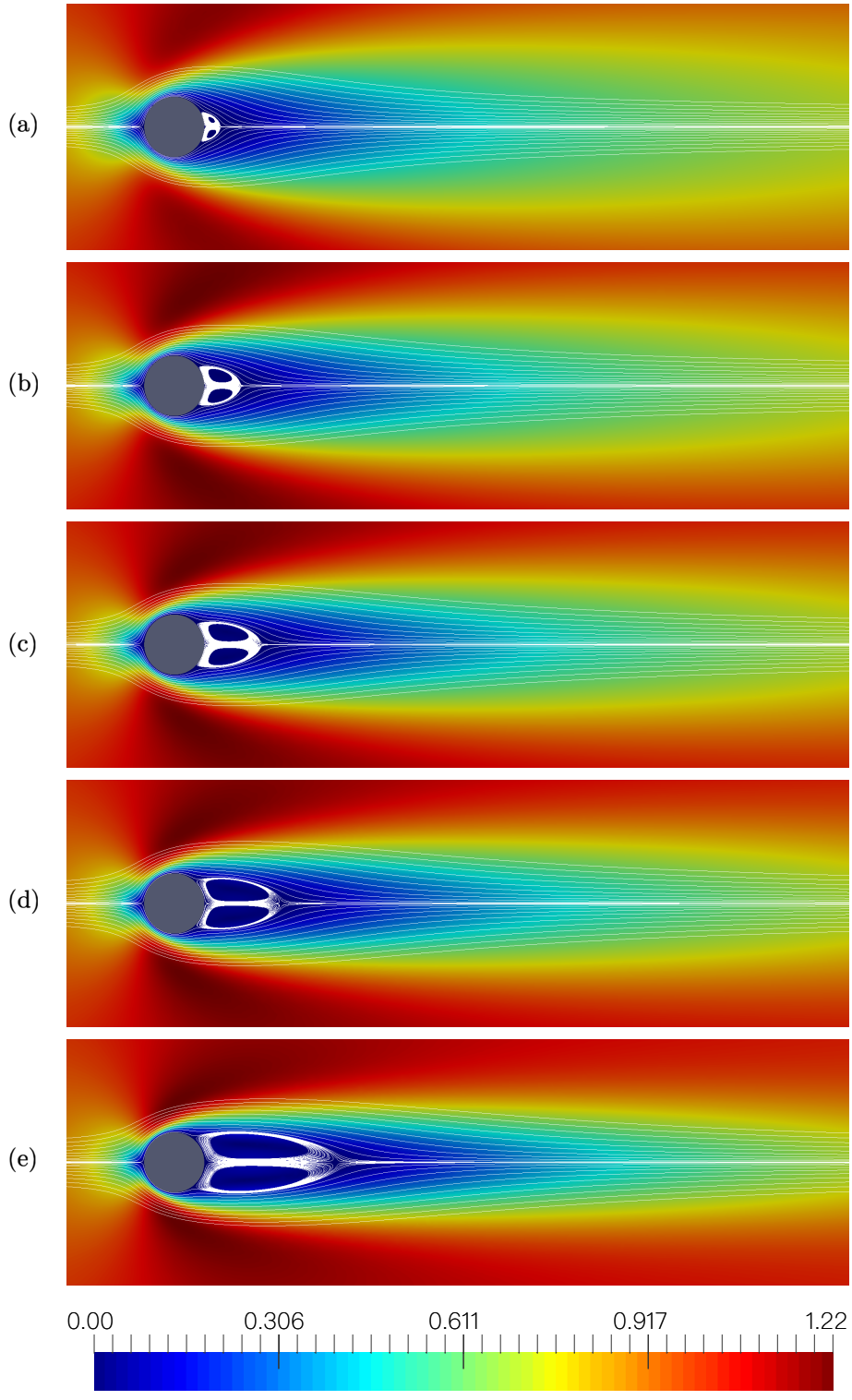

Figure 4.5: Streamlines for (a) Re = 10, (b) Re = 15, (c) Re = 20, (d) Re = 25, and (e) Re = 40.

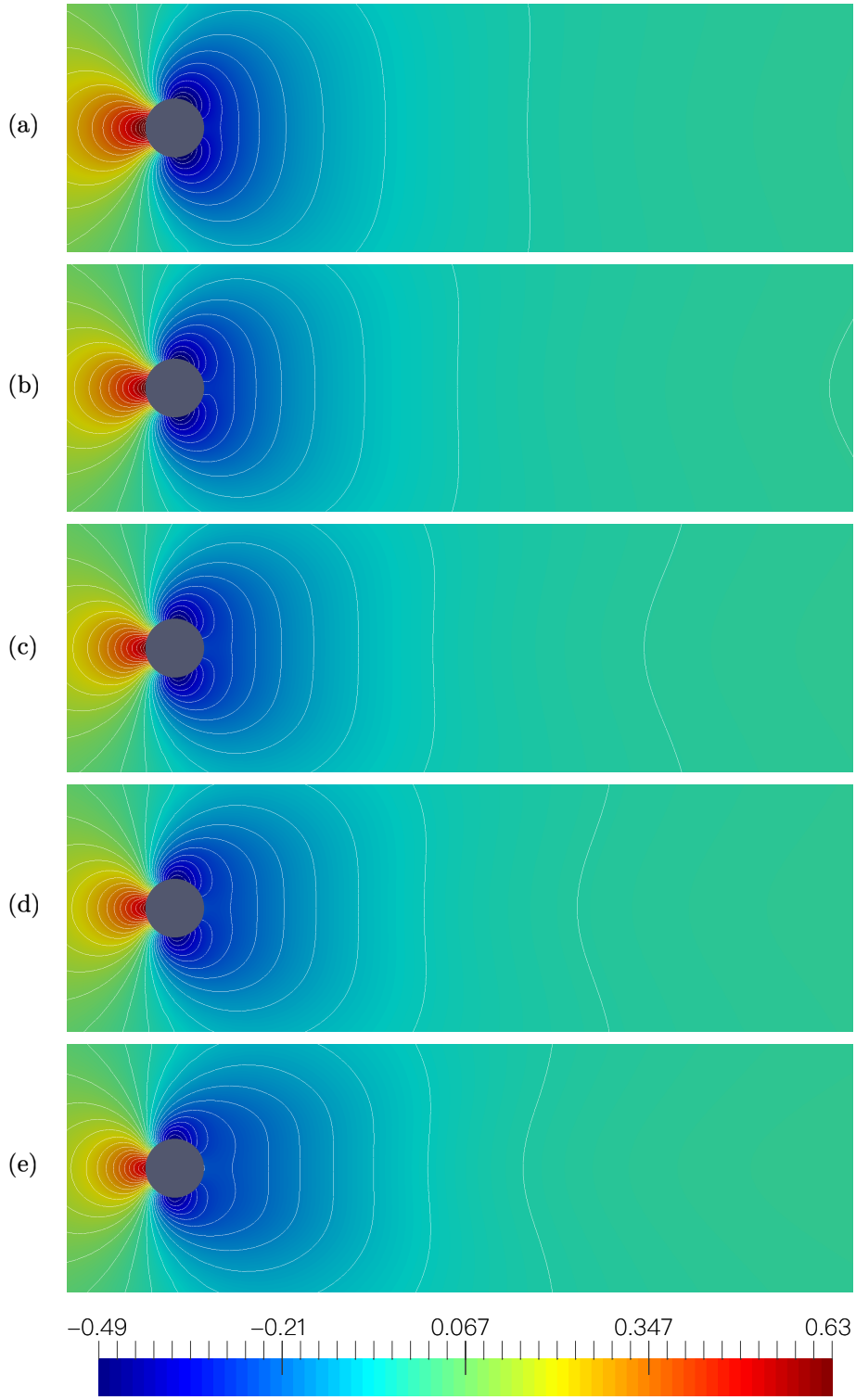

Figure 4.6: Pressure contours for (a) Re = 10, (b) Re = 15, (c) Re = 20, (d) Re = 25, and (e) Re = 40.

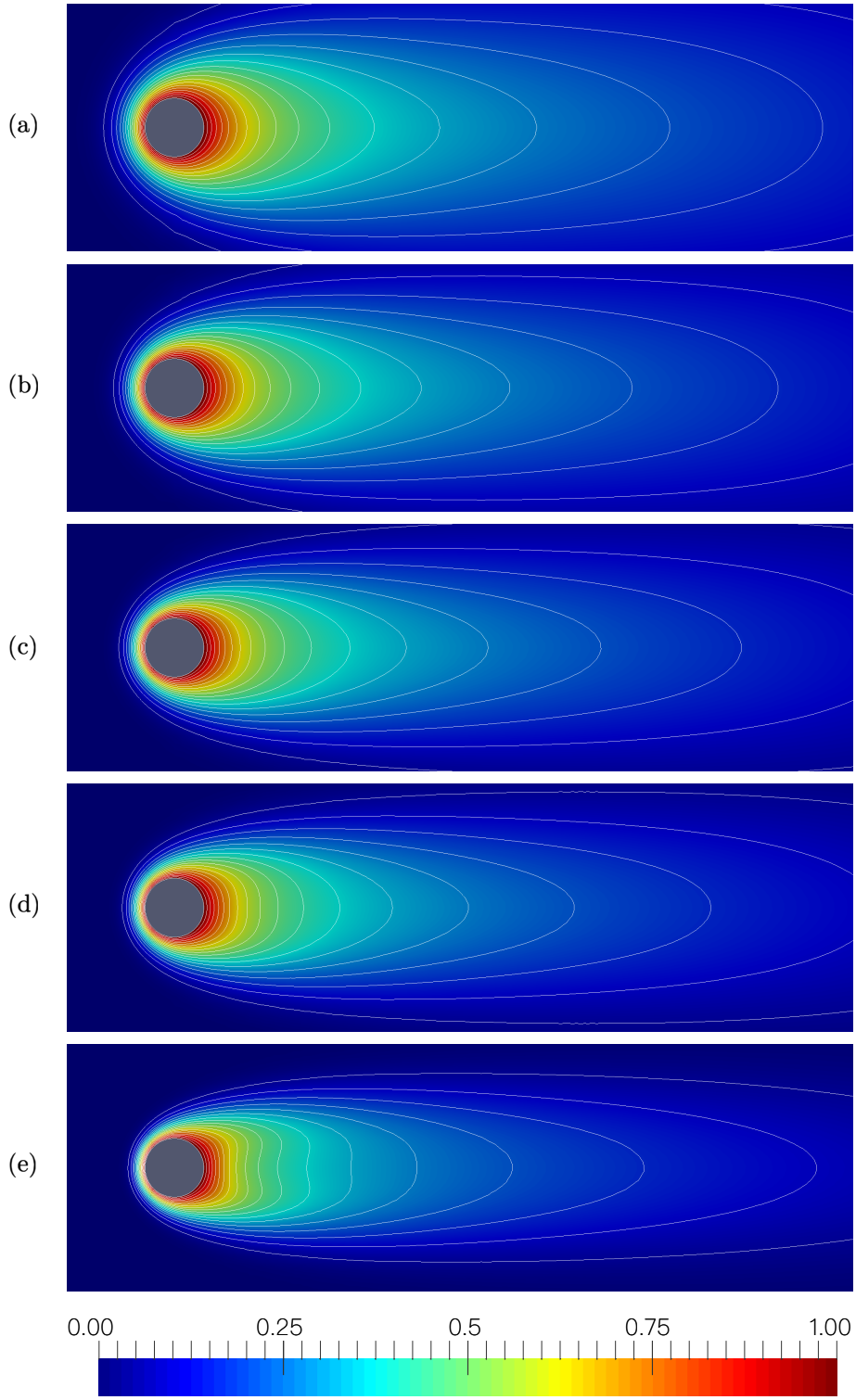

Figure 4.7: Temperature contours for (a) Re = 10, (b) Re = 15, (c) Re = 20, (d) Re = 25, and (e) Re = 40.

4.2 Mixed convection flow past a heated circular cylinder

Representation of the flow past a heated circular cylinder considering buoyancy forces can be also shown in Figure 4.1. The parameters L_ϕ, L, H, as well as the properties of the fluid will be the same as those used in the first study.

The computational domain used for this study had a dimensionless size of $L_\phi = 10D$, $L = 25D$, and $H = 20D$. In this problem, the velocity, temperature, and pressure fields will be studied for Reynolds numbers (Re) of 10 and 45 and Prandtl number Pr = 0.7, under mixed convection over a heated circular cylinder, which means that the forced and natural convection are combined and then the Richardson number ($\mathrm{Ri} = \mathrm{Gr}\,\mathrm{Re}^{-2}$) cannot be taken as zero, because buoyancy effects are becoming important along with convective effects. This configuration has also been studied by Biswas et al. [5].

The grid used for computations is shown in Figure 4.2, which is made up of 30,337 elements and 15,372 nodes. The mesh size on the cylinder surface was $0.014D$ and this size of the elements gradually varied to $0.049D$ in a radius of $1.5D$. In the rest of the domain, the element size was less than $0.52D$.

The iterative method was carried out using a tolerance of $\epsilon = 10^{-10}$ as the stopping criterion, with a maximum number of iterations of 20 and a final dimensionless time of 40 with a time step of 0.1.

4.2.1 Test results and discussion

The calculations were carried out for a Reynolds number of Re = 10 and Re = 45, considering the influence of buoyancy forces indicated by a Richardson number of Ri = 1, Ri = 1.5 and Ri = 2. Figure 4.9 shows the streamlines for Re = 10. It can be noticed that the symmetry on the horizontal line has been lost and increasing the Richardson number from Ri = 0 to Ri = 1 results a decrease in the recirculation bubble showed in Figure 4.5, where buoyancy forces were neglected. Figure 4.9 also shows the behavior for Ri = 1.5 and Ri = 2. At these Richardson numbers, buoyancy dominates inertial forces. A steady wake was observed for Ri = 1, while the wake becomes unsteady for Ri = 1.5 and Ri = 2, which is consistent with previous studies of Biswas et al. [5] indicating that a steady wake is found below Ri = 1.4. Also a recirculation zone is perceived at Ri = 2 near the upper wall of the physical domain. This happens because in this case, the buoyant force dominates stronger than the convective one and produces this recirculation behavior. These results show excellent agreement with the ones obtained by Biswas et al. [5].

The pressure contours are shown in Figure 4.10 for Re = 10. Now it can be seen that the highest pressure is not located at the front stagnation point A and the lowest pressure is located below the cylinder toward the lower wall of the physical domain. A steady behavior can be observed for Ri = 1, but for Ri = 1.5 and Ri = 2, high and low-pressure zones begin to appear towards the upper wall, which can be easily seen for Ri = 2 and it is related with the recirculation zone.

Figure 4.11 shows the temperature contours around the heated cylinder for Re = 10. If these results are compared to that of Re = 10 in forced convection flow past a heated circular cylinder shown in Figure 4.7; it can be noticed a completely different wake behavior. Now the presence of the buoyancy force produces oscillations in the flow which leads to periodic variation of the heat flux on the solid surface of the circular cylinder. The higher the Richardson number, the more oscillatory instabilities grow.

Figure 4.12 shows the streamlines for Re = 45 at Ri = 1 and Ri = 2. A steady wake was observed for Ri = 1, while the wake becomes unsteady for Ri = 2, which is consistent with previous studies of Biswas et al. [5] indicating that a steady wake is found below Ri = 1.985 for Re = 45. No recirculation zone is perceived for Ri = 1 and Ri = 2. In this case, the Reynolds number is higher than 10, so a recirculation zone cannot be seen in the physical domain due to increased velocity.

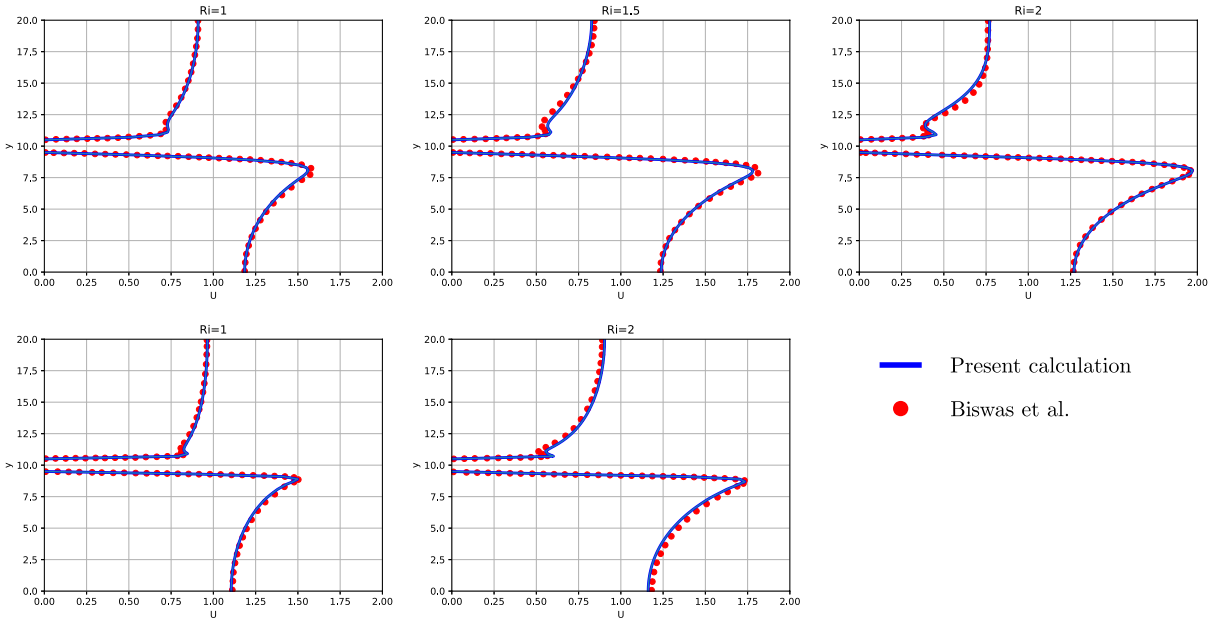

Figure 4.8: Velocity profiles at $x = 10$ for different Ri at (a) Re = 10, and (b) Re = 45.

Figure 4.13 shows the pressure contours for Re = 45 at Ri = 1 and Ri = 2. These results are similar to those shown for Re = 10 but now high and low-pressure zones will not appear due to increased velocity. The temperature contours are shown in Figure 4.14 for Re = 45 at Ri = 1 and Ri = 2. The presence of the buoyancy force produces oscillations and heat transfer will occur faster due to increased velocity.

The horizontal velocity component profile was calculated for Re = 10 and Re = 45 at $x/D = 10$ to compare the results of the present work with those obtained by Biswas et al. [5] showing an excellent agreement as can be seen in Figure 4.8.

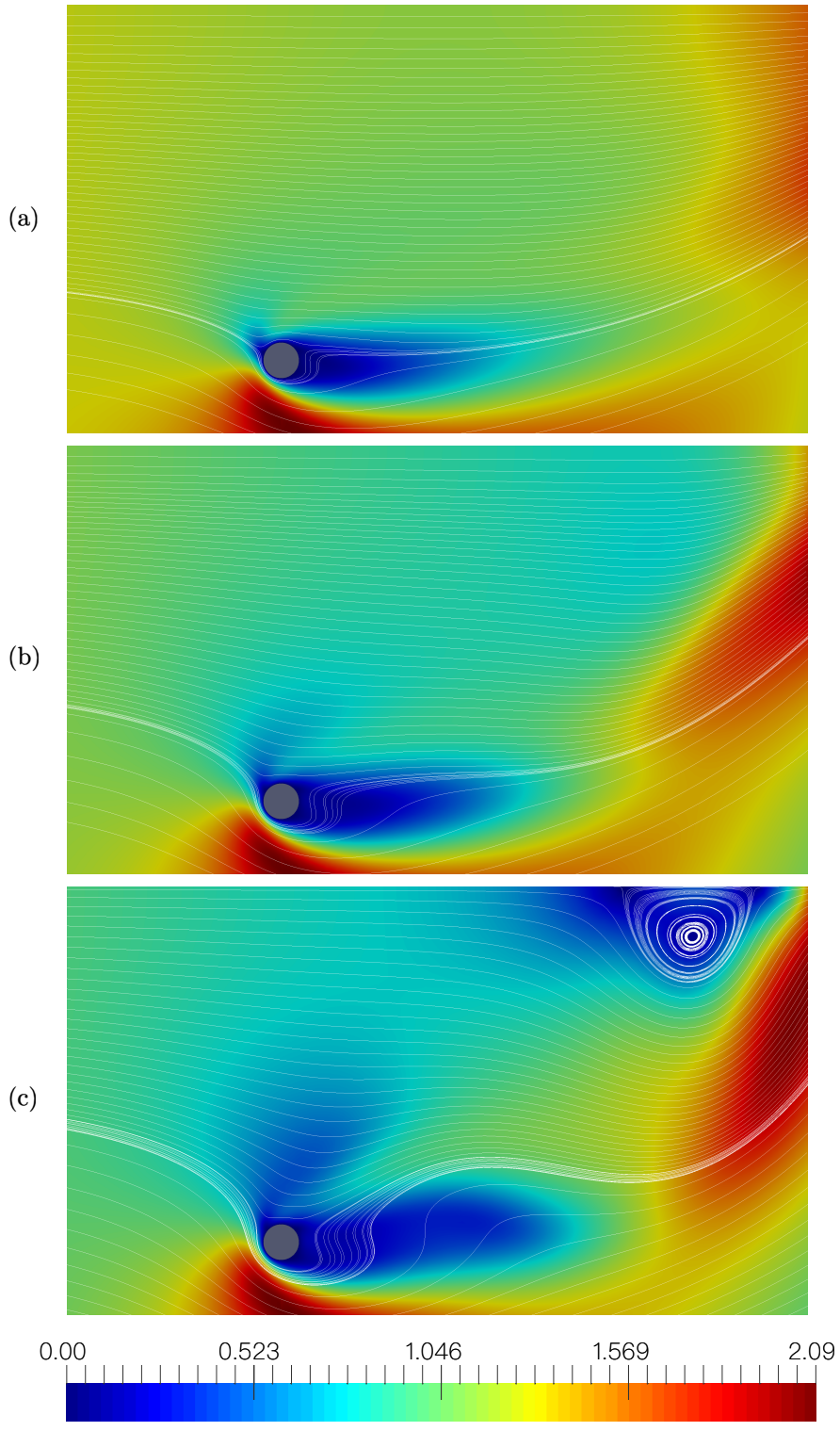

Figure 4.9: Streamlines for Re = 10 at (a) Ri = 1, (b) Ri = 1.5, and (c) Ri = 2.

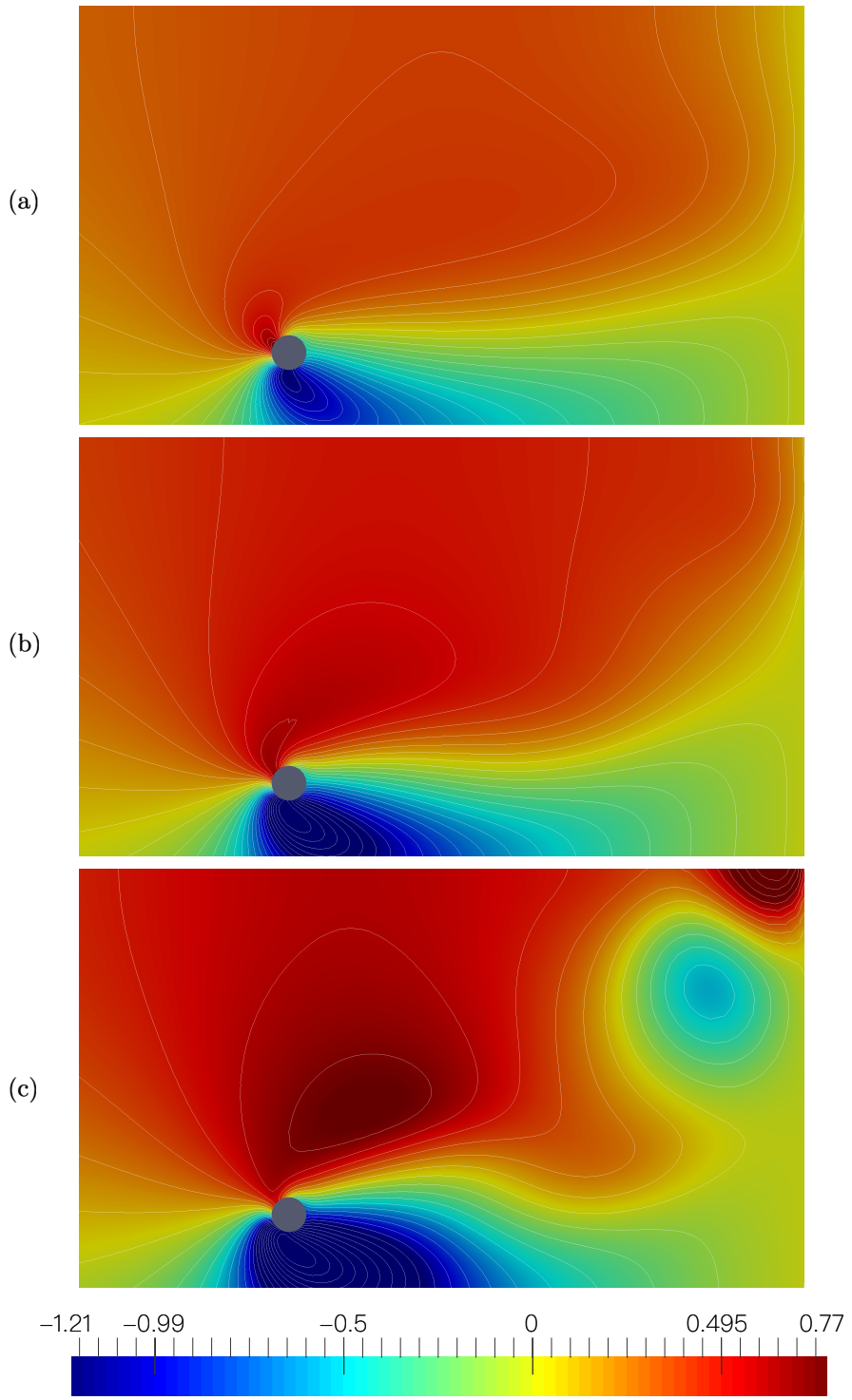

Figure 4.10: Pressure contours for Re = 10 at (a) Ri = 1, (b) Ri = 1.5, and (c) Ri = 2.

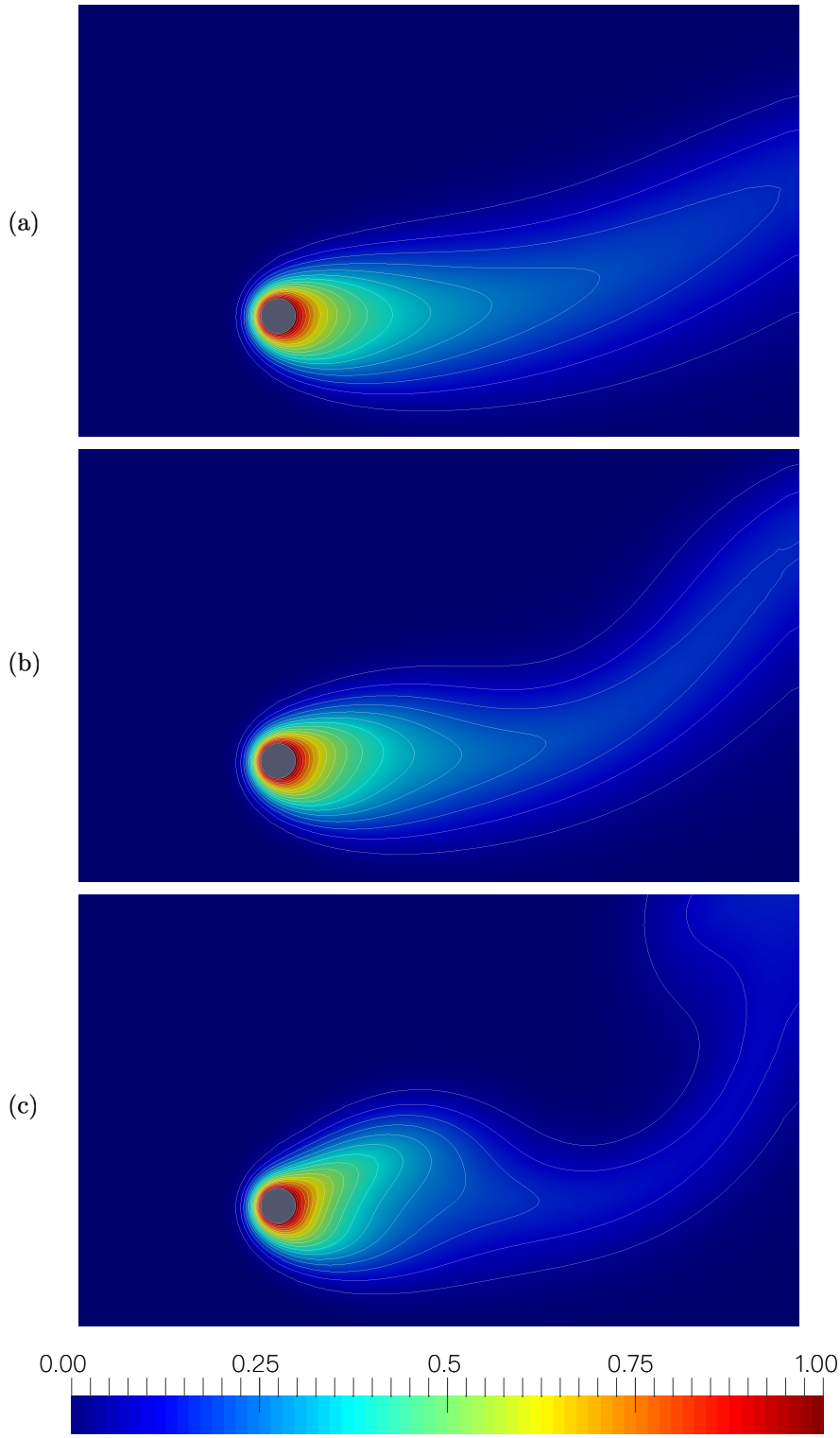

Figure 4.11: Temperature contours for Re = 10 at (a) Ri = 1, (b) Ri = 1.5, and (c) Ri = 2.

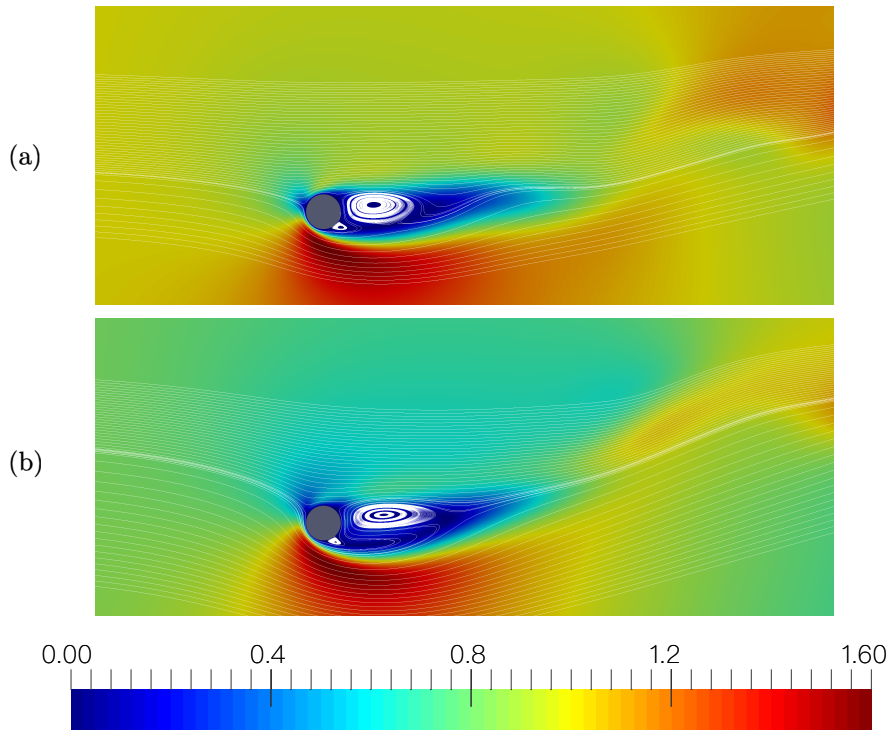

Figure 4.12: Streamlines for Re = 45 at (a) Ri = 1, and (b) Ri = 2.

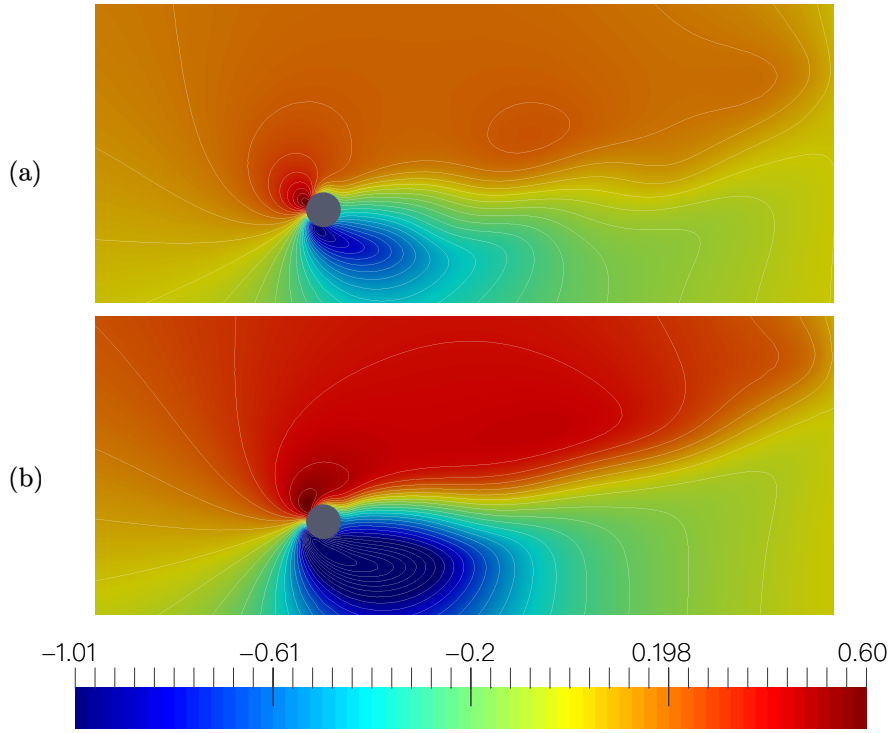

Figure 4.13: Pressure contours for Re = 45 at (a) Ri = 1, and (b) Ri = 2.

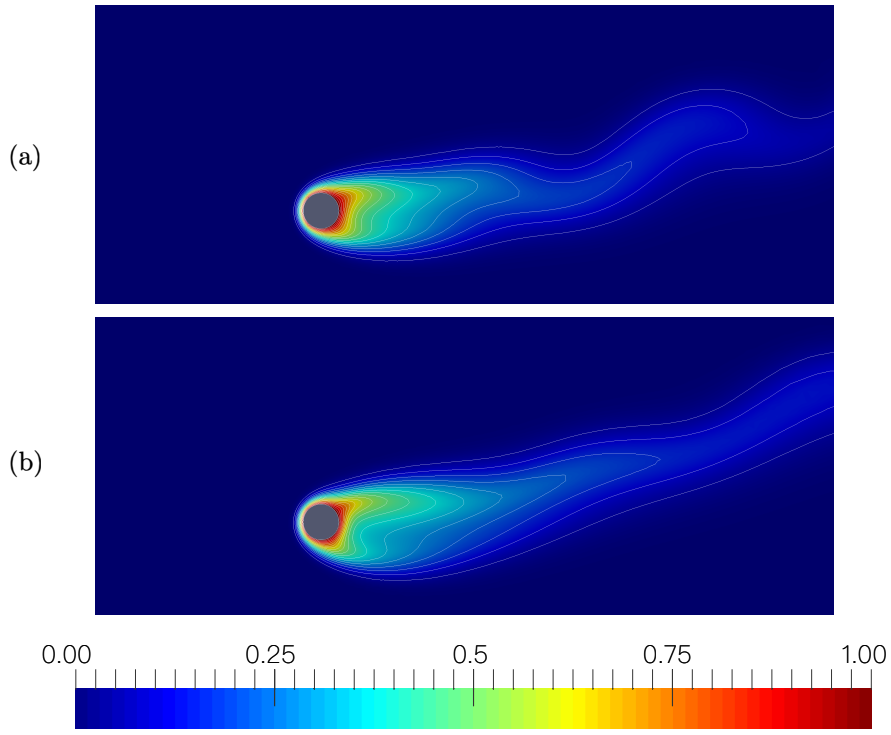

Figure 4.14: Temperature contours for Re = 45 at (a) Ri = 1, and (b) Ri = 2.

4.3 Forced convection flow past a heated circular cylinder for a Reynolds number of 100 and 200

A scheme of the flow past a non-heated circular cylinder can be shown in Figure 4.1. Now, the parameters L_ϕ, L, H will change for this case and no temperature will be set on the cylinder wall and at the inlet.

The computational domain used had a dimensionless size of $L_\phi = 8D$, $L = 38D$, and $H = 32D$. The velocity, temperature, and pressure fields will be studied for a Reynolds number (Re) of 100 and 200 and Prandtl number Pr = 0.7, under forced convection over a non-heated circular cylinder, so the Richardson number (Ri) can be taken as zero. This configuration has been studied by Rajani et al. [24], Qu et al. [21], and Redal et al. [25].

The grid used for calculations was similar to the one shown in Figure 4.2. The grid is made up of 22,725 elements and 11,511 nodes. The mesh size on the cylinder surface was $0.013D$ and this size of the elements gradually varied to $0.047D$ in a radius of $1.5D$. In the rest of the domain, the elements decreased until reaching the size of $1.81D$ at the top and bottom walls.

The iterative method was carried out using a tolerance of $\epsilon = 10^{-10}$ as the stopping criterion, with a maximum number of iterations of 20 and a final dimensionless time of 400 with a time step of 0.1.

4.3.1 Test results and discussion

The simulations were carried out for a Reynolds number of Re = 100 and Re = 200. The validation focused on the study of the vertical velocity component v at a point in the middle of the outflow plane as shown in Figure 4.15. It can be noted that after an initial transient, the vertical velocity component becomes periodic with a given period $1/f$, being f the oscillation frequency.

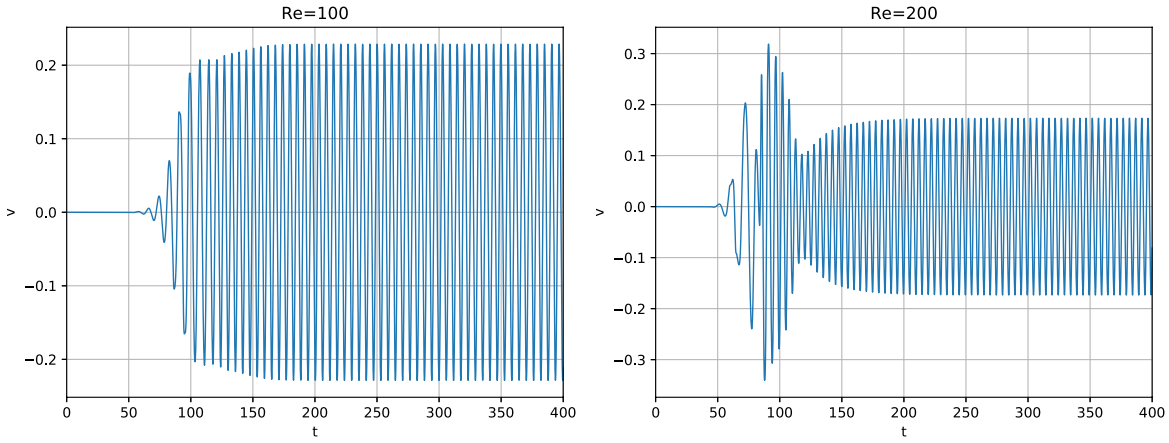

Figure 4.15: Vertical velocity in the mid of outflow plane for Re = 100 and Re = 200.

Initially, symmetrical vortices will appear just behind the circular cylinder and these recirculations will gradually grow in a similar way to those shown for a Reynolds number range of 10 to 40 in Figure 4.5. There will come a point where the vortices will no longer elongate and then an unsymmetrical behavior will start to be seen until the Von Karmann vortex street begins to appear resulting in a periodic flow.

The time-dependent behavior of the vertical velocity component v can be seen for Re = 100 and Re = 200 in Figure 4.16 and Figure 4.19 respectively, where the periodicity of flow has been successfully accomplished. To validate the results of the present work, the oscillation frequency f will be measured to determine if the oscillating flow in the wake region behaves like those of the previous works reported by Rajani et al. [24], Qu et al. [21], and Redal et al. [25]. For this purpose, the Strouhal number $S_t = fD/U_\infty$ will be calculated with D being the diameter and U_∞ the uniform inlet velocity. Since they are dimensioned as unity, S_t is equivalent to the oscillation frequency f. Table 4.2 shows the Strouhal numbers calculated in the present work for Re = 100 and Re = 200, which show a very good agreement with the values obtained by other authors.

Table 4.2: Comparison of the Strouhal number for Re = 100 and Re = 200

Re	**Present calculation**	[25]	[21]	[24]
100	0.1694	0.165	0.1649	0.1569
200	0.201	0.1954	0.1958	0.1957

From the results of Table 4.2, it can be seen that the oscillation period obtained numerically is $1/f \approx 4.97$ for Re = 200 and $1/f \approx 5.90$ for Re = 100, which is consistent with previous experimental studies by Brooks et al. [6] where it is stated that the period of oscillation observed was $1/f = 6$ for Re = 100. The time-dependent behavior of the pressure is shown for Re = 100 and Re = 200 in Figure

4.17 and Figure 4.20 respectively, where the periodicity of flow has been successfully accomplished. Similar to the description of the velocity field, initially a steady symmetrical wake will be observed behind the circular cylinder and stagnation areas such as those shown for a Reynolds number range of 10 to 40 in Figure 4.6 will be identified upstream and downstream of the cylinder. The contours will gradually become unstable and the symmetry will start to break along the horizontal axis indicating the onset of flow instability. Then an oscillatory wake behind the circular cylinder will be perceived with the presence of periodic rotating vortices.

The time-dependent behavior of the temperature is shown for Re = 100 and Re = 200 in Figure 4.18 and Figure 4.21 respectively. The description of the process follows the same steps of the velocity and pressure fields, where finally, it will be observed the total detachment of vortices in the wake.

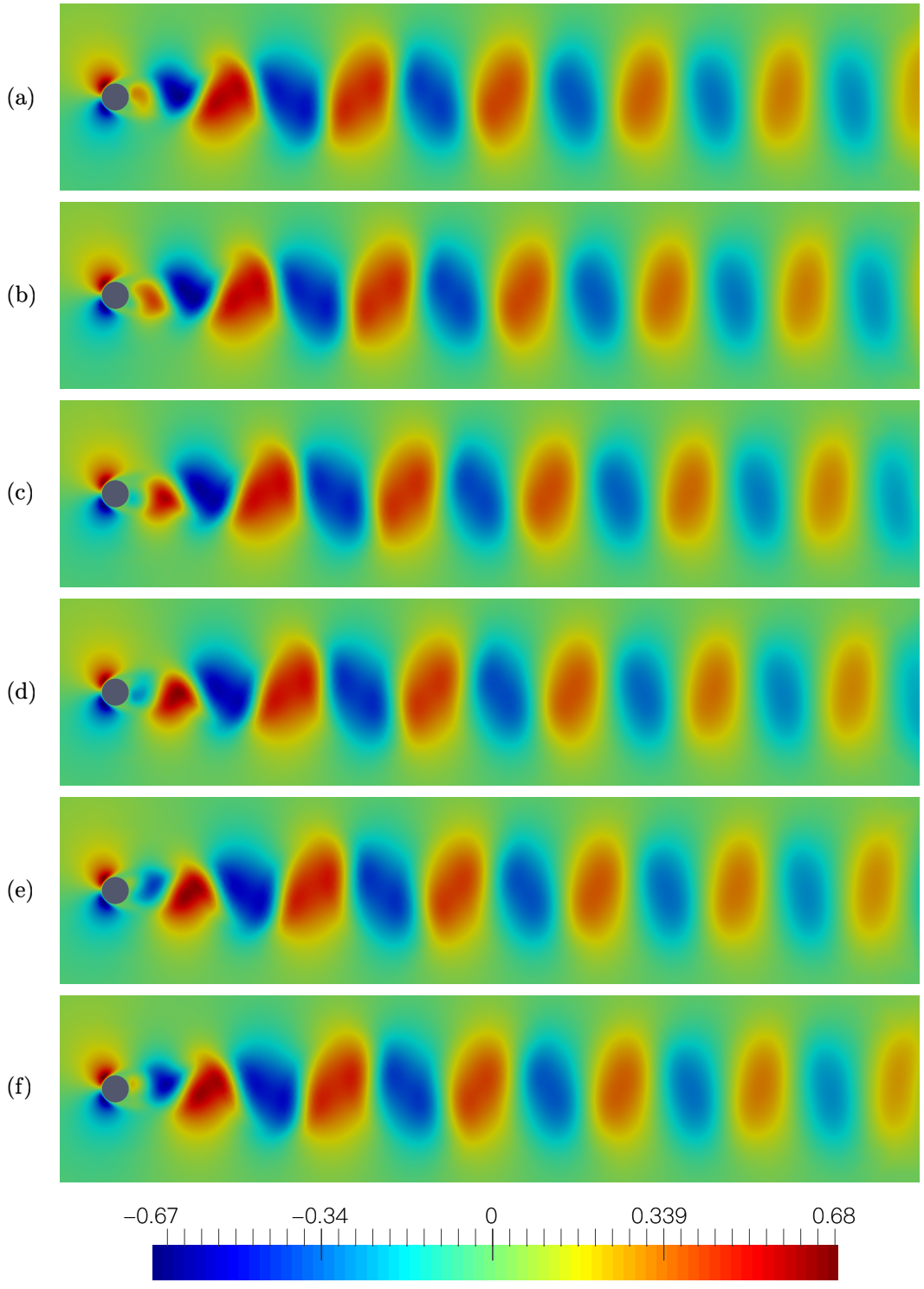

Figure 4.16: Vertical velocity component for Re = 100 at the successive instants (a) 0, (b) $\tau/6$, (c) $\tau/3$, (d) $\tau/2$, (e) $2\tau/3$, and (f) $5\tau/6$.

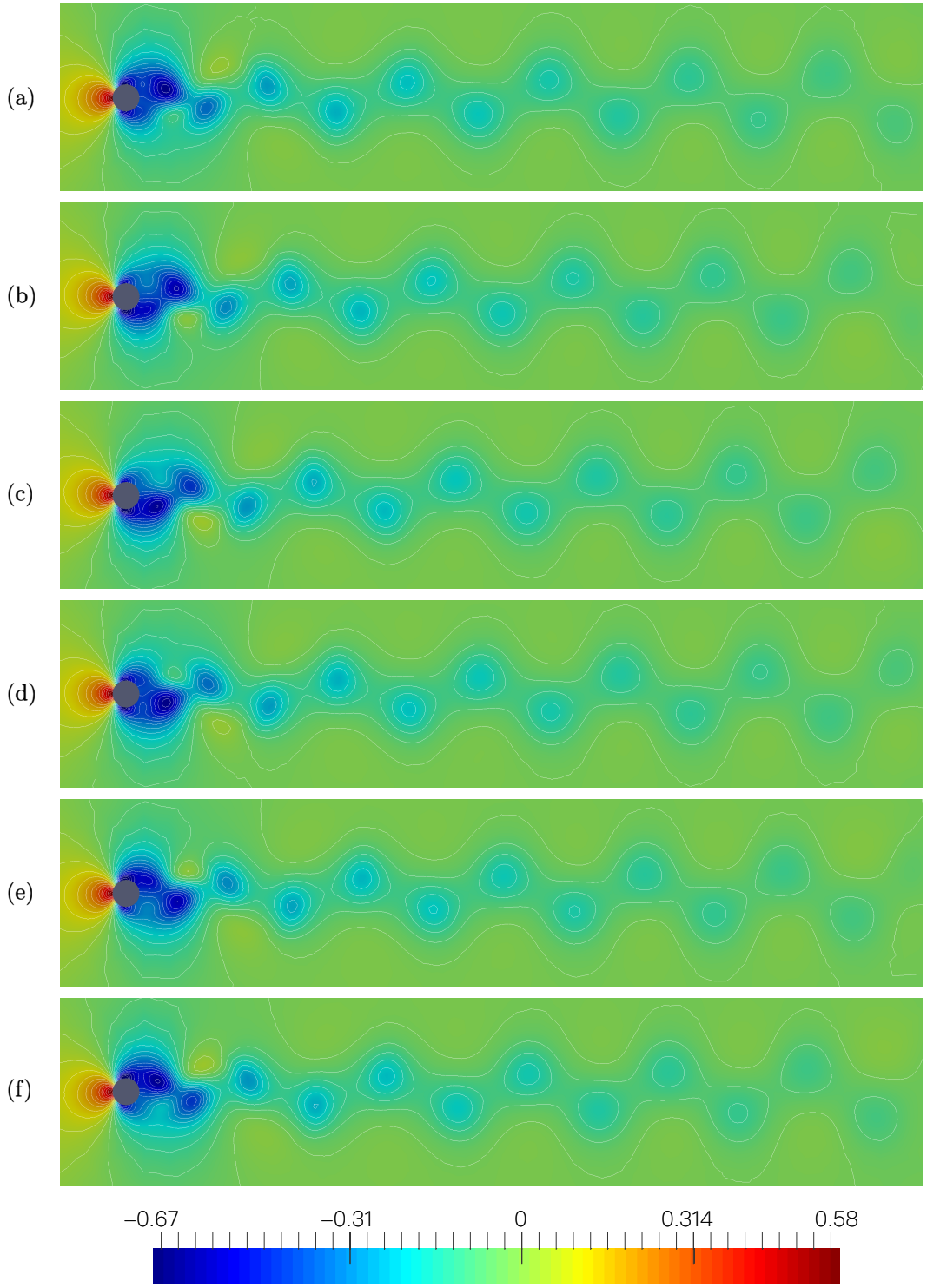

Figure 4.17: Pressure contours for Re = 100 at the successive instants (a) 0, (b) $\tau/6$, (c) $\tau/3$, (d) $\tau/2$, (e) $2\tau/3$, and (f) $5\tau/6$.

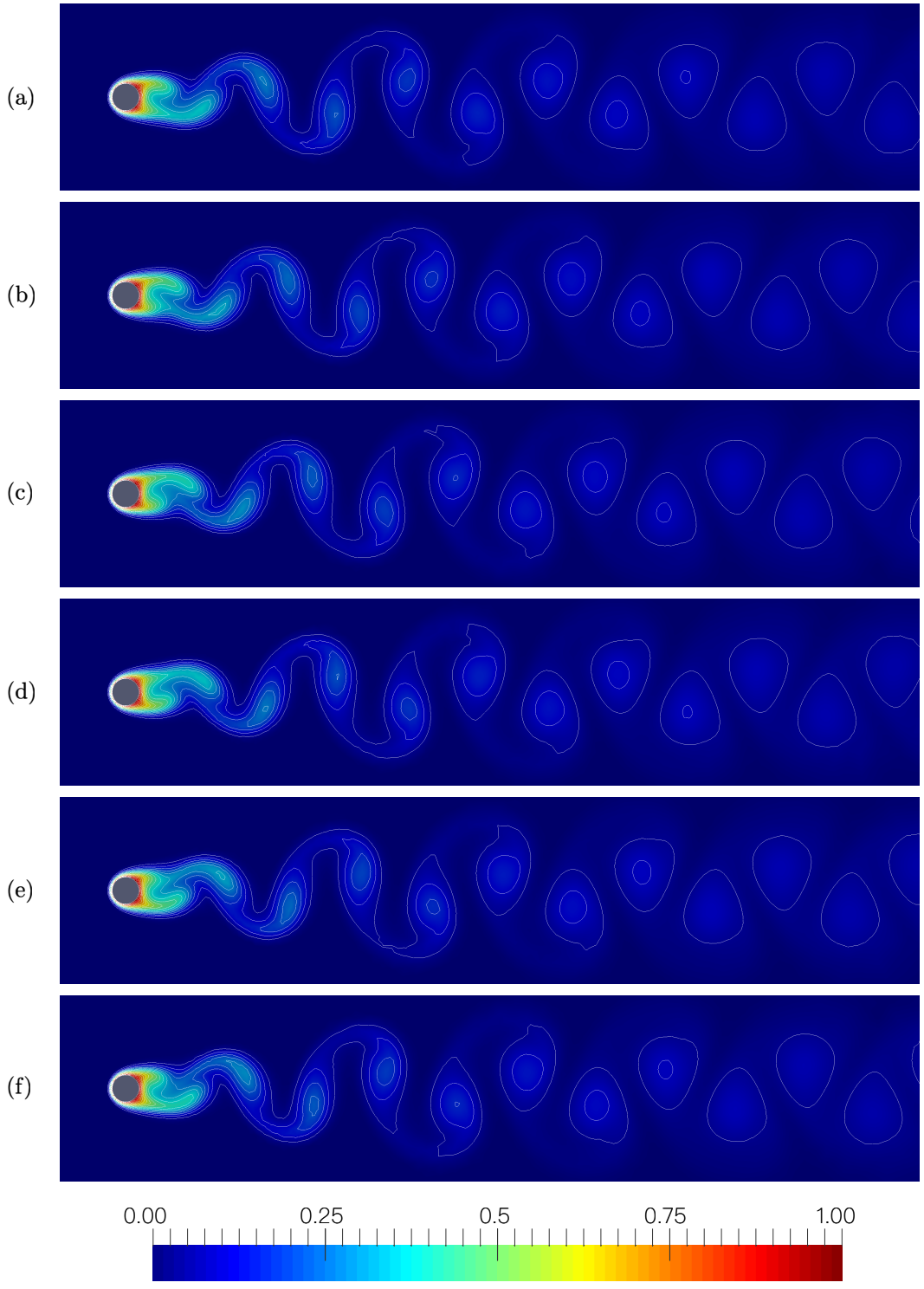

Figure 4.18: Temperature contours for $\mathrm{Re} = 100$ at the successive instants (a) 0, (b) $\tau/6$, (c) $\tau/3$, (d) $\tau/2$, (e) $2\tau/3$, and (f) $5\tau/6$.

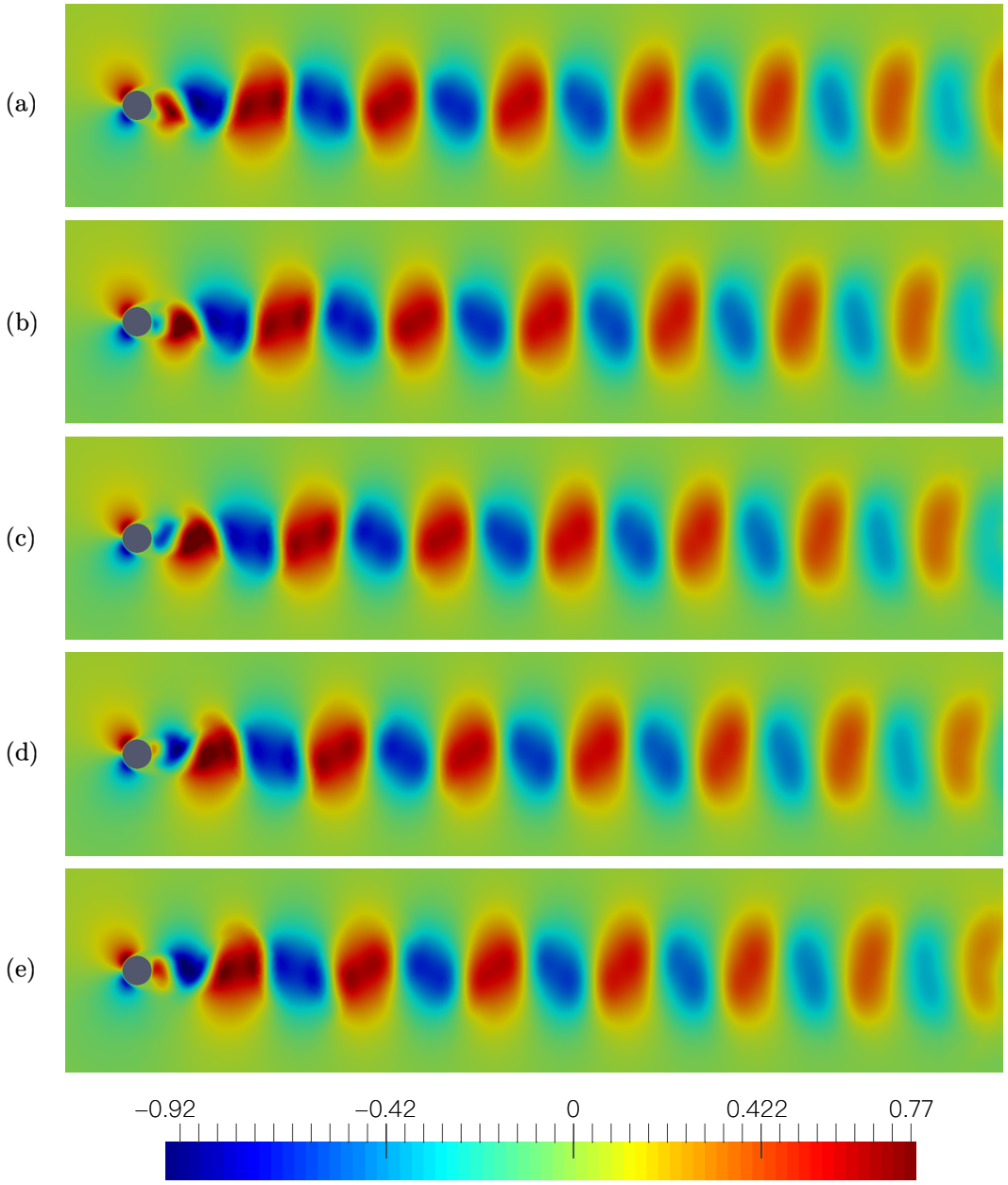

Figure 4.19: Vertical velocity component for Re = 200 at the successive instants (a) 0, (b) $\tau/5$, (c) $2\tau/5$, (d) $3\tau/5$, and (e) $4\tau/5$.

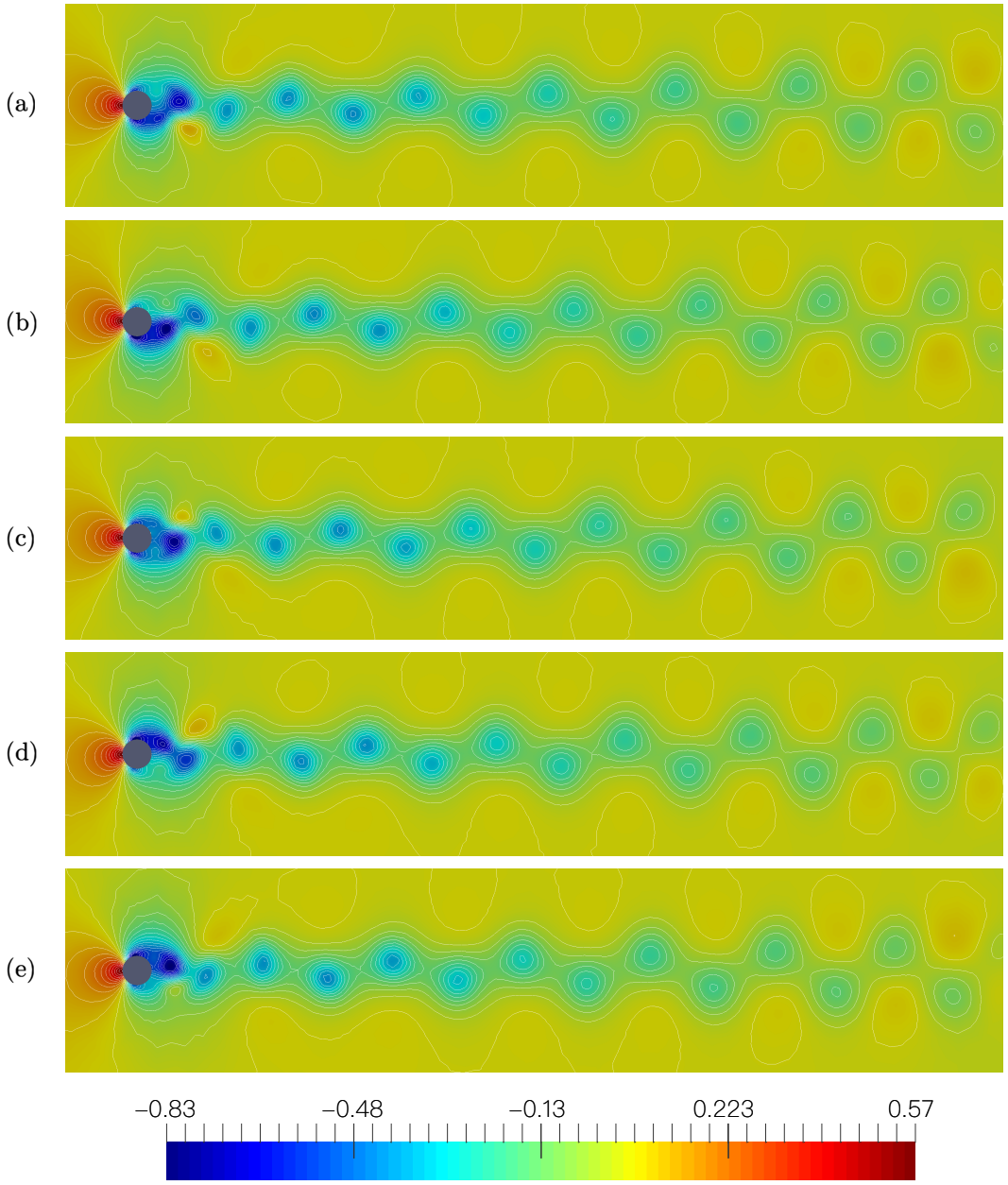

Figure 4.20: Pressure contours for Re = 200 at the successive instants (a) 0, (b) $\tau/5$, (c) $2\tau/5$, (d) $3\tau/5$, and (e) $4\tau/5$.

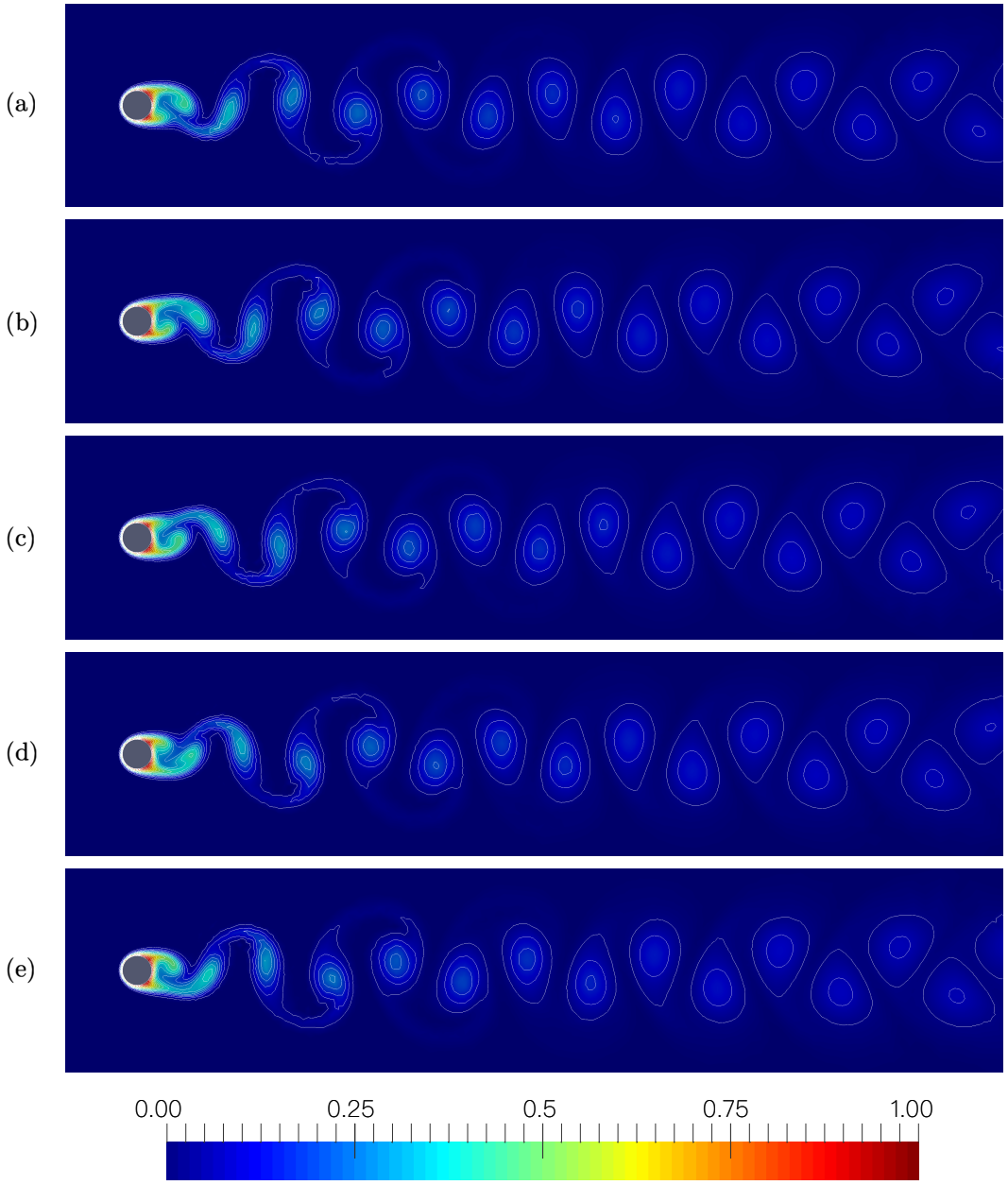

Figure 4.21: Temperature contours for Re = 200 at the successive instants (a) 0, (b) $\tau/5$, (c) $2\tau/5$, (d) $3\tau/5$, and (e) $4\tau/5$.

4.4 Natural convection in a square enclosure with a circular cylinder

A schematic representation of the flow around a heated circular cylinder in a square enclosure is shown in Figure 4.22 and a two-dimensional representation of a slice of the center of the three-dimensional domain can be shown in Figure 4.23. In the two-dimensional Figure, D denotes the diameter of the circular cylinder, T_c is the temperature of the walls and T_h is the cylinder temperature, where $T_h > T_c$. The square enclosure has sides of length $L = 1$ and the circular cylinder is just in the middle of the encloser and has a diameter of $0.4L$. The cylinder is surrounded by a fluid of mass density ρ, dynamic viscosity μ, and thermal conductivity κ.

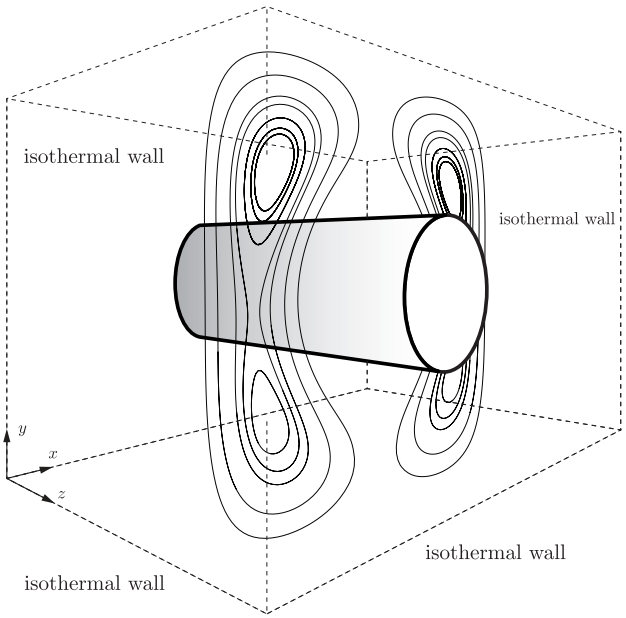

Figure 4.22: Physical domain for the three-dimensional case.

In this problem, the velocity, temperature, and pressure fields will be studied for a Reynolds number of $\mathrm{Re} = 1$, a Prandtl number of $\mathrm{Pr} = 0.7$, and a Rayleigh number of $\mathrm{Ra} = 10^4$, under natural convection over a heated circular cylinder, which means that the buoyancy effects dominate over the convective effects and the Richardson number ($\mathrm{Ri} = \mathrm{Gr}\,\mathrm{Re}^{-2}$) will not be zero because $\mathrm{Gr} \gg \mathrm{Re}^{-2}$. This configuration has been studied by Asan [3], Kim et al. [15], and Hussain et al. [14].

The grid used for the two-dimensional case is shown in Figure 4.24. Small triangular elements were generated around the cylinder and in the region of the walls, whereas the size of the elements becomes thicker in the rest of the domain. The grid is made up of 24,978 elements and 12,785 nodes. To correctly solve the viscous effects, the maximum thickness of the boundary layer was 0.05. On the cylinder and wall surfaces, the mesh size was 0.001 and gradually varied to 0.005 until it reached the thickness of the boundary layer. In the rest of the domain, the elements become a little bigger.

The iterative method was carried out using a tolerance of $\epsilon = 10^{-10}$ as the stopping criterion, with a maximum number of iterations of 20 and a single time step because it is a stationary study.

To solve this problem for the three-dimensional case, the mesh was considerably reduced as it can be shown in Figure 4.25. The grid is made up of 61,020 elements and 11,904 nodes, where the elements are tetrahedrons. The boundary layer will not be solved correctly for this case, but this problem can be

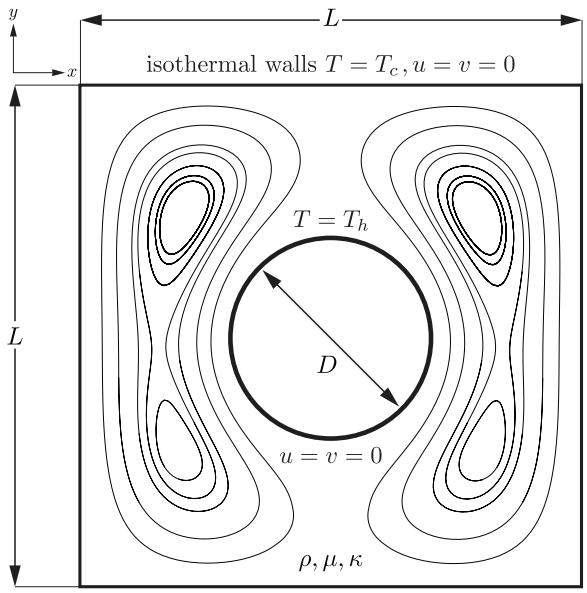

Figure 4.23: Physical domain with boundary conditions for the two-dimensional case.

validated by studying the behavior of the heat flow of the cylinder, which does not need such a refined mesh around the cylinder.

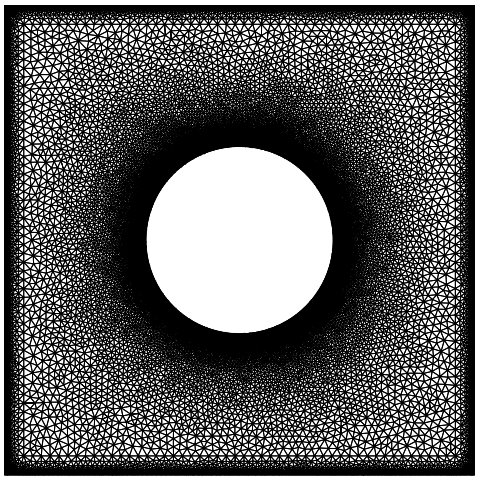

Figure 4.24: View of the grid for the two-dimensional case.

4.4.1 Test results and discussion

The simulations were carried out for a Reynolds number of Re = 1 and a Rayleigh number of Ra = 10^4. Figures 4.26, 4.27, and 4.28 show the results for the streamlines, the pressure contours and the temperature contours respectively for the two-dimensional case. It can be noted on those Figures how the steady behavior is reached and the fields are symmetrical about the vertical line that cuts the center of the circular cylinder.

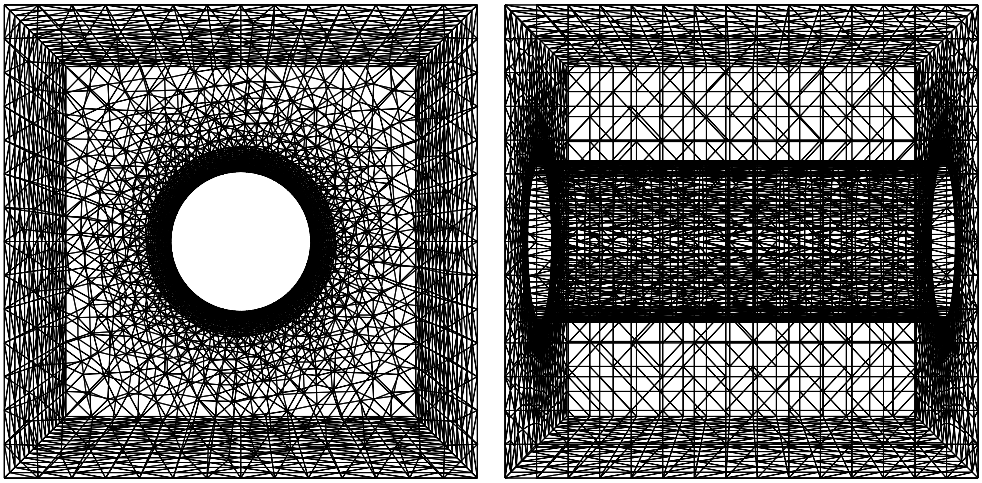

Figure 4.25: View of the grid fof the three-dimensional case.

The process occurs as follows, the heated fluid moves upward becoming gradually colder and denser until it reaches the isothermal cold surface of the square enclosure, and then it starts to change its direction producing symmetrical vortices as can be seen in Figure 4.26 and according to the pressure field shown in Figure 4.27. Also, Figure 4.28 shows how heat is transferred by conduction in the walls of the square enclosure.

The rate of heat transfer at the hot circular cylinder wall will be measured with the surface-averaged Nusselt number defined as

$$\overline{\mathrm{Nu}} = \frac{1}{W}\int_0^W \mathrm{Nu}\,\mathrm{d}S,$$

where $\mathrm{Nu} = -\partial T/\partial \mathrm{n}$ is the local Nusselt number with n denoting the normal direction to the cylinder surface and W is the cylinder surface area. To validate the results of the present work, the surface-averaged Nusselt number $\overline{\mathrm{Nu}}$ will be calculated for the two-dimensional and the three-dimensional case and be compared with those calculated in previous reported works by Asan [3], Kim et al. [15], and Hussain et al. [14].

Table 4.3 shows the results obtained in the present work and compared to the values obtained by the authors mentioned above. The results show a very good agreement with the reported values, where the value obtained for the three-dimensional case refers to a slice of the center of the three-dimensional domain as can be shown in Figures 4, 5 and 6.

Table 4.3: Comparison of surface-averaged Nusselt number for $\mathrm{Ra} = 10^4$

Present calculation				
2D	**3D**	[14]	[15]	[3]
3.407	3.427	3.4047	3.414	3.331

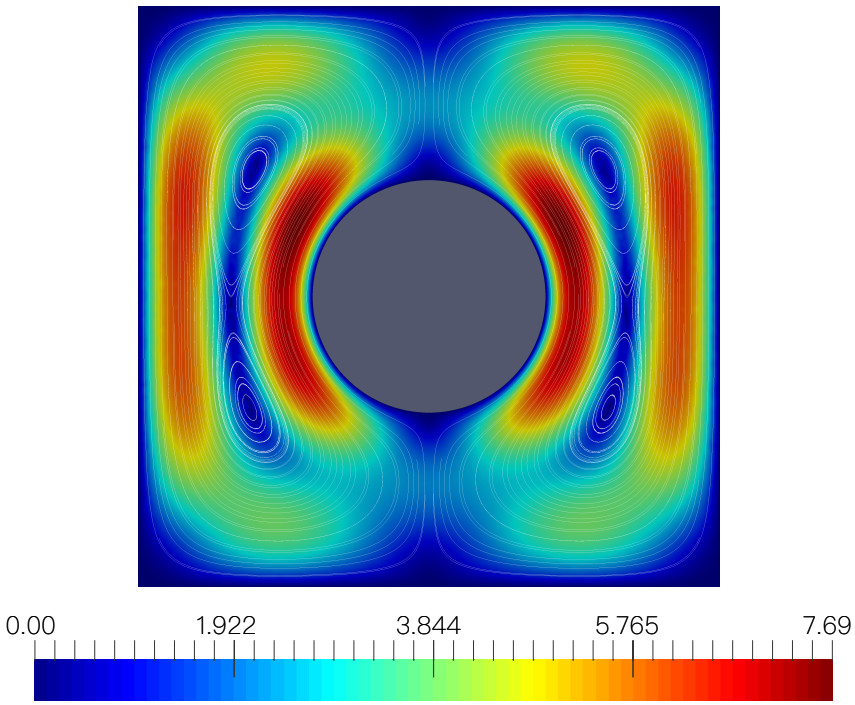

Figure 4.26: Streamlines at Ra = 10^4 for the two-dimensional case.

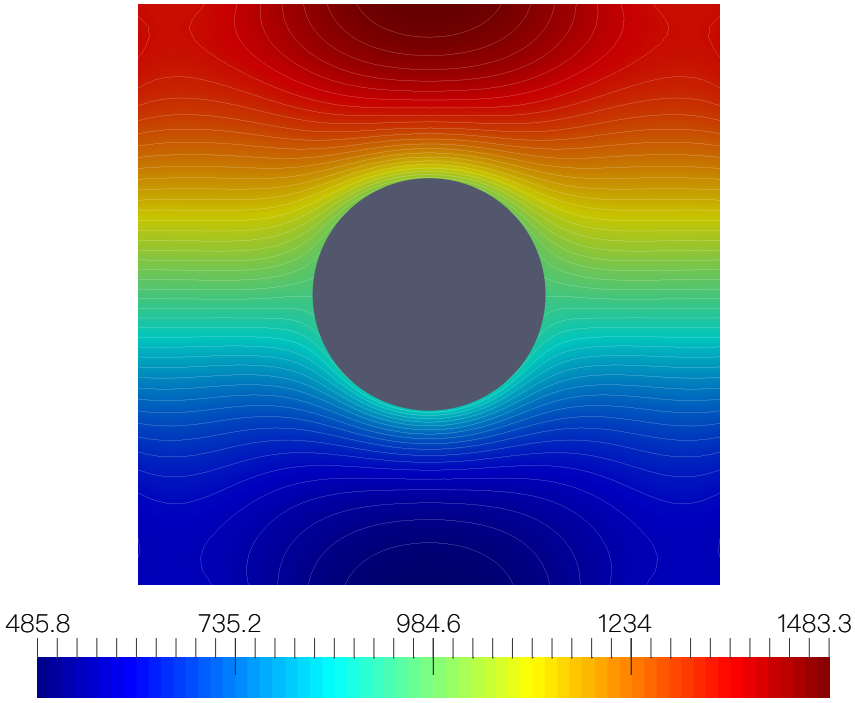

Figure 4.27: Pressure contours at Ra = 10^4 for the two-dimensional case.

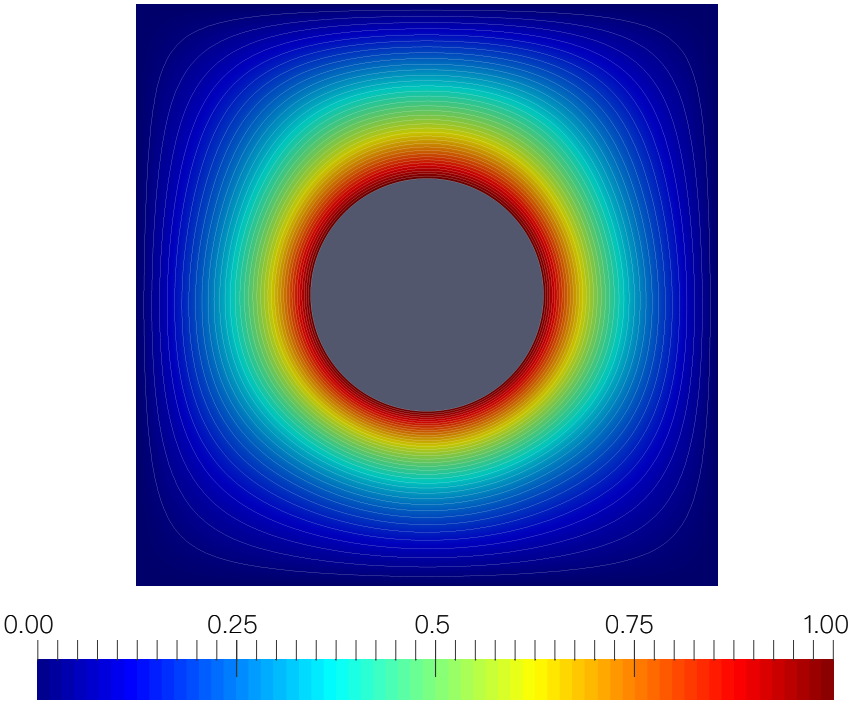

Figure 4.28: Temperature contours at $\mathrm{Ra} = 10^4$ for the two-dimensional case.

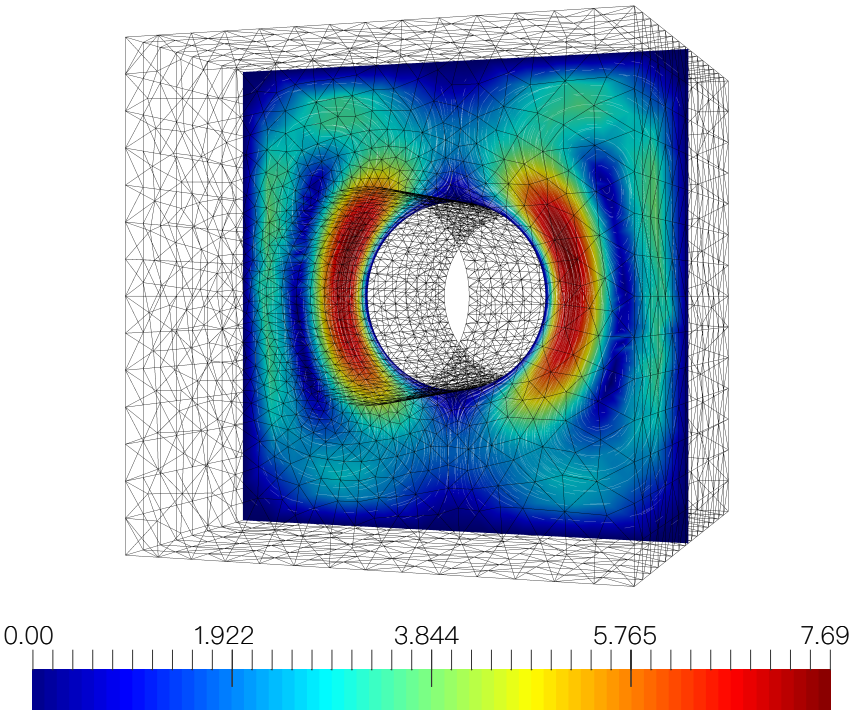

Figure 4.29: Streamlines at $\mathrm{Ra} = 10^4$ for the three-dimensional case.

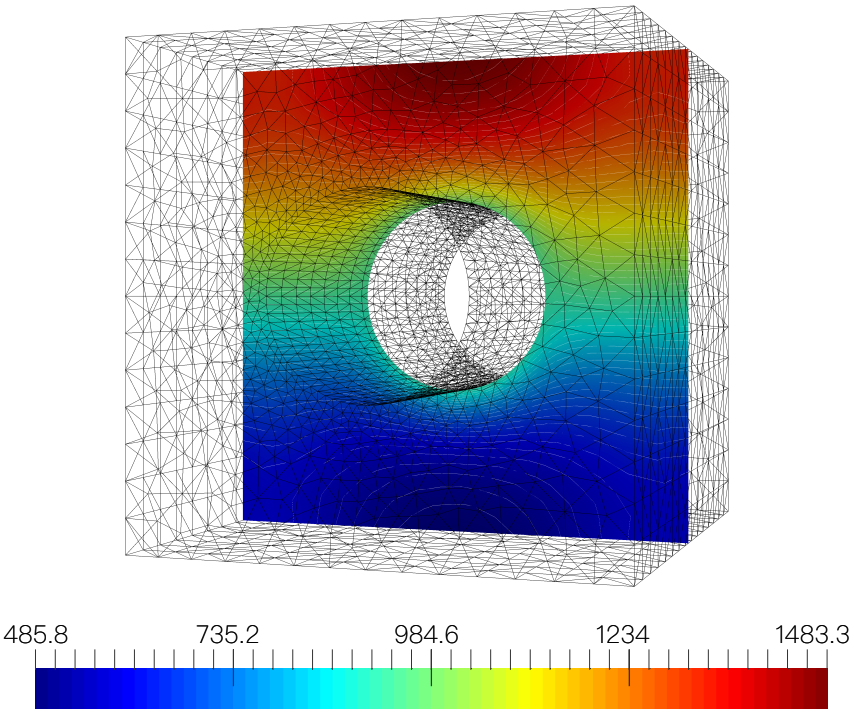

Figure 4.30: Pressure contours at Ra = 10^4 for the three-dimensional case.

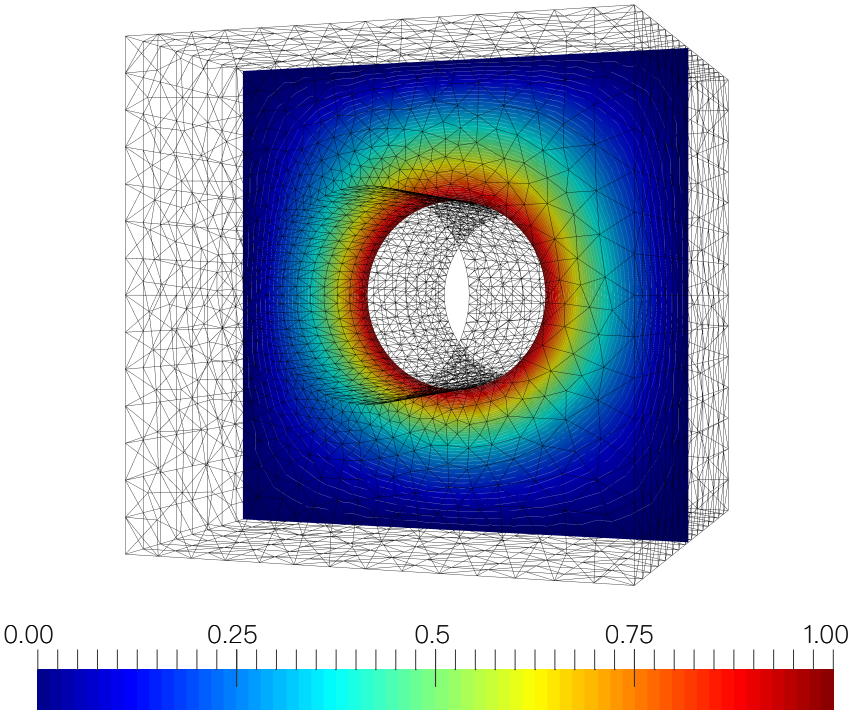

Figure 4.31: Temperature contours at Ra = 10^4 for the three-dimensional case.

Chapter 5

Results and discussion

Several scenarios were calculated to obtain a more realistic behavior of the wind, pressure, and temperature fields. The main idea is to solve the velocity, pressure, and temperature fields using the model for laminar and incompressible flow with heat transfer (2.4)-(2.6) describe in Section 2.5 but replacing the uniform flow imposed at the inlet with more realistic velocity and temperature profiles, as well as the physical domain used in previous validations tests.

The first scenario will be the flow past an ellipsoidal obstacle and the flow past two sinusoidal obstacles. These two configurations will be carried out for $\mathrm{Re} = 8000$ and, as a result of this Reynolds number, problem (2.12)-(2.14) will become a decoupled system due to $\mathrm{Ri} \to 0$. These scenarios were originally three-dimensional studies proposed by Qin et al [20] but were reduced to the two-dimensional case due to computational requirements. Therefore, only a slice of the center of the domains will be studied.

In the second scenario, the velocity, pressure, and temperature fields will be calculated for Reynolds numbers of $\mathrm{Re} = 10$, $\mathrm{Re} = 40$, and $\mathrm{Re} = 200$. In this case, the physical domain will be hills with a characteristic length of 500 m and 1 km respectively such as those used in the sinusoidal obstacles test and for a simulation height of 5 km. A velocity profile and uniform temperature were imposed at the inlet as well as a temperature profile on the hills. The third scenario will be similar to the second, but now a temperature profile will be imposed at the inlet, which will vary smoothly down to -10 degrees until it reaches a height of 2 km. The last scenario will be calculated for the same Reynold numbers used in the second and the third and for a Reynolds number of $\mathrm{Re} = 2000$. The physical domain will consist of a set of actual altitude data obtained from a GeoTIFF data file. A more realistic velocity and temperature profile will be imposed at the inlet, as well as a temperature profile for the terrain determined by the elevation dataset.

The model used in the present work has limitations that must be discussed. Fluid flow behavior can be classified as laminar, transitional, or turbulent flow. As shown in the test results for a Reynolds number range of 10 to 40 in Chapter 4, for laminar flow, the streamlines tend to follow a regular behavior that shows the formation of a symmetrical steady wake. In the case of turbulent flow, complex patterns will be appreciated and the streamlines will follow a chaotic behavior, therefore, the laminar model would no longer be useful due to the high Reynolds number, and a turbulence closure model such as the $k-\epsilon$ model [4] would be needed. In the case of the transition flow, it would be a mixture of laminar and turbulent flow. In this region, the flow will begin to become unstable and symmetry will be lost, as shown for a Reynolds number of 100 and 200 in Chapter 4.

Therefore, the model shown in the present work can be used up to the case of the transition flow. This model was tested for a Reynold numbers of 2000 and 8000, although laminar behavior was observed, it cannot guarantee that phenomena such as kinetic energy dissipation will be modeled correctly, as a turbulent model such as the $k-\epsilon$ model could. Furthermore, more powerful computational requirements would be needed to correctly solve a turbulent model, since to show the full behavior of turbulence, the

three-dimensional case [2] would be more appropriate.

5.1 First scenario

These configurations have been studied by Qin et al [20], and emulates a wind tunnel that is 4 m in x-coordinate, 1 m in y-coordinate and 3 m in z-coordinate. This scenario aims to qualitatively compare the results reported by Qin et al [20] with those obtained in the present work because their studies focused on the reconstruction of the wind field, therefore, their numerical model results for laminar and incompressible flow with heat transfer were not reported. Only the velocity field will be qualitatively compared because that is the result shown by Qin et al.

5.1.1 Forced convection flow past a heated ellipsoidal obstacle

A scheme of a forced convection flow past a 3D object can be shown in Figure 5.1, where a slice of the center of the domain will be taken as the two-dimensional domain for the present work. In this problem, the geometry will be an ellipsoidal one, which is surrounded by a fluid of mass density ρ, dynamic viscosity μ, and thermal conductivity κ. The height of the ellipsoidal model is 0.15 m. The original model can be shown in Figure 5.2, but only a slice of the center of the domain will be studied due to the computational requirements that were available for this work. The velocity, temperature, and pressure fields will be studied for a Reynolds number (Re) of 8000 and Prandtl number Pr = 0.7, under forced convection over the ellipsoidal model, and the Richardson number (Ri) can be taken as zero.

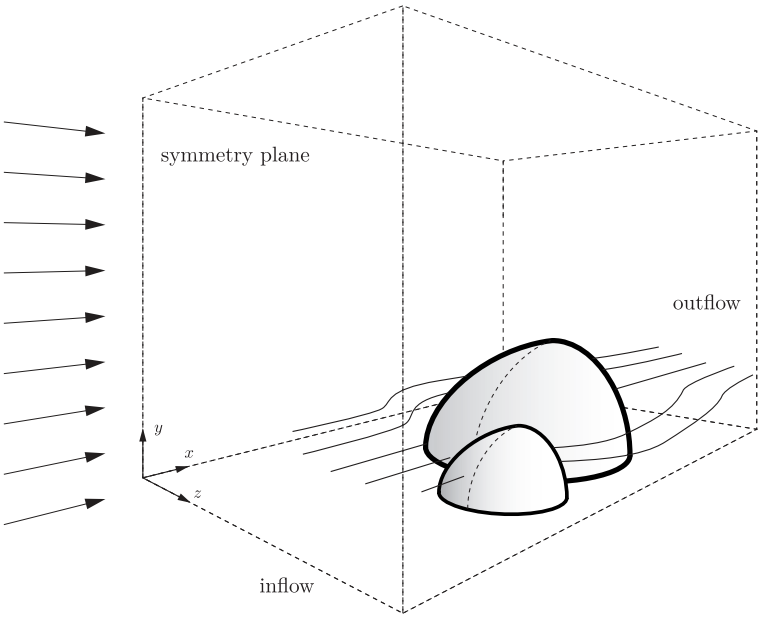

Figure 5.1: Physical domain, where a two-dimensional slice located on the vertical center plane will be taken for the ellipsoidal and sinusoidal numerical studies.

The velocity, pressure, and temperature fields are set to 0 at all points in the domain. At the inlet, the horizontal velocity component u is set to $u = 0.98$, and the vertical velocity component v is set to zero $v = 0$. Also, an uniform temperature profile is set as $T = 0$ at the inlet. At the top wall, symmetry boundary conditions are imposed, setting the velocity and temperature gradients to zero

$v = \partial u/\partial y = \partial T/\partial y = 0$. At the outlet, the pressure, velocity gradient and temperature gradient are set to zero $v = p = \partial u/\partial x = \partial T/\partial x = 0$. At the surfaces of the obstacles, the no-slip condition $u = v = 0$ and a uniform temperature $T_{\mathrm{w}} = 1$ will be imposed.

The grid used for computations is shown in Figure 5.3. Small triangular elements were generated around the ellipsoidal geometry and in the wake region, whereas the size of the elements becomes thicker in the inlet region of the domain. The grid is made up of 173,639 elements and 87,488 nodes. The dimensions of the wind tunnel $4 \times 1 \times 3$ m will be taken as dimensionless. To correctly solve the viscous effects, the maximum thickness of the boundary layer was 0.05. On the bottom wall and considering the ellipsoidal geometry, the mesh size was 0.001 and gradually varied to 0.005 until it reached the thickness of the boundary layer. In the wake region and over the ellipsoidal geometry, the elements become a little bigger to correctly solve the behavior of the flow until they reached the size of 0.008.

The iterative method was carried out using a tolerance of $\epsilon = 10^{-5}$ as the stopping criterion, with a maximum number of iterations of 20 and a final dimensionless time of 1 with a time step of 0.1.

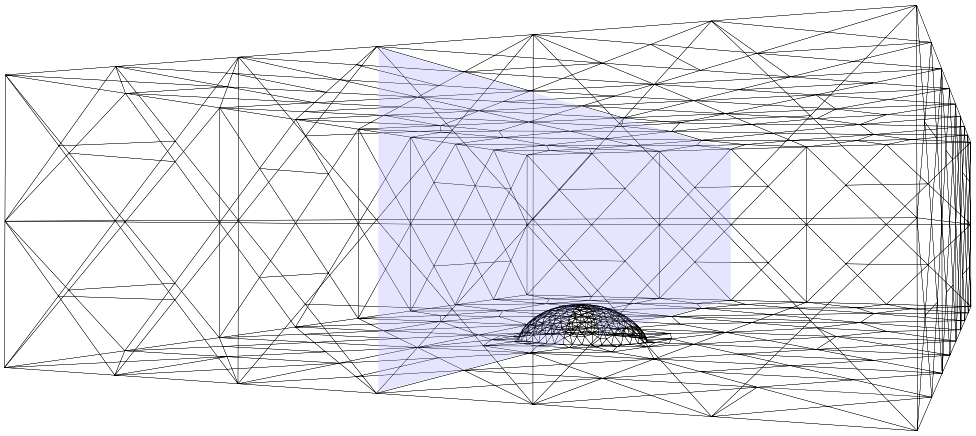

Figure 5.2: View of the grid for the ellipsoidal numerical study used by Qin et al [20], where a two-dimensional slice located on the vertical center plane will be taken for the ellipsoidal numerical study.

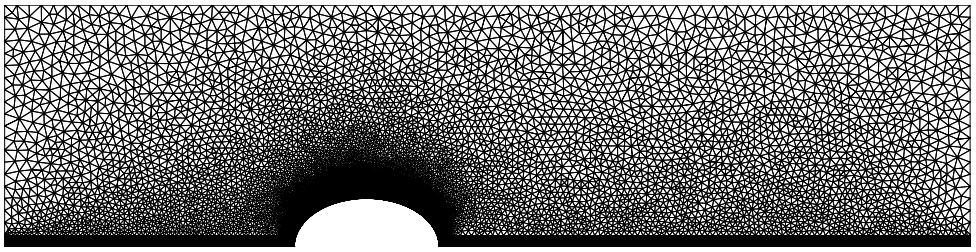

Figure 5.3: View of the grid of the two-dimensional slice for the ellipsoidal numerical study.

Scenario results and discussion

The simulations were carried out for a Reynolds number of Re = 8000. The validation focused on the velocity field study to be qualitatively compared with the results shown by Qin et al [20], where the test was calculated for a velocity of 8.5 m/s at the inlet. Although a turbulence model would be required for this velocity, the behavior of the fluid flow will still have to change from laminar to turbulent, with the difference that it will occur faster than in the case of a lower Reynolds number.

Following this idea, the velocity field obtained for a dimensionless time of 0.2 in the present work, when the flow still behaved as laminar, showed the same behavior as those shown by Qin et al. [20]. This happened just before the boundary layer detachment occurred as can be seen in Figure 5.4, where a zone of zero velocity can be observed on the left side of the ellipsoidal obstacle due to the no-slip condition on the obstacle and how a slight detachment of the boundary layer begins at the top and on the right side of the obstacle. A Reynolds number of Re = 8000 was used because it is the maximum number that our code works on.

The pressure field can be seen in Figure 5.5, where it shows the maximum pressure on the left side of the obstacle where the wind flow changes its direction, which refers to the stagnation point and the minimum pressure is above the ellipsoidal obstacle that is consistent with the result of the velocity field where the velocity is maximum.

The temperature field is also shown in Figure 5.6, where can be noticed how the boundary layer starts to detach on the right side of the ellipsoidal obstacle.

Taking into account that the air has a mass density of $\rho = 1.22$ Kg/m^3, and a dynamic viscosity of 1.78×10^{-5} Kg/m $\cdot$ s; for the case of a characteristic length of 0.15 m, the velocity for a Reynolds number of Re = 8000 would be 0.78 m/s.

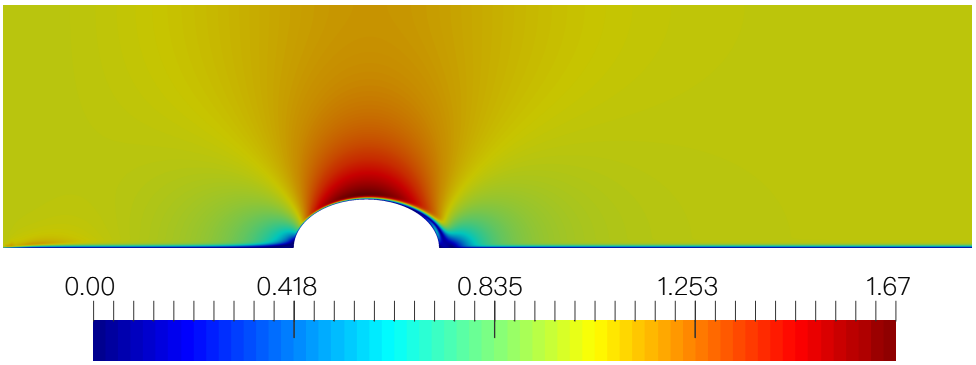

Figure 5.4: Velocity field of the two-dimensional ellipsoidal study.

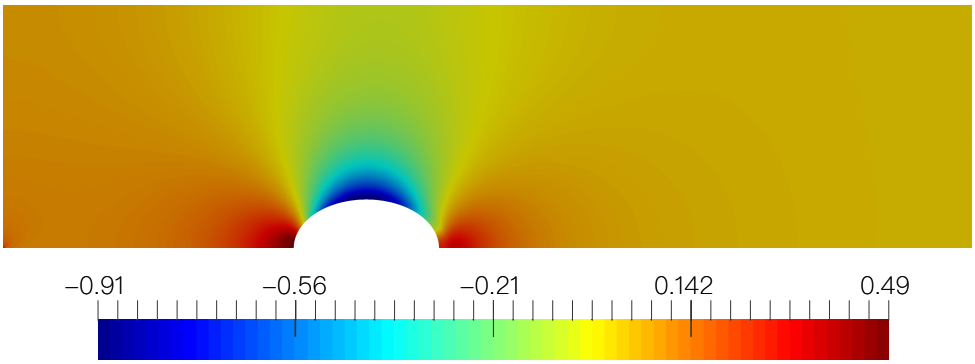

Figure 5.5: Pressure field of the two-dimensional ellipsoidal study.

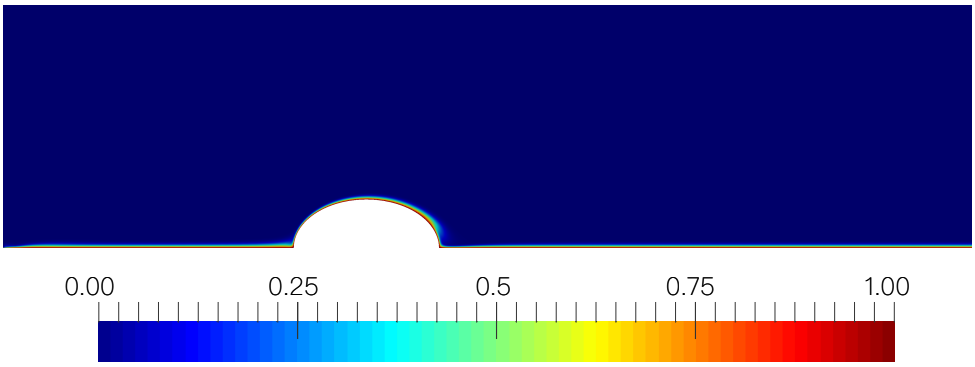

Figure 5.6: Temperature field of the two-dimensional ellipsoidal study.

5.1.2 Forced convection flow past two heated sinusoidal obstacles

A scheme for this problem is equivalent to the one shown in Figure 5.1, but now the geometry will be two sinusoidal obstacles, which are surrounded by a fluid of mass density ρ, dynamic viscosity μ, and thermal conductivity κ. The height of the largest sinusoidal obstacle is 0.20 m and the smallest is 0.15 m. The original model can be shown in Figure 5.7, but as it was done for the ellipsoidal case, only a slice of the center of the domain will be studied due to the computational requirements that were available for this work. The velocity, temperature, and pressure fields will be studied for a Reynolds number (Re) of 8000 and Prandtl number Pr = 0.7, under forced convection over the sinusoidal model, and the Richardson number (Ri) can be taken as zero. In this case, the boundary conditions are exactly the same as those used in the ellipsoidal case.

The grid used for computations is shown in Figure 5.8. Small triangular elements were generated around the sinusoidal geometry and in the wake region, whereas the size of the elements becomes thicker in the inlet region of the domain. The grid is made up of 214,851 elements and 108,232 nodes. The dimensions of the wind tunnel will be taken as dimensionless. To correctly solve the viscous effects, the maximum thickness of the boundary layer was 0.05. On the bottom wall and considering the sinusoidal geometry, the mesh size was 0.001 and gradually varied to 0.005 until it reached the thickness of the boundary layer. In the wake region and over the ellipsoidal geometry, the elements become a little bigger to correctly solve the behavior of the flow until they reached the size of 0.008.

The iterative method was carried out using a tolerance of $\epsilon = 10^{-5}$ as the stopping criterion, with a maximum number of iterations of 20 and a final dimensionless time of 1 with a time step of 0.1.

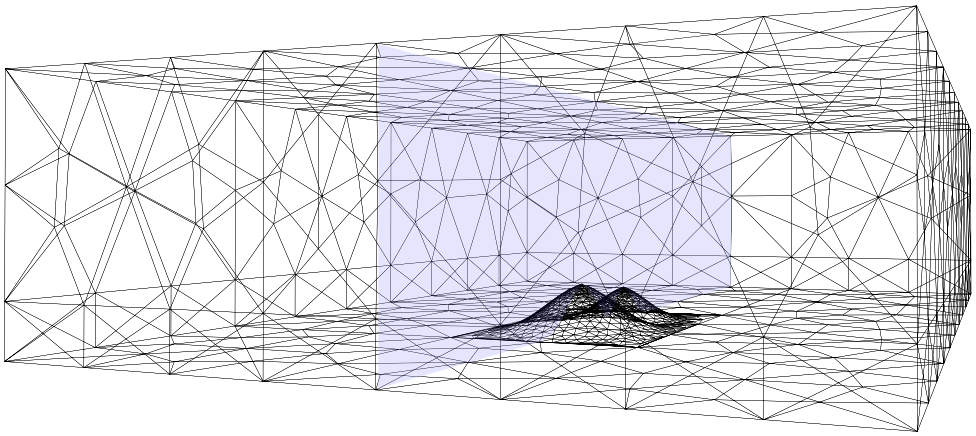

Figure 5.7: View of the grid for the sinusoidal numerical study used by Qin et al [20], where a two-dimensional slice located on the vertical center plane will be taken for the sinusoidal numerical study.

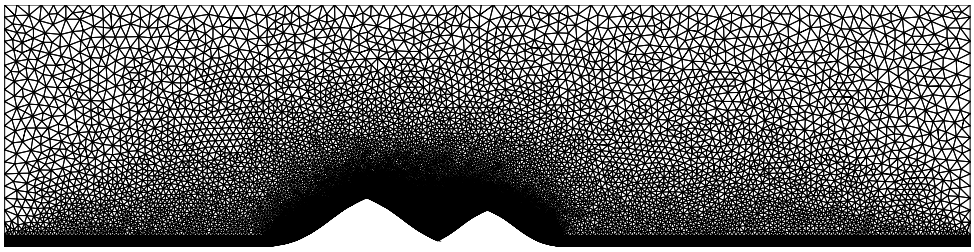

Figure 5.8: View of the grid of the two-dimensional slice for the sinusoidal numerical study.

Scenario results and discussion

The simulations were carried out for a Reynolds number of $\mathrm{Re} = 8000$. The validation focused on the velocity field study to be qualitatively compared with the results reported by Qin et al [20] following the same idea shown in the previous case for the ellipsoidal obstacle. Same behavior was observed before the boundary layer detachment occurred as can be seen in Figure 5.9, where a zone of zero velocity can be observed on the left and right side of the sinusoidal obstacles due to the no-slip condition on the obstacles and how a slight detachment of the boundary layer begins at the tops of the obstacles. The pressure field can be seen in Figure 5.10, where it shows the maximum pressure on the left side of the highest obstacle and between them, and the minimum pressure is above the sinusoidal obstacles that are consistent with the result of the velocity field where the velocity is maximum. The temperature field is also shown in Figure 5.11, where can be noticed how the boundary layer starts to detach on the top of the sinusoidal obstacles.

Taking into account that the air has a mass density of $\rho = 1.22$ Kg/m^3, and a dynamic viscosity of 1.78×10^{-5} Kg/m $\cdot$ s; for the case of a characteristic length of 0.2 m, the velocity for a Reynolds number of $\mathrm{Re} = 8000$ would be 0.58 m/s.

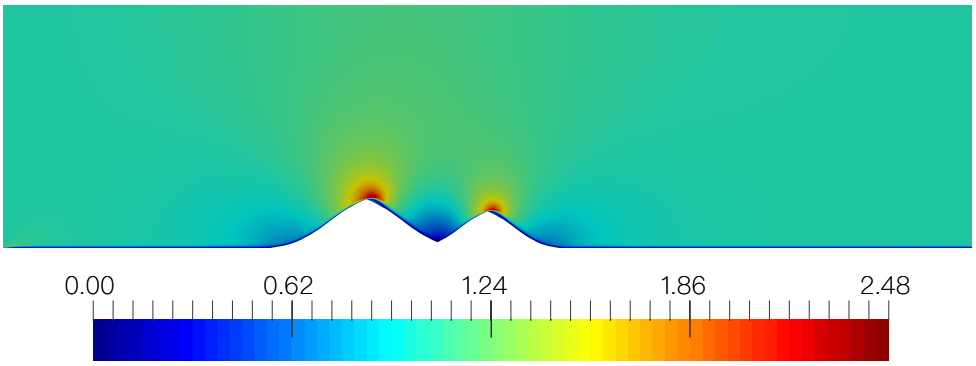

Figure 5.9: Velocity field of the two-dimensional sinusoidal study.

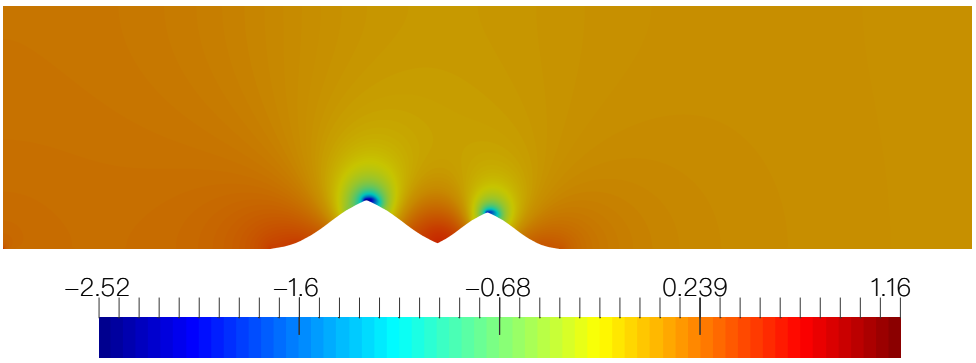

Figure 5.10: Pressure field of the two-dimensional sinusoidal study.

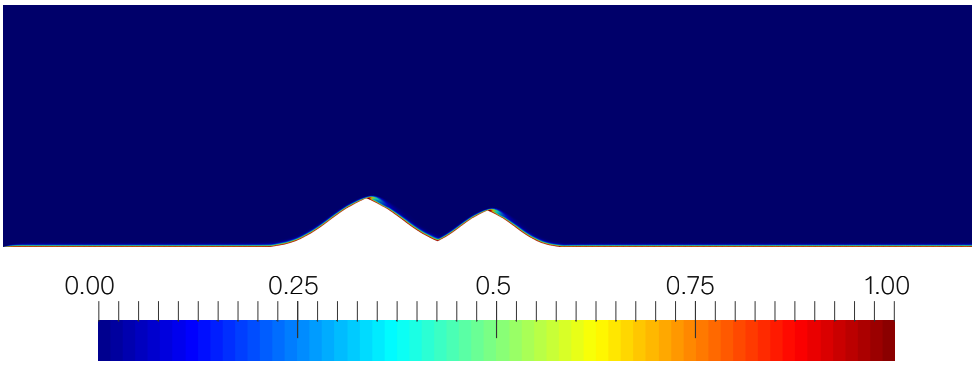

Figure 5.11: Temperature field of the two-dimensional sinusoidal study.

5.2 Second scenario

In engineering applications, a power-law wind profile is often used to model wind behavior. Accurate results have been obtained over the water and open land surfaces with the following profile [13]

$$\frac{u}{u_r} = \left(\frac{h}{h_r}\right)^{\alpha}, \tag{5.1}$$

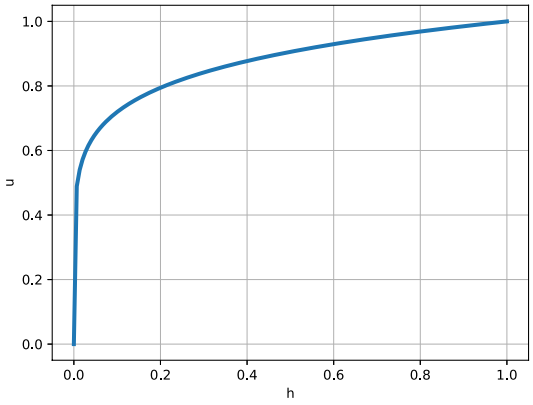

Figure 5.12: Power-law wind profile used to model wind behavior at the inlet.

where u is the wind velocity at height h, u_r is the known wind velocity at a reference height h_r, and the exponent α is a coefficient that depends on the stability of the atmosphere. For the open sea, the coefficient α is approximately $\alpha = 0.10$, while for open land it is taken as $\alpha = 0.143$, which is the coefficient that will be used in the current computations. This profile can be seen in Figure 5.12.

According to the International Standard Atmosphere [19], it has been established a model to calculate the temperature as a function of altitude above sea level, which is only valid for the troposphere, the lowest part of the atmosphere. This model states the following for the dimensionless case

$$\frac{T}{T_0} = 1 - L\left(\frac{h}{h_r}\right), \tag{5.2}$$

where T is the temperature at height h and T_0 is the known sea level standard temperature. It can be seen that if $h = 0$ is taken as the height of the sea level, a dimensionless temperature of $T/T_0 = 1$ would correspond to this height, which is the dimensionless sea level standard temperature, and $L = 6.5$ is the dimensionless temperature lapse rate, which would have K/km as a physical dimension. This profile can be seen in Figure 5.13.

In this case, the boundary conditions will change. The velocity, pressure, and temperature fields are set to 0 at all points in the domain. The wind profile (5.1) is imposed at the inlet, where the vertical velocity component v is set to zero $v = 0$, which will also be set to zero for the entire domain and the temperature profile (5.2) is also set at the inlet. At the top wall, symmetry boundary conditions are imposed, setting the velocity and temperature gradients to zero $v = \partial u/\partial y = \partial T/\partial y = 0$. At the outlet, the pressure, velocity gradient and temperature gradient are set to zero $v = p = \partial u/\partial x = \partial T/\partial x = 0$. Finally, at the hills surface, the no-slip condition will be imposed $u = v = 0$ as well as the temperature profile (5.2).

The computational domain used for this scenario had a dimensionless height of 1 and dimensionless width of 4, corresponding to 5 km and 20 km respectively, with $h_r = 5$ km. The grids used for computations are shown in Figure 5.14 and 5.15 for the hills with a characteristic length of 500 m and 1 km respectively. The dimensionless characteristic length will be 0.1 and 0.2 for the hills of 500 m and 1 km respectively. Small triangular elements were generated around the hills and in the wake region, whereas the size of the elements becomes thicker in the rest of the domain. The grid is made up of 142,932 elements and 72,608 nodes for the 500m hills and is made up of 133,370 elements and 67,626 nodes for the 1 km hills. The mesh size on the bottom wall and hills surface was 0.003 and this size of the elements gradually varied to 0.008 in the rest of the domain.

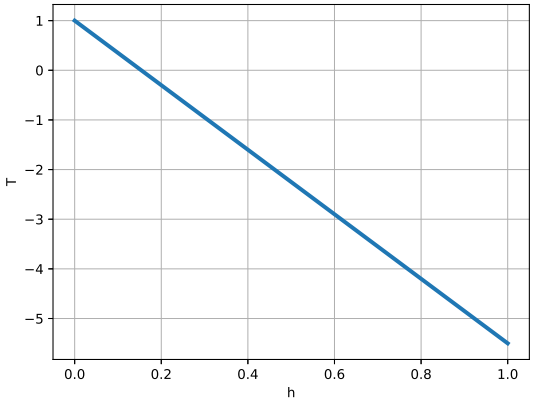

Figure 5.13: Temperature profile used to model temperature behavior at the troposphere.

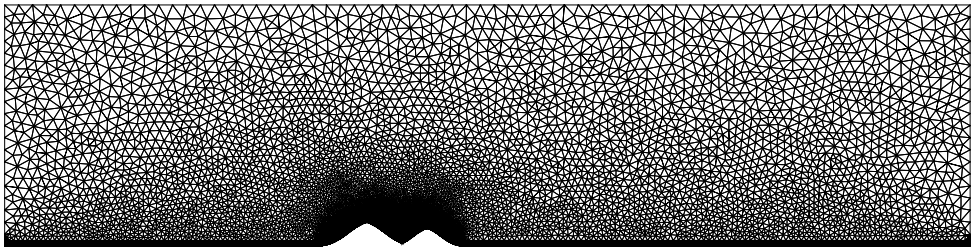

Figure 5.14: View of the grid of the two-dimensional hills with a characteristic length of 500 m.

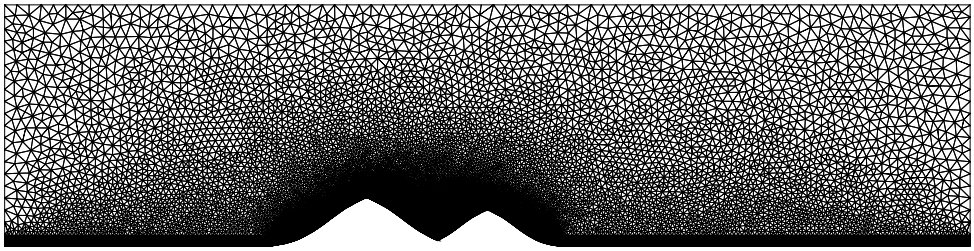

Figure 5.15: View of the grid of the two-dimensional hills with a characteristic length of 1 Km.

The iterative method was carried out using a tolerance of $\epsilon = 10^{-5}$ as the stopping criterion, with a maximum number of iterations of 20 and a final dimensionless time of 10 with a time step of 0.1.

5.2.1 Scenario results and discussion

The model was computed for a Prandtl number of Pr = 0.7, under forced convection with a Richardson number of Ri = 0.

In the case of the characteristic length of 0.1, figure 5.16 shows the velocity field obtained for a Reynolds number of Re = 10, Re = 40, and Re = 200 respectively. From the Figure, a laminar behavior can be appreciated and how the thickness of the boundary layer decreases as the Reynolds number increases, which is an expected result because the higher the Reynolds number, the lower the viscous forces and therefore the thickness of the boundary layer is inversely proportional to the Reynolds number. Furthermore, a slight disturbance of the velocity field is observed just above the hills due to the no-slip condition on the hill surface, which can be easily noticed as the boundary layer decreases.

The pressure field can be seen in Figure 5.17 for a Reynolds number of Re = 10, Re = 40, and Re = 200 respectively , where it shows how the pressure is highest at the inlet and gradually decreases to zero once the outlet is reached, which is consistent with the result of the velocity field since, without this pressure difference, the fluid flow would not be possible. Also, stagnation areas are visible on the surface of the hills.

Figure 5.18 shows the temperature field obtained for a Reynolds number of Re = 10, Re = 40, and Re = 200 respectively. It can be seen how the low-temperature part of the profile at the inlet cannot reach the output with a low Reynolds number. This happens due to the low velocity at the inlet and the temperature profile imposed on the hills, which heat that part of the physical domain, while for a higher number of Reynolds, the temperature profile begins to appear completely downstream, as can be seen for the case of Re = 200. The slight disturbance of the temperature field is observed just above the hills due to their temperature profile on the hill surface, which can be easily noticed as the Reynolds number increases.

In the case of the characteristic length of 0.2, Figure 5.19 shows the velocity field obtained for a Reynolds number of Re = 10, Re = 40, and Re = 200 respectively. Similar results are obtained as in Figure 5.16, but now the disturbance of the velocity field on the hills due to the no-slip condition is better observed because the height of the hills is twice that of the previous ones. Furthermore, the thickness of the boundary layer has increased due to the height of the hills.

Figure 5.20 shows the pressure field obtained for a Reynolds number of Re = 10, Re = 40, and Re = 200 respectively. The same behavior is observed as those obtained in Figure 5.17 but in this case, lower stagnation areas are shown as can be easily seen at the top of the hills.

Figure 5.21 shows the temperature field obtained for a Reynolds number of Re = 10, Re = 40, and Re = 200 respectively. Similar results are obtained as in Figure 5.18. Because the height of the hills is twice that of the previous ones, a lower temperature can be noticed at the top of the hills. Now, a slightly lower temperature can be seen in the region around the hills and downstream compared to the previous results shown in Figure 5.18.

Taking into account that the air has a mass density of $\rho = 1.22$ Kg/m^3, and a dynamic viscosity of 1.78×10^{-5} Kg/m $\cdot$ s; for the case of a characteristic length of 1000 m, the velocity u_r for a Reynolds number of Re = 10, Re = 40, and Re = 200 would be 1.45×10^{-7}, 5.83×10^{-7}, and 2.91×10^{-6} m/s respectively. For the case of a characteristic length of 500 m, the velocity for a Reynolds number of Re = 10, Re = 40, and Re = 200 would be 2.91×10^{-7}, 1.17×10^{-6}, and 5.83×10^{-6} m/s respectively.

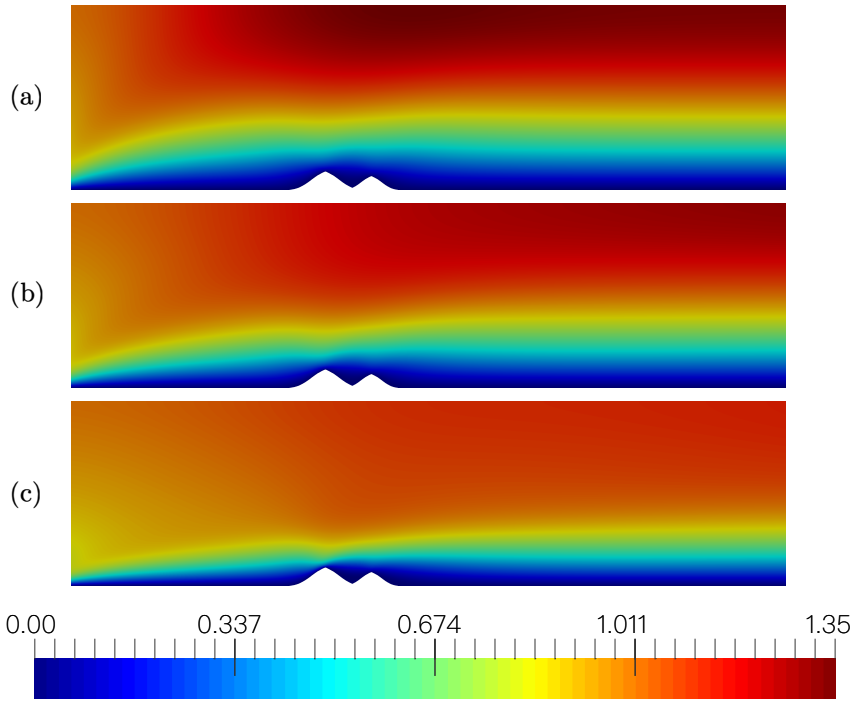

Figure 5.16: Velocity fields for hills with a dimensionless characteristic length of 0.1 for (a) Re = 10, (b) Re = 40, and (c) Re = 200.

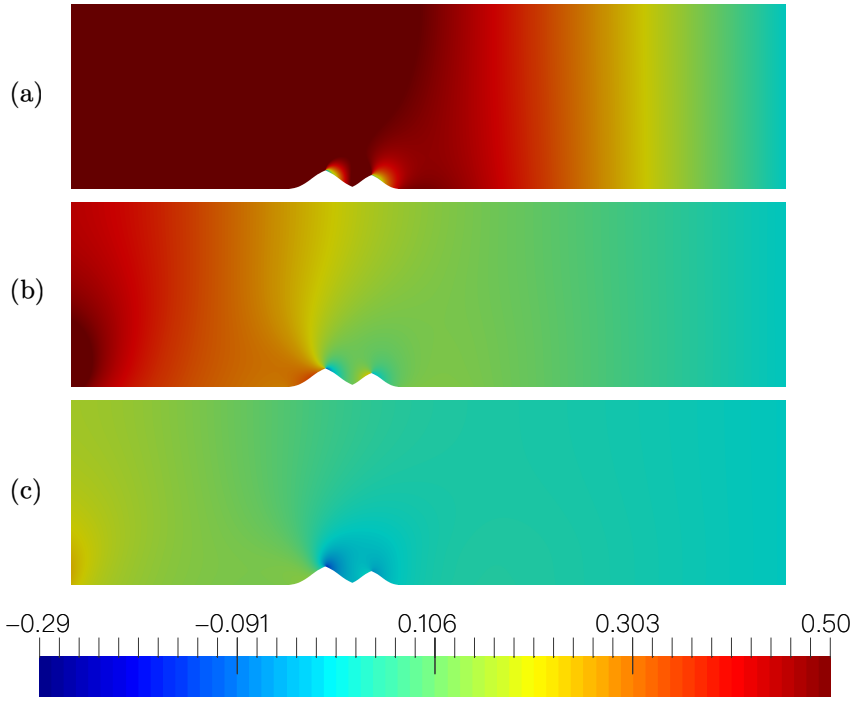

Figure 5.17: Pressure fields for hills with a dimensionless characteristic length of 0.1 for (a) Re = 10, (b) Re = 40, and (c) Re = 200.

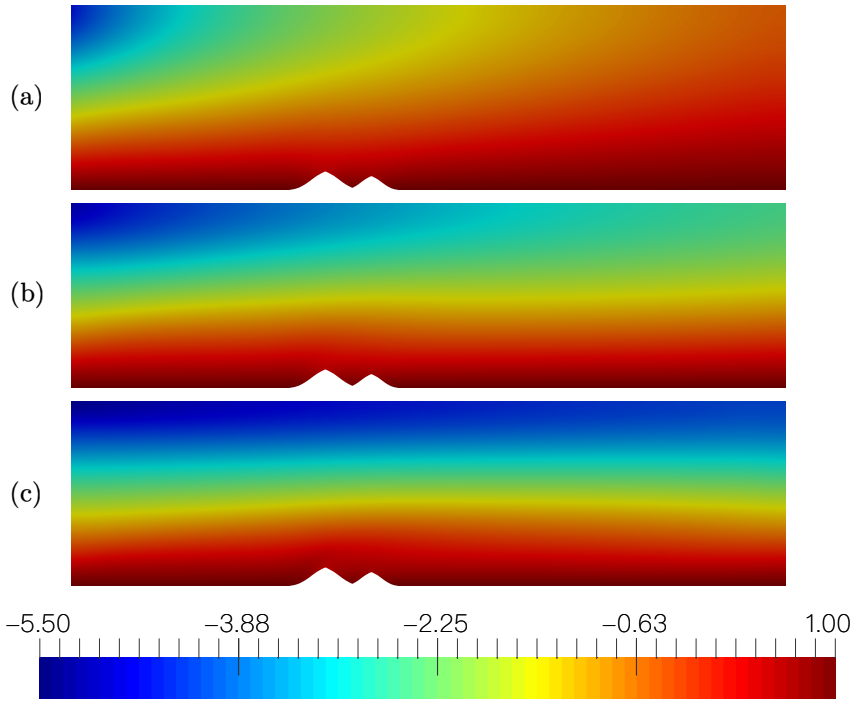

Figure 5.18: Temperature fields for hills with a dimensionless characteristic length of 0.1 for (a) Re = 10, (b) Re = 40, and (c) Re = 200.

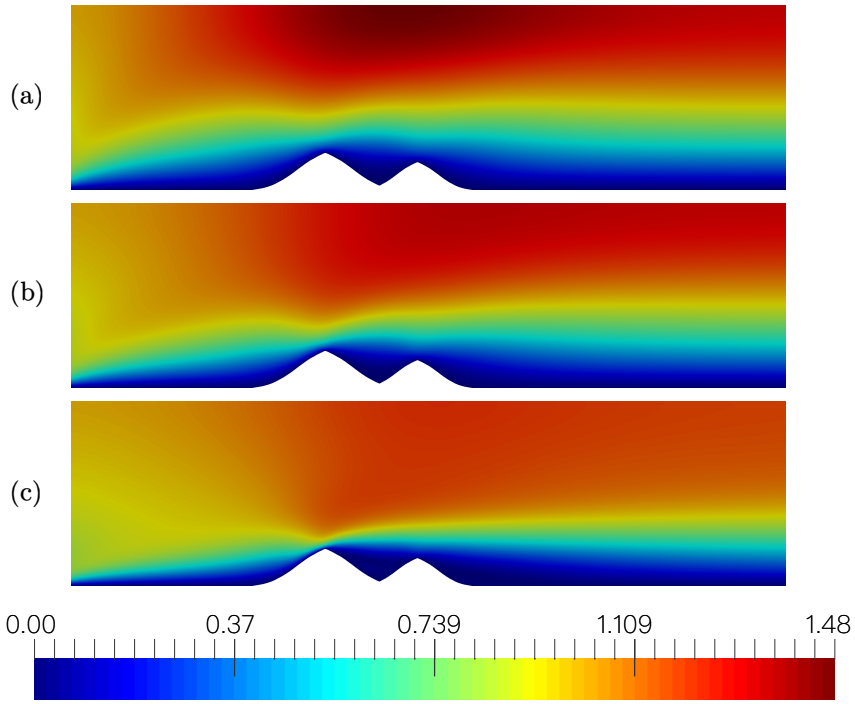

Figure 5.19: Velocity fields for hills with a dimensionless characteristic length of 0.2 for (a) Re = 10, (b) Re = 40, and (c) Re = 200.

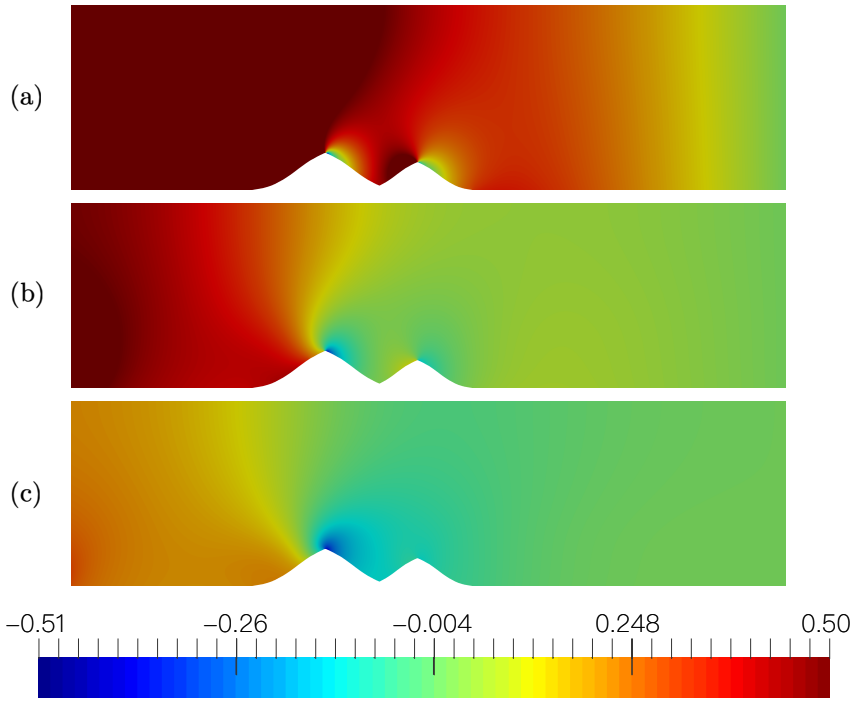

Figure 5.20: Pressure fields for hills with a dimensionless characteristic length of 0.2 for (a) Re = 10, (b) Re = 40, and (c) Re = 200.

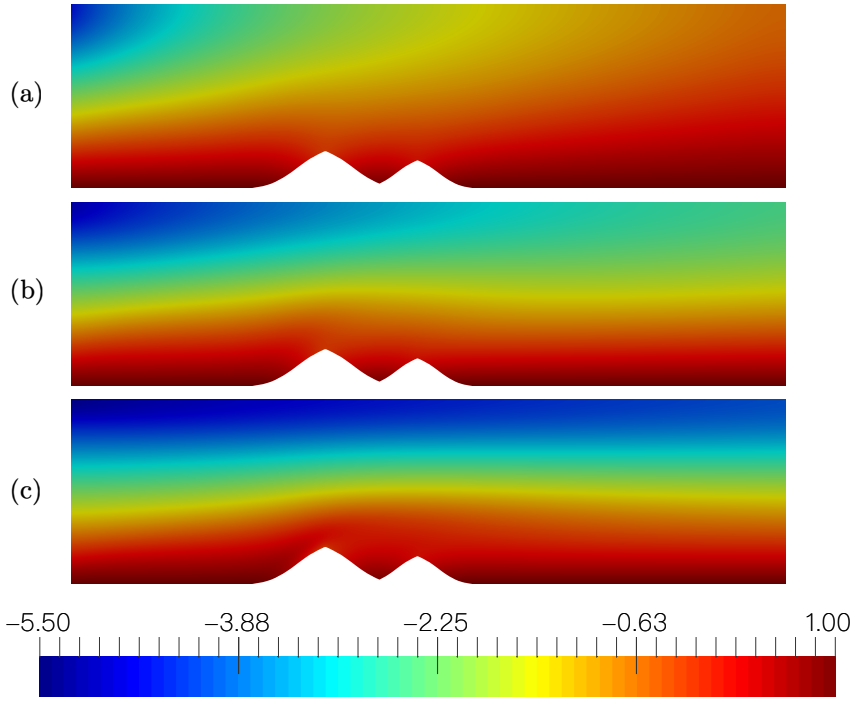

Figure 5.21: Temperature fields for hills with a dimensionless characteristic length of 0.2 for (a) Re = 10, (b) Re = 40, and (c) Re = 200.

5.3 Third scenario

For this scenario, the same procedure as the first one will be used with the difference that now for the boundary conditions, the temperature at the inlet is replaced by a temperature profile that will vary smoothly to -10 degrees until it reaches a dimensionless height of 0.4, corresponding to 2 km, which is a profile required by Microflown Technologies. The profile can be shown in Figure 5.22. The computational domains will remain as those in previous scenario, shown in Figure 5.14 and 5.15, as well as the same parameters used in the previous iterative method.

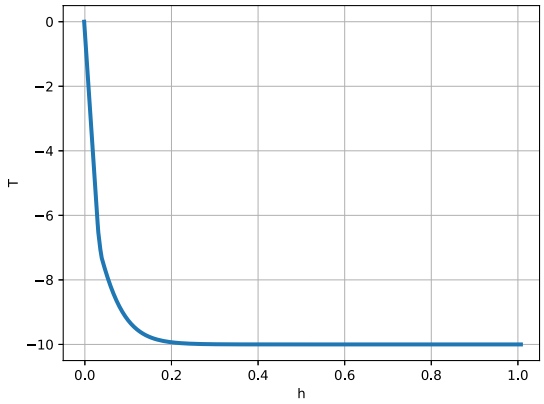

Figure 5.22: Temperature profile used to model temperature behavior at the inlet.

5.3.1 Scenario results and discussion

For this scenario, the same results were obtained as the previous scenario for the velocity and pressure fields. Both for the case of a characteristic length of 0.1 and 0.2 as can be seen in Figures 5.23, 5.24, and 5.26, 5.27 respectively.

The difference lies in the temperature fields shown in Figures 5.25 and 5.28 for the case of a characteristic length of 0.1 and 0.2 respectively, because temperature profile 5.22 has been imposed at the inlet, while in the previous case the profile was the one shown in Figure 5.13.

Figures 5.25 shows the temperature field obtained for a Reynolds number of $\mathrm{Re} = 10$, $\mathrm{Re} = 40$, and $\mathrm{Re} = 200$ respectively for the case of a characteristic length of 0.1. It can be seen how thermal convection is capable of reaching the upper wall of the physical domain for a low Reynolds number, while for a higher Reynolds number, the heat flow is confined downstream due to the increased velocity. The region above the hills is disturbed due to their temperature profile that causes the temperature to decrease with height. It is shown how the region between the hills has a higher temperature than the top of the hills. For the case of a characteristic length of 0.2, Figure 5.28 shows how the temperature has decreased in the region over the hills because now the hills are twice as high as before.

Taking into account that the air has a mass density of $\rho = 1.22$ Kg/m^3, and a dynamic viscosity of 1.78×10^{-5} Kg/m $\cdot$ s; for the case of a characteristic length of 1000 m, the velocity u_r for a Reynolds number of $\mathrm{Re} = 10$, $\mathrm{Re} = 40$, and $\mathrm{Re} = 200$ would be 1.45×10^{-7}, 5.83×10^{-7}, and 2.91×10^{-6} m/s respectively. For the case of a characteristic length of 500 m, the velocity for a Reynolds number of $\mathrm{Re} = 10$, $\mathrm{Re} = 40$, and $\mathrm{Re} = 200$ would be 2.91×10^{-7}, 1.17×10^{-6}, and 5.83×10^{-6} m/s respectively.

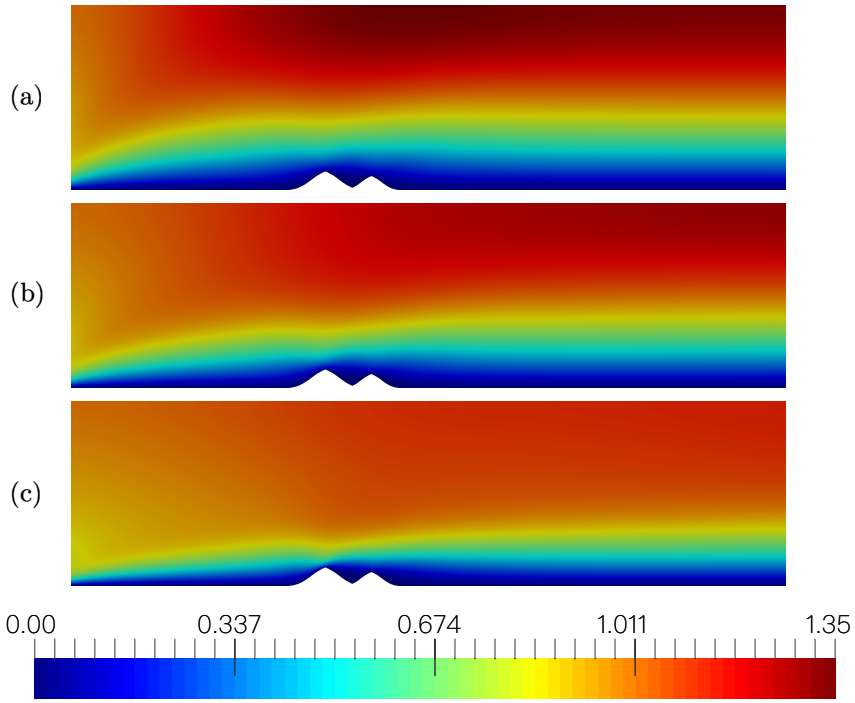

Figure 5.23: Velocity fields for hills with a dimensionless characteristic length of 0.1 for (a) Re = 10, (b) Re = 40, and (c) Re = 200.

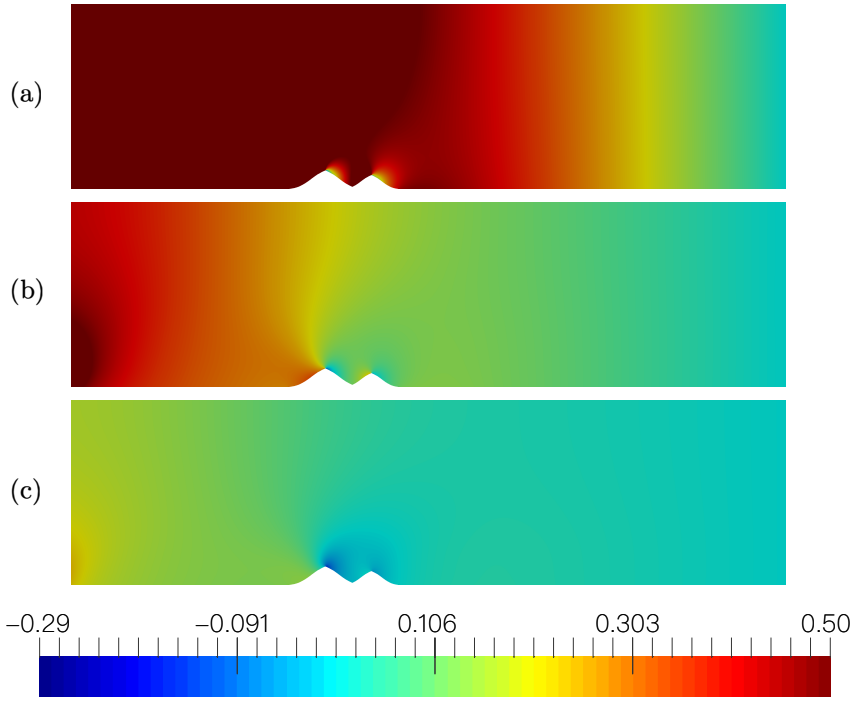

Figure 5.24: Pressure fields for hills with a dimensionless characteristic length of 0.1 for (a) Re = 10, (b) Re = 40, and (c) Re = 200.

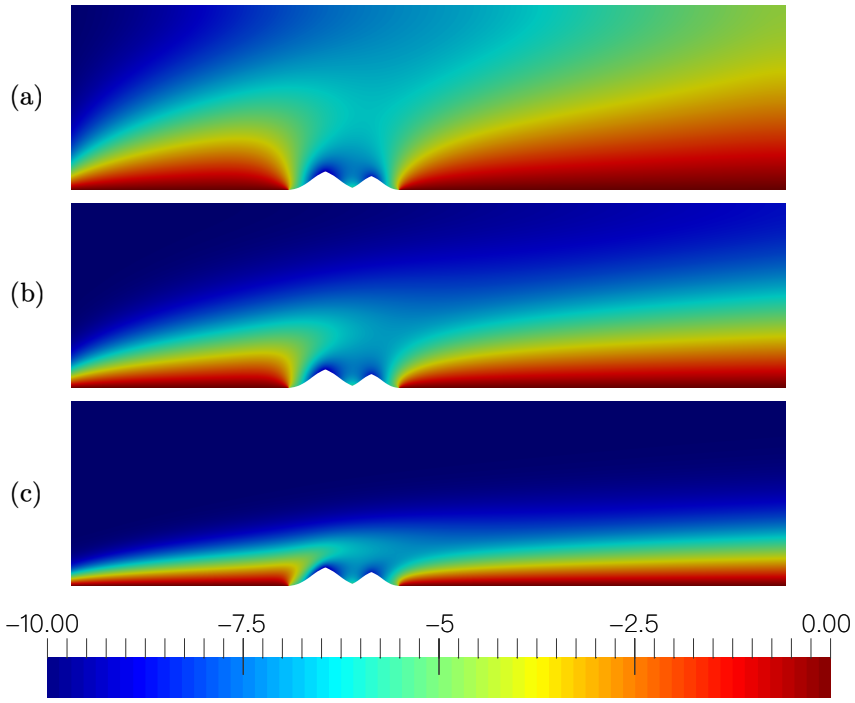

Figure 5.25: Temperature fields for hills with a dimensionless characteristic length of 0.1 for (a) Re = 10, (b) Re = 40, and (c) Re = 200.

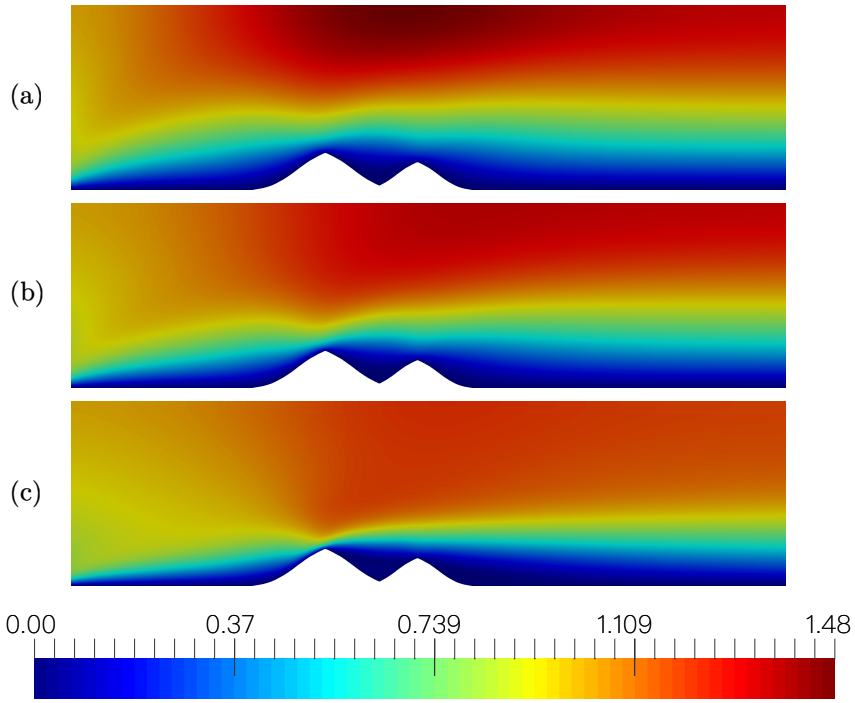

Figure 5.26: Velocity fields for hills with a dimensionless characteristic length of 0.2 for (a) Re = 10, (b) Re = 40, and (c) Re = 200.

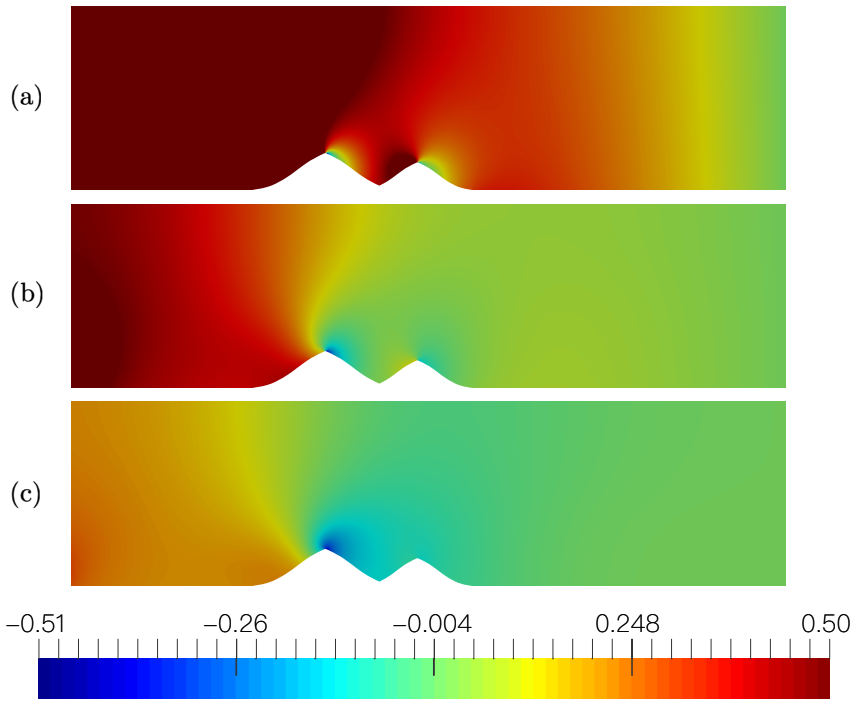

Figure 5.27: Pressure fields for hills with a dimensionless characteristic length of 0.2 for (a) Re = 10, (b) Re = 40, and (c) Re = 200.

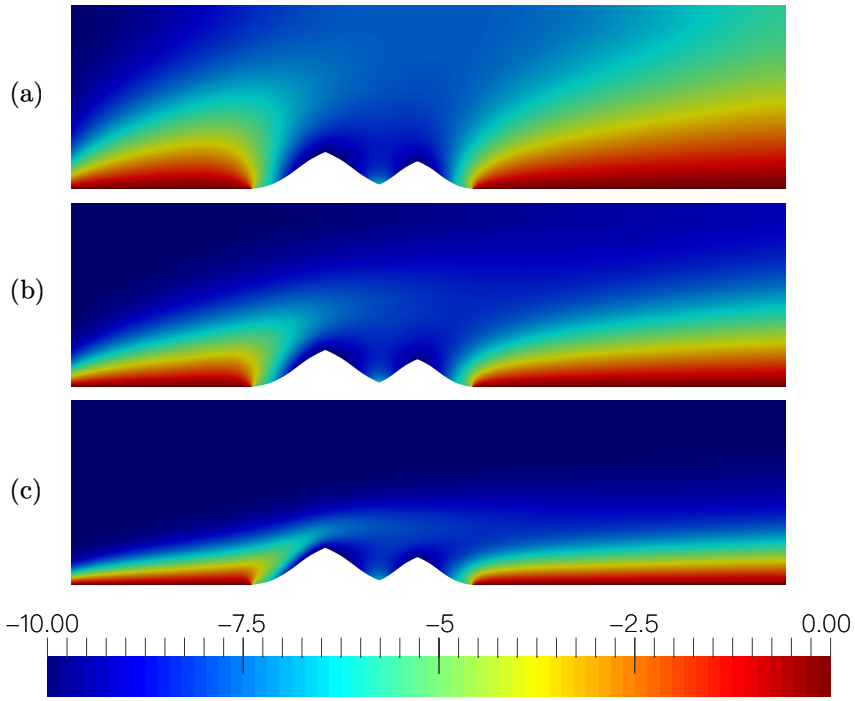

Figure 5.28: Temperature fields for hills with a dimensionless characteristic length of 0.2 for (a) Re = 10, (b) Re = 40, and (c) Re = 200.

5.4 Fourth scenario

For this scenario the velocity, pressure, and temperature fields are set to 0 at all points in the domain. The wind profile (5.1) is imposed at the inlet, where the vertical velocity component v is set to zero $v = 0$, which will also be set to zero for the entire domain and the temperature profile (5.2) is set. At the top wall, symmetry boundary conditions are imposed, setting the velocity and temperature gradients to zero $v = \partial u/\partial y = \partial T/\partial y = 0$. At the outlet, the pressure, velocity gradient and temperature gradient are set to zero $v = p = \partial u/\partial x = \partial T/\partial x = 0$. Finally, at the hills surface, the no-slip condition will be imposed $u = v = 0$ as well as the temperature profile (5.2).

The computational domains will change, but before describing their properties, it is necessary to show what the data collection process was like.

The data [23] to create the physical domain is based on [data, processing] services provided by the OpenTopography Facility with support from the National Science Foundation under NSF Award Numbers 1833703, 1833643, and 1833632. This airborne laser swath mapping data was acquired in support of collaborative research by members of the U.S. Geological Survey (USGS) and the National Aeronautics and Space Administration (NASA), with funding provided by NASA's Earth Surface and Interior Focus Area. The data were acquired and processed by TerraPoint, LLC under contract to NASA's Stennis Space Center. The data are in the public domain with no restrictions on their use.

These data belong to the Western Rainier Seismic Zone, adjacent to Mount Rainier, in Pierce County, Washington, United States. All dataset covers approximately 325 km^2 and includes approximately a billion data points. Point density is approximately 2 pts/m^2.

The dataset [23] used in the present work is shown in Figure 5.29 and contains 30,984,850 points with a point density of 2.40 pts/m^2. It covers the world from 1333.026 Km to 1345.962 Km, left to right, and -42.582 km to -30.870 km from bottom to top, which corresponds to a region of 12.936 km wide by 11.712 km high near of Niesson Creek in Washington. These coordinate values are relative to the origin of the dataset's coordinate reference system (CRS) that identifies a particular coordinate reference system: UTM zone 12N. In this case, the CRS code that corresponds to the study area would be EPSG: 2926. The latitude, longitude, and altitude data is provided by OpenTopography in a GeoTIFF file that contains the latitude and longitude information in a row-column format and the altitude information in a raster band. Each pixel in the dataset shown in Figure 5.29 associates an altitude value.

To read the data from the altitude raster, a Python script was written using a Python package called Rasterio [10]. The script allows the user to save the latitude or longitude along with the altitude in a DAT, CSV, or TXT format. Another Python script was written to generate a GEO file, which is the extension of Gmsh's scripting language. Gmsh [9] is an open-source finite element mesh generator with a built-in CAD engine and post-processor that has been employed in the present work to generate the meshes. Once the GEO script is run in Gmsh, an MSH file is generated containing the domain information about the cells and the nodes.

The mesh obtained as an MSH file must be imported into Python, but in such a way that the Fenics [18] environment is able to read it. This can be accomplished by converting MSH files to XML files via a Fenics command. Finally, an XML file containing all the domain information will be called from the *navier_stokes_boussinesq* Python file, which outputs an XDMF file that can be visualized in ParaView [1]. This workflow can be summarized in the diagram shown in Figure 5.30.

Two different rows will be taken from the dataset shown in Figure 5.29 to create two physical domains with different altitude irregularities but with the same dimensionless characteristic length. The data will be rescaled to adapt it to the company's requirements, which are cases with dimensionless characteristic length, corresponding to 1 km. The first row is represented as the red line in Figure 5.29 and corresponds to the data that is 8 km from the top reference: -30.870 Km, and the second row is represented as the blue line in Figure 5.29 and is 11 km from the same top reference. Imported altitude points in Gmsh have been smoothed by using a spline adjustment in Python to remove noise from the dataset. The results are shown in Figure 5.31, where the noise has been removed as can be seen.

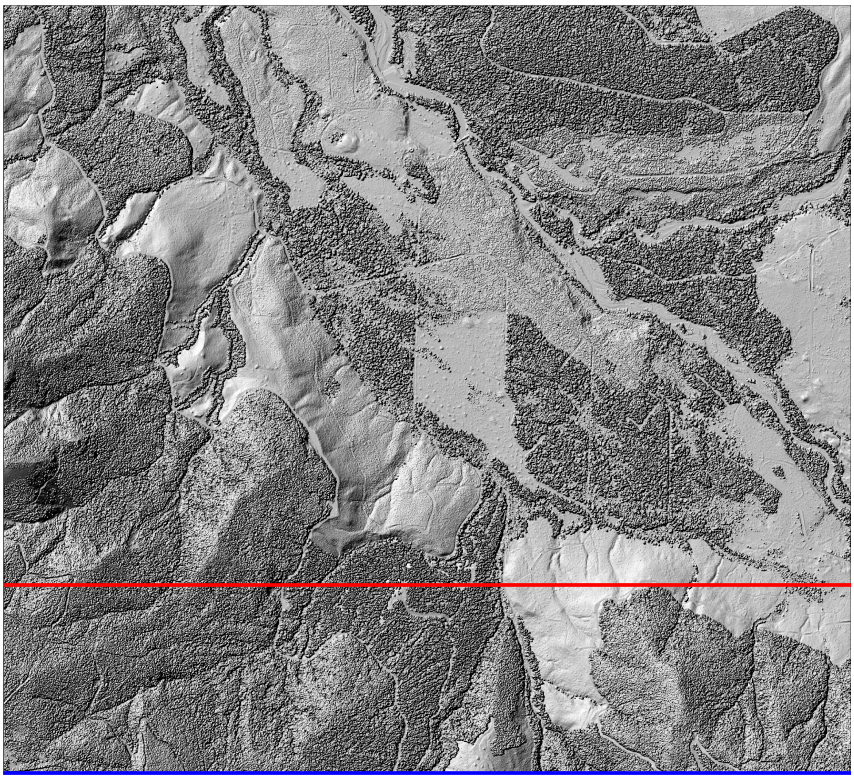

Figure 5.29: Dataset [23] of a zone near Niesson Creek in Washington, United States.

The resulting computational domains can be shown in Figures 5.32 and 5.33, hereafter referred to as Topography 1 and Topography 2 respectively. The left side of the green line shown in the Figures indicates the part of the solution to be discarded to avoid spurious phenomena in the graphic representation, which are produced due to the truncation of the computational domain and the interaction of the boundary conditions at the inlet with the rest of the computational domain. Both domains have a dimensionless height of 1 and a dimensionless characteristic length of 0.2, corresponding to 5 km and 1 km respectively. The dimensionless width is 2.75 for the first one and 1.59 for the second one, which corresponds to 13.75 km and 7.95 km respectively.

The first grid in Figure 5.32 is made up of 264,820 elements and 133,436 nodes while the second grid in Figure 5.33 is made up of 838,661 elements and 421,138 nodes. The meshes size on the bottom wall surface was 0.0005 and this size of the elements gradually varied to 0.006 in the rest of the domain.

The iterative method was carried out using a tolerance of $\epsilon = 10^{-5}$ as the stopping criterion, with a maximum number of iterations of 20 and a final dimensionless time of 15 with a time step of 0.1.

5.4.1 Scenario results and discussion

The velocity, pressure and temperature fields were calculated for a Reynolds number of Re = 10, Re = 40, Re = 200 and Re = 2000 for Topography 1 and Topography 2.

In the case of Topography 1, Figure 5.34 shows the result of the velocity field for 10 and 40, while Figure 5.35 shows the result for 200 and 2000. Laminar behavior can be seen in the Figures and how the thickness of the boundary layer decreases as the Reynolds number increases. For the Reynolds 2000 case in Figure 5.35, where the viscous forces have decreased considerably can be noticed that the boundary

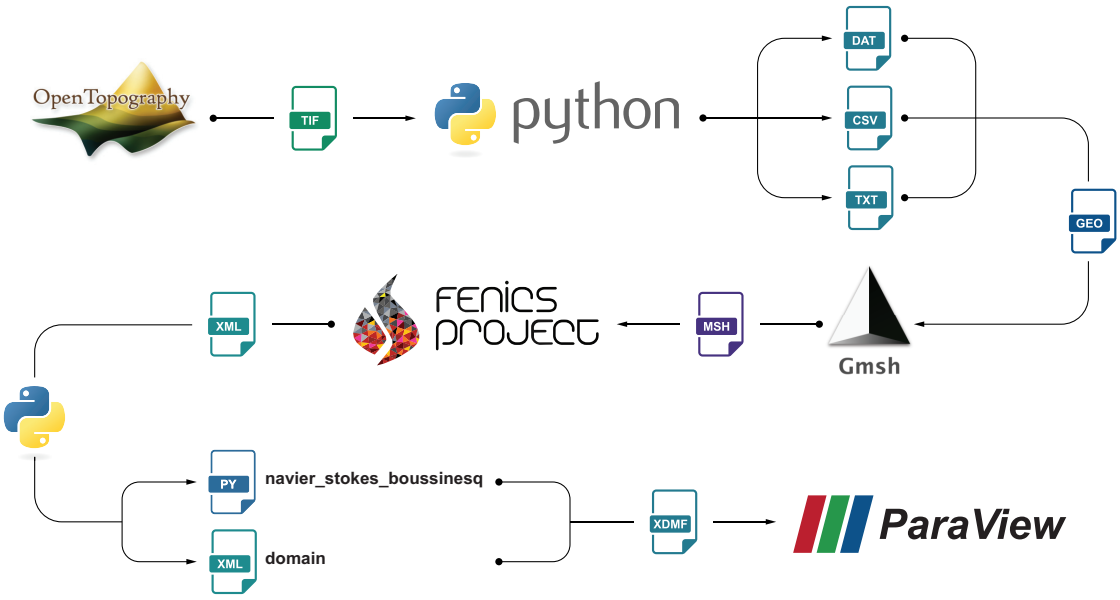

Figure 5.30: Workflow for computing the velocity, pressure, and temperature fields in a given domain.

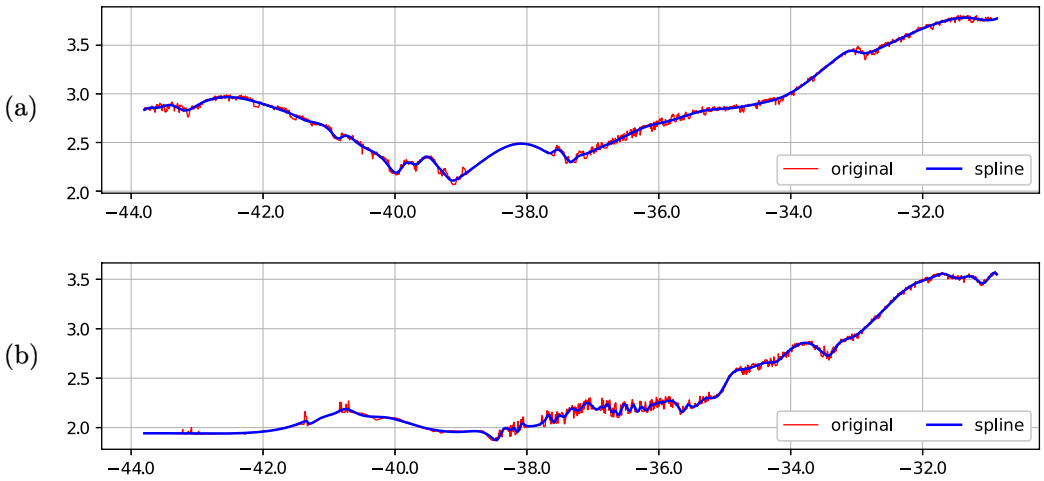

Figure 5.31: Raw and smoothed data in (km) corresponding to rows represented as the (a) blue and (b) red line in Figure 5.29 from the dataset [23].

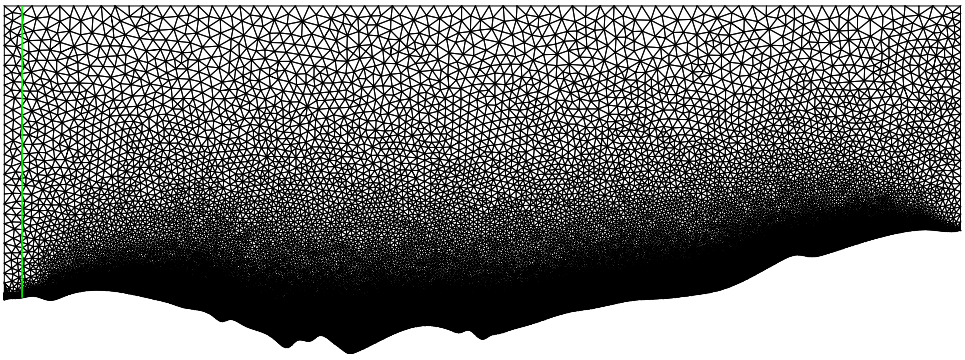

Figure 5.32: View of the grid resulting from taking the first row.

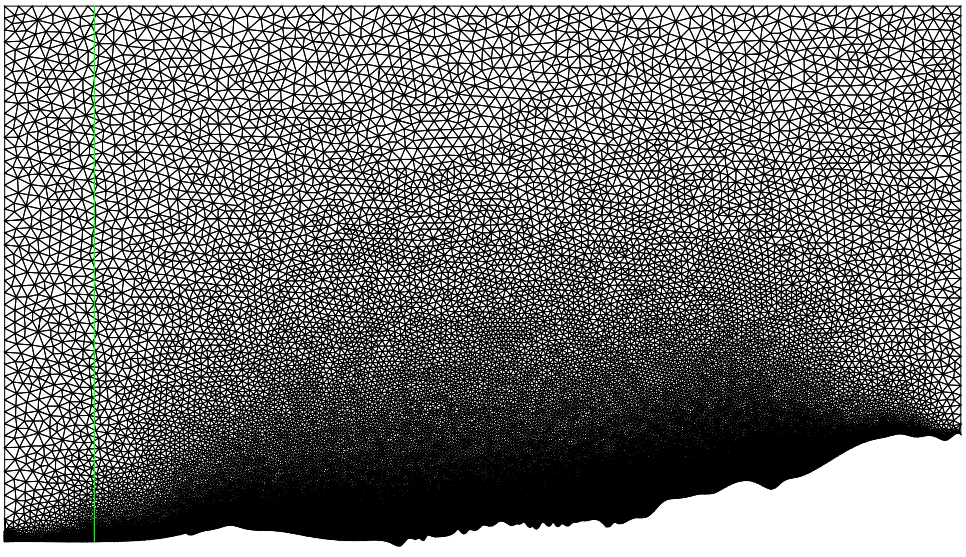

Figure 5.33: View of the grid resulting from taking the second row.

layer is correctly solved as a result of the good mesh shown in Figure 5.32.

The pressure field results can be seen in Figure 5.36 for a pressure field of 10 and 40, while Figure 5.37 shows the result for 200 and 2000. These figures show how the pressure is highest at the inlet and gradually decreases to zero once the outlet is reached. Furthermore, stagnation areas are visible on the surface of the lower wall of the physical domain, which are caused by the irregularity of the wall, as well as the Reynolds number imposed. It can be also noticed a decrease in the pressure field at the inlet as the Reynolds number increases.

Figure 5.38 shows the result of the temperature field for 10 and 40, while Figure 5.39 shows the result for 200 and 2000. It can be seen how the low-temperature part of the profile at the inlet cannot reach the output with a low Reynolds number, while for a higher number of Reynolds, the temperature profile begins to appear completely downstream. These results can be compared with previous in Figures 5.18 and 5.21, where the bottom wall was a horizontal line. In these cases, the temperature profile on the lower wall can be better appreciated due to domain irregularities in that area. It can be seen how the highest temperature coincides with the lowest point of the domain, which corresponds to the standard temperature of the sea level.

In the case of Topography 2, Figure 5.40 shows the result of the velocity field for 10 and 40, while Figure 5.41 shows the result for 200 and 2000. The same behavior is obtained as that observed in Topography 1, but now for a domain that has decreased in length by half. Although the irregularities of the domain have increased on the bottom wall of the physical domain, a laminar behavior can be seen in the Figures and how the thickness of the boundary layer decreases as the Reynolds number increases. For the $\mathrm{Re} = 2000$ case in Figure 5.41, where the viscous forces have decreased considerably can be noticed that the boundary layer is correctly solved as a result of the good mesh shown in Figure 5.33.

Figure 5.42 shows the result of the pressure field for 10 and 40, while Figure 5.43 shows the result for 200 and 2000. Similar results are obtained to those shown in Figures 5.36 and 5.37. In this case, stagnation areas are more predominant on the surface of the lower wall of the physical domain due to their irregularities. It can be seen how the stagnation areas decrease as the Reynolds number increases.

Figure 5.44 shows the result of the temperature field for 10 and 40, while Figure 5.45 shows the result for 200 and 2000. The same behavior is obtained as that observed in Topography 1. But now that the domain has halved its length, it can be seen more clearly how the higher temperature produced by the points near the inlet are able to reach the outlet due to thermal convection and the high Reynolds number, as can be seen for the $\mathrm{Re} = 2000$ case in Figure 5.45.

Taking into account that the air has a mass density of $\rho = 1.22$ Kg/m^3, dynamic viscosity of 1.78×10^{-5} Kg/m $\cdot$ s, and the characteristic length of the physical domain is 1000 m; the velocity u_r for a Reynolds number of $\mathrm{Re} = 10$, $\mathrm{Re} = 40$, $\mathrm{Re} = 200$ and $\mathrm{Re} = 2000$ would be 1.45×10^{-7}, 5.83×10^{-7}, 2.91×10^{-6}, and 2.91×10^{-5} m/s respectively. Pressure and temperature were defined as a dimensionless variable as shown in expressions (2.7). Therefore, a dimensionless value of zero for the pressure corresponds to the current atmospheric pressure. The dimensionless value of the temperature will depend on the temperature profile taken. If the profile in the study is the one shown in Figure 5.13, then the standard sea level temperature corresponds to 1, while if the selected profile is the one shown in Figure 5.22, the standard temperature of the sea level corresponds to zero.

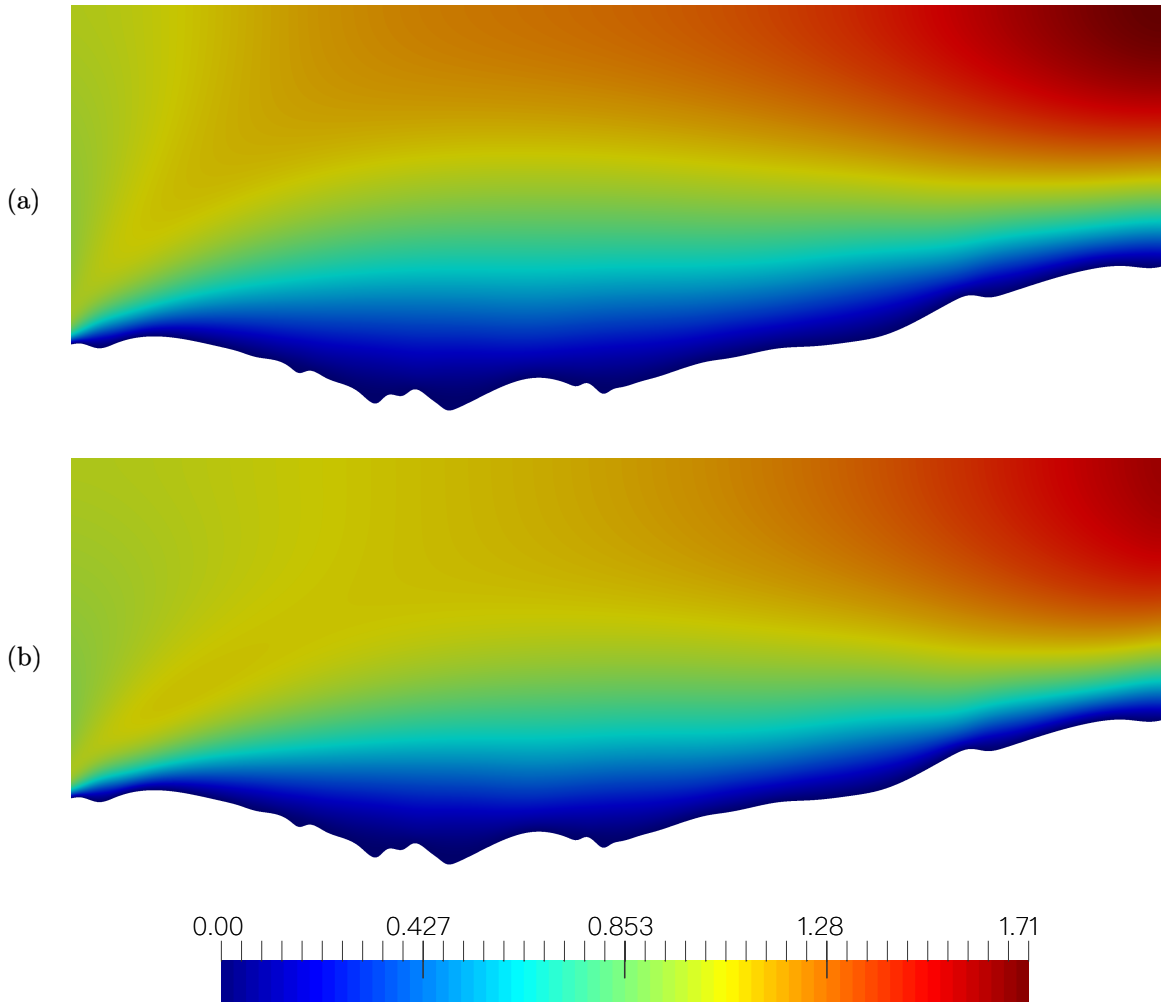

Figure 5.34: Velocity fields belonging to Topography 1 for (a) Re = 10 and (b) Re = 40.

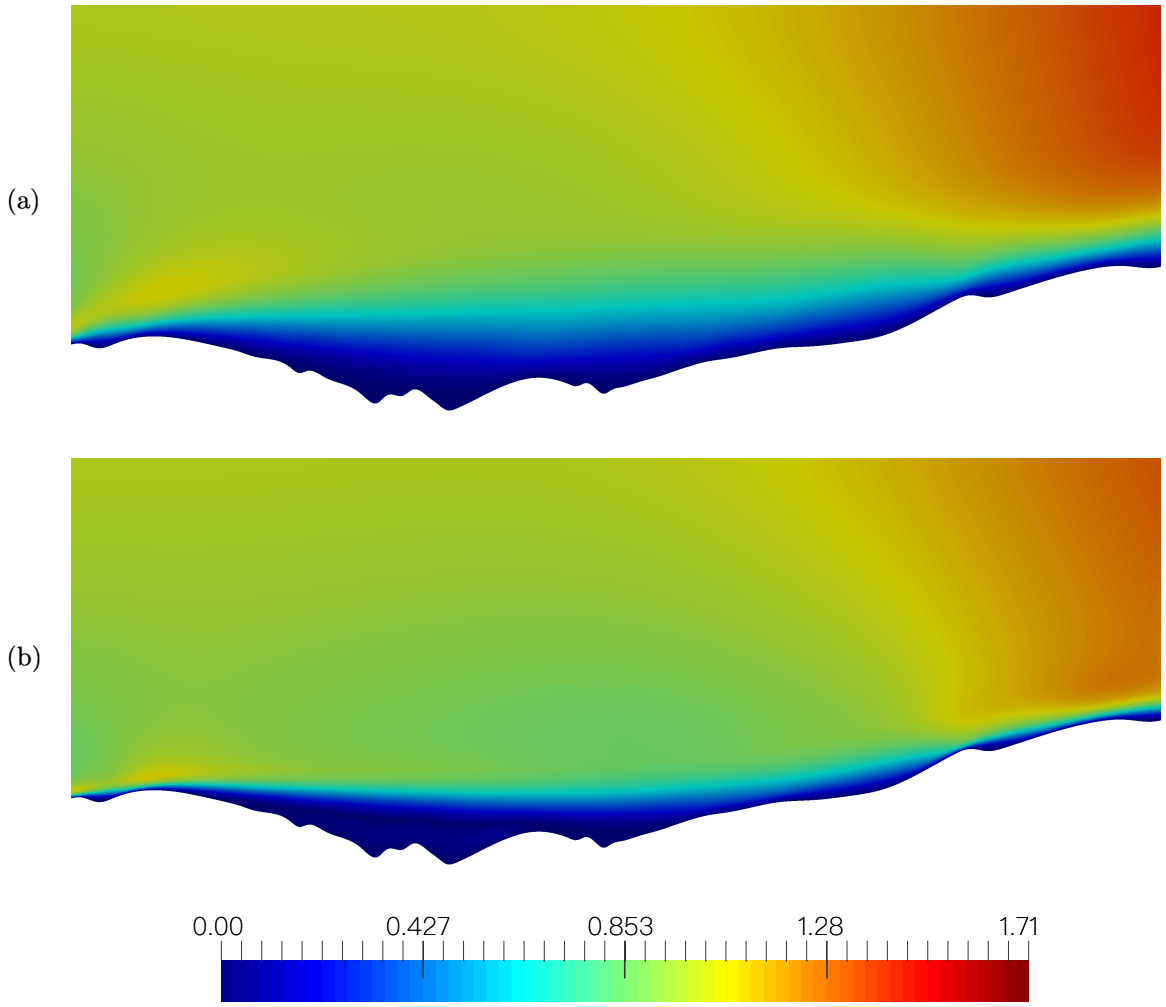

Figure 5.35: Velocity fields belonging to Topography 1 for (a) Re = 200 and (b) Re = 2000.

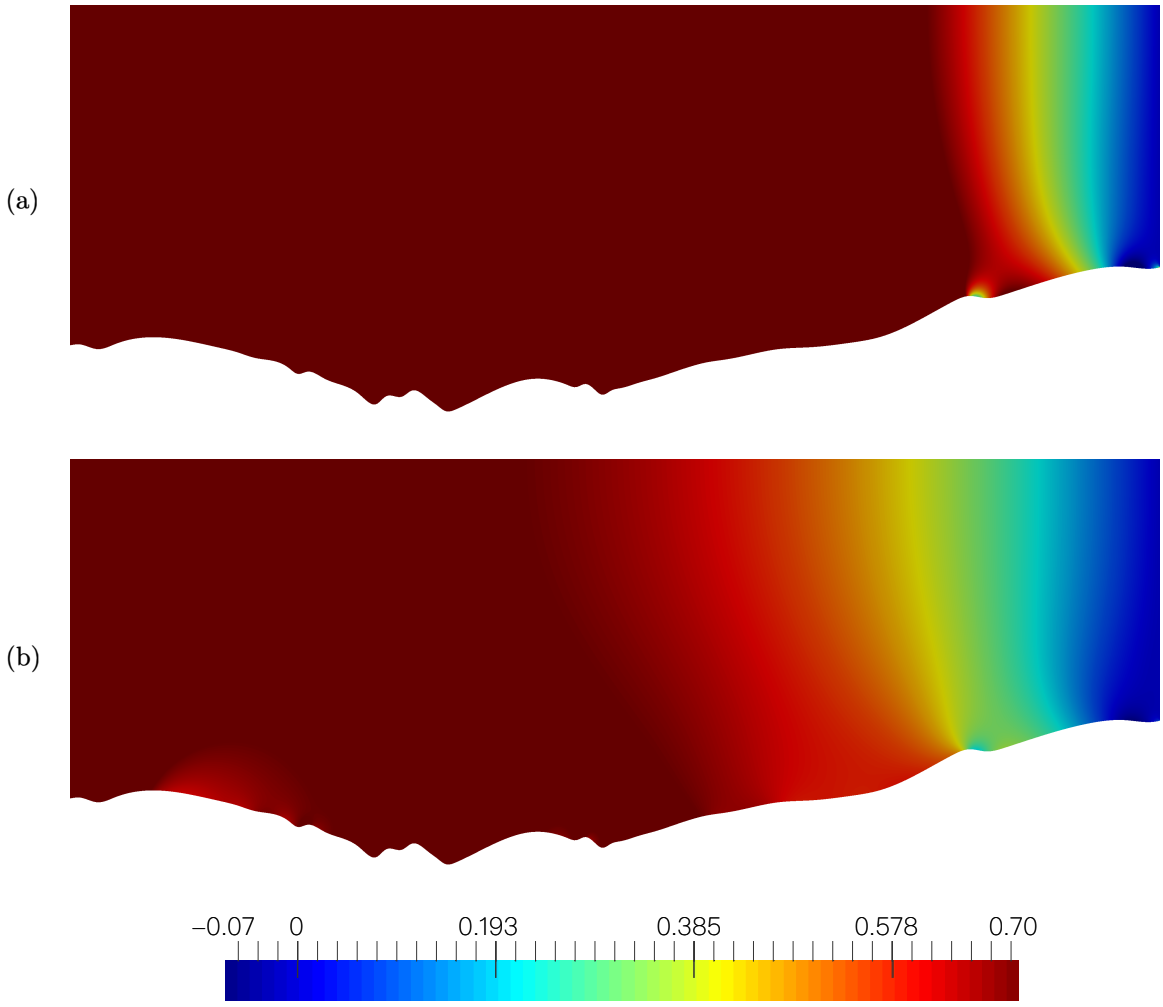

Figure 5.36: Pressure fields belonging to Topography 1 for (a) Re = 10 and (b) Re = 40.

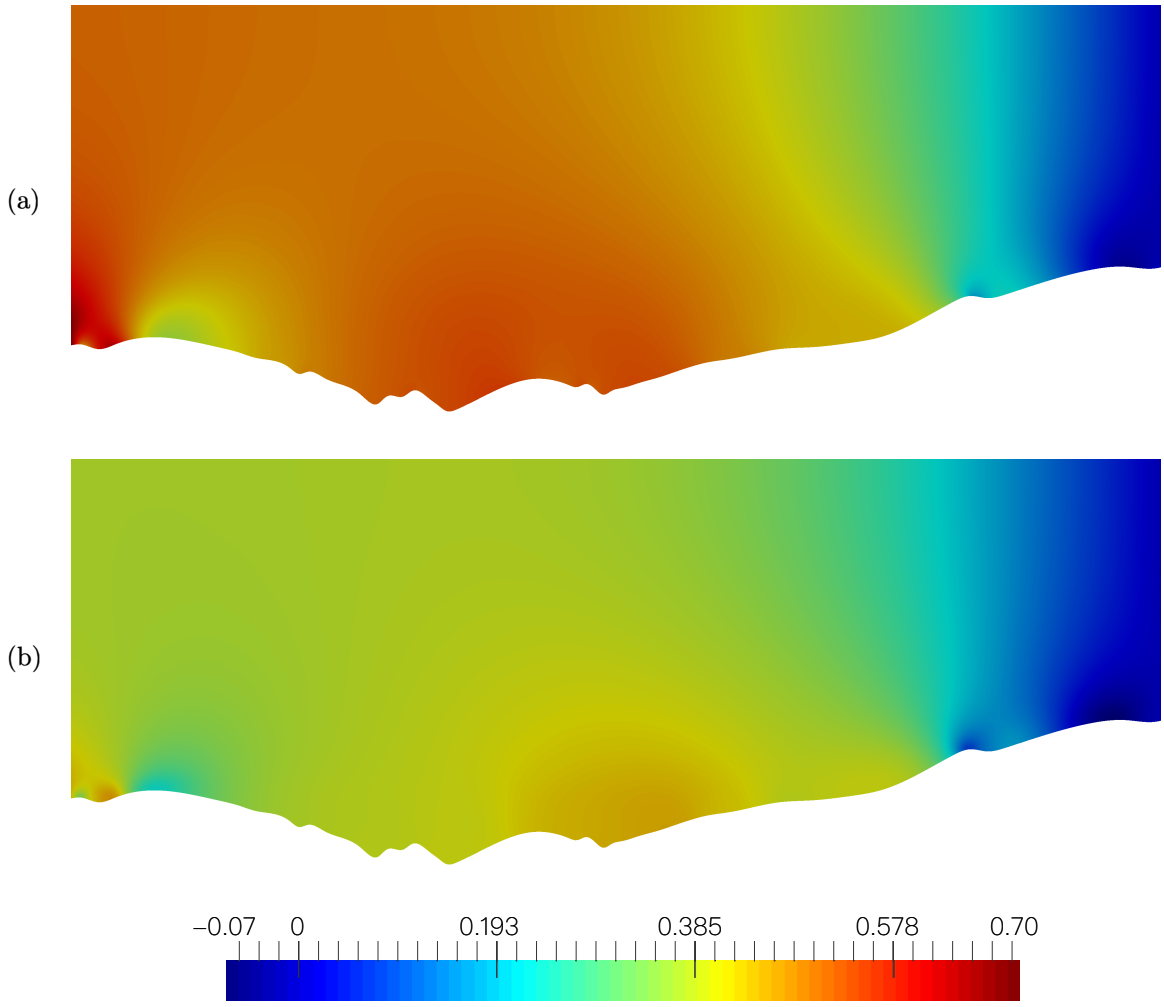

Figure 5.37: Pressure fields belonging to Topography 1 for (a) Re = 200 and (b) Re = 2000.

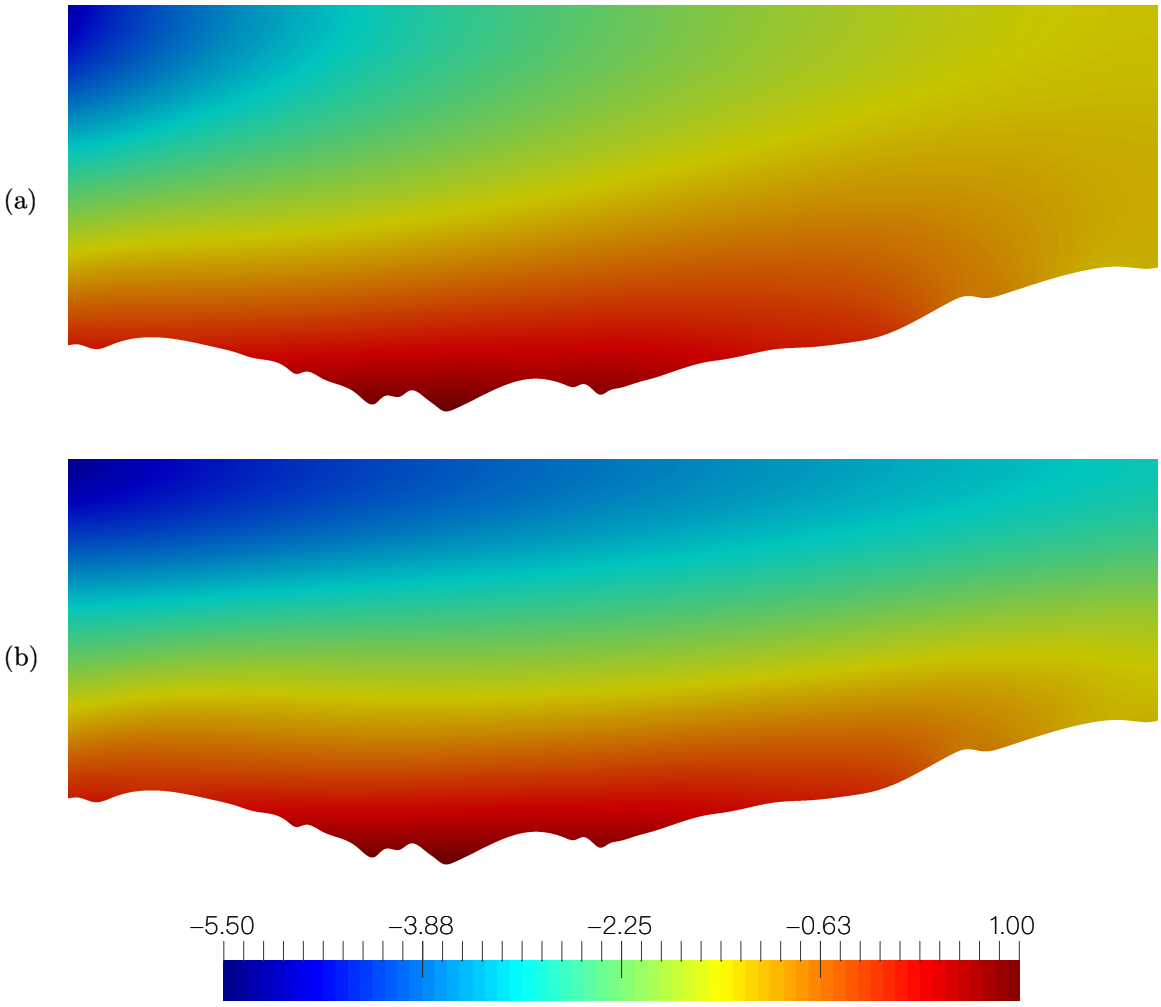

Figure 5.38: Temperature fields belonging to Topography 1 for (a) Re = 10 and (b) Re = 40.

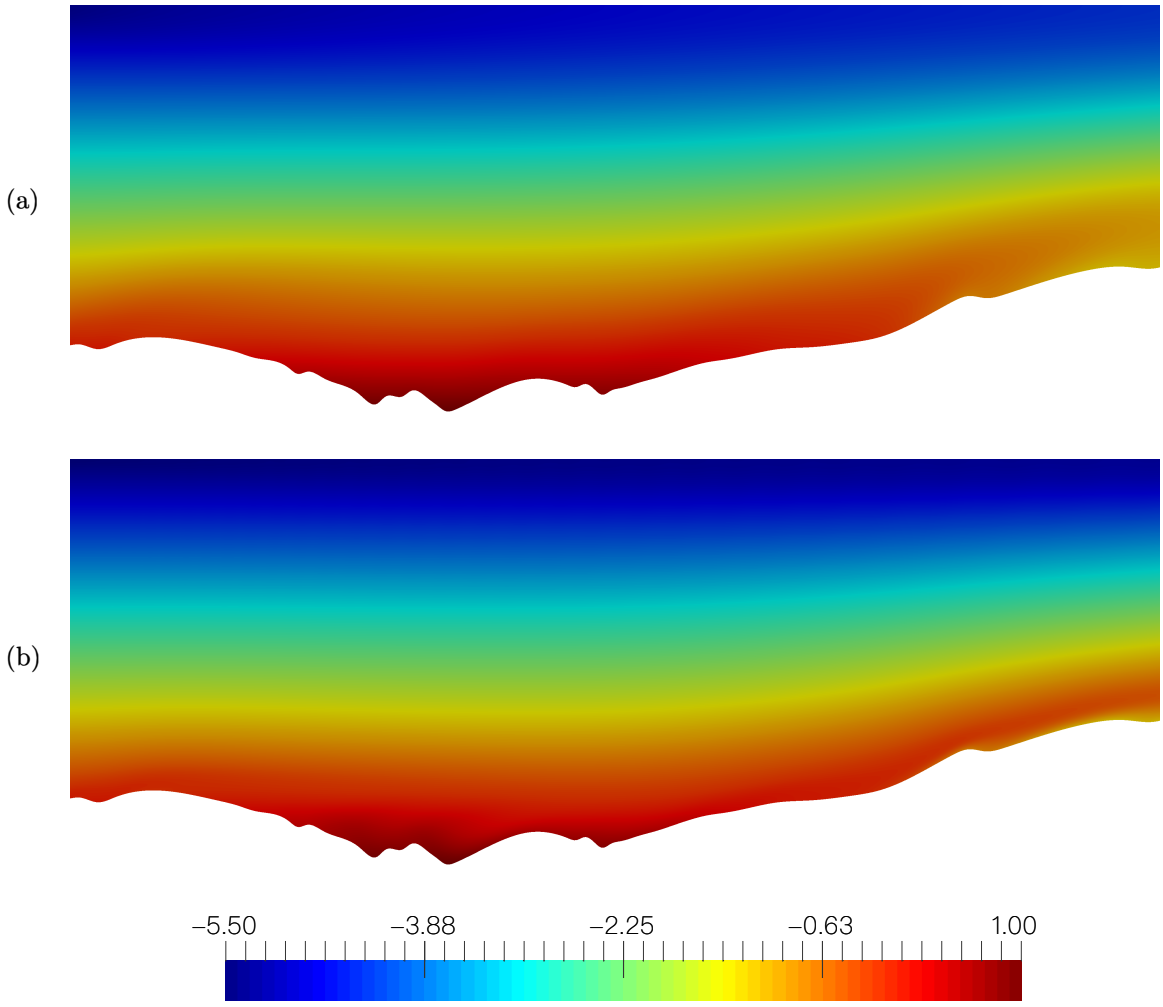

Figure 5.39: Temperature fields belonging to Topography 1 for (a) Re = 200 and (b) Re = 2000.

(a)

(b)

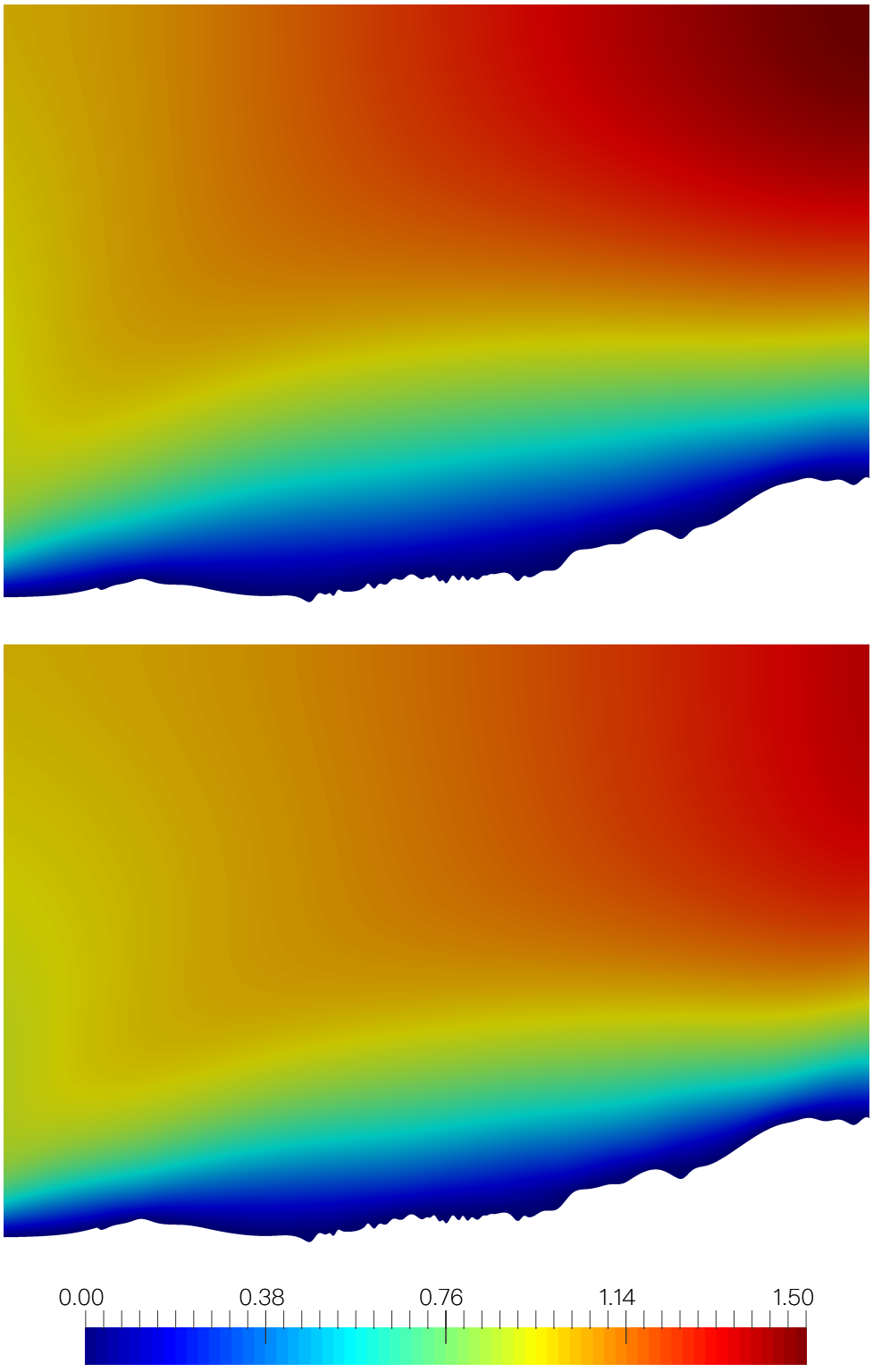

Figure 5.40: Velocity fields belonging to Topography 2 for (a) Re = 10 and (b) Re = 40.

(a)

(b)

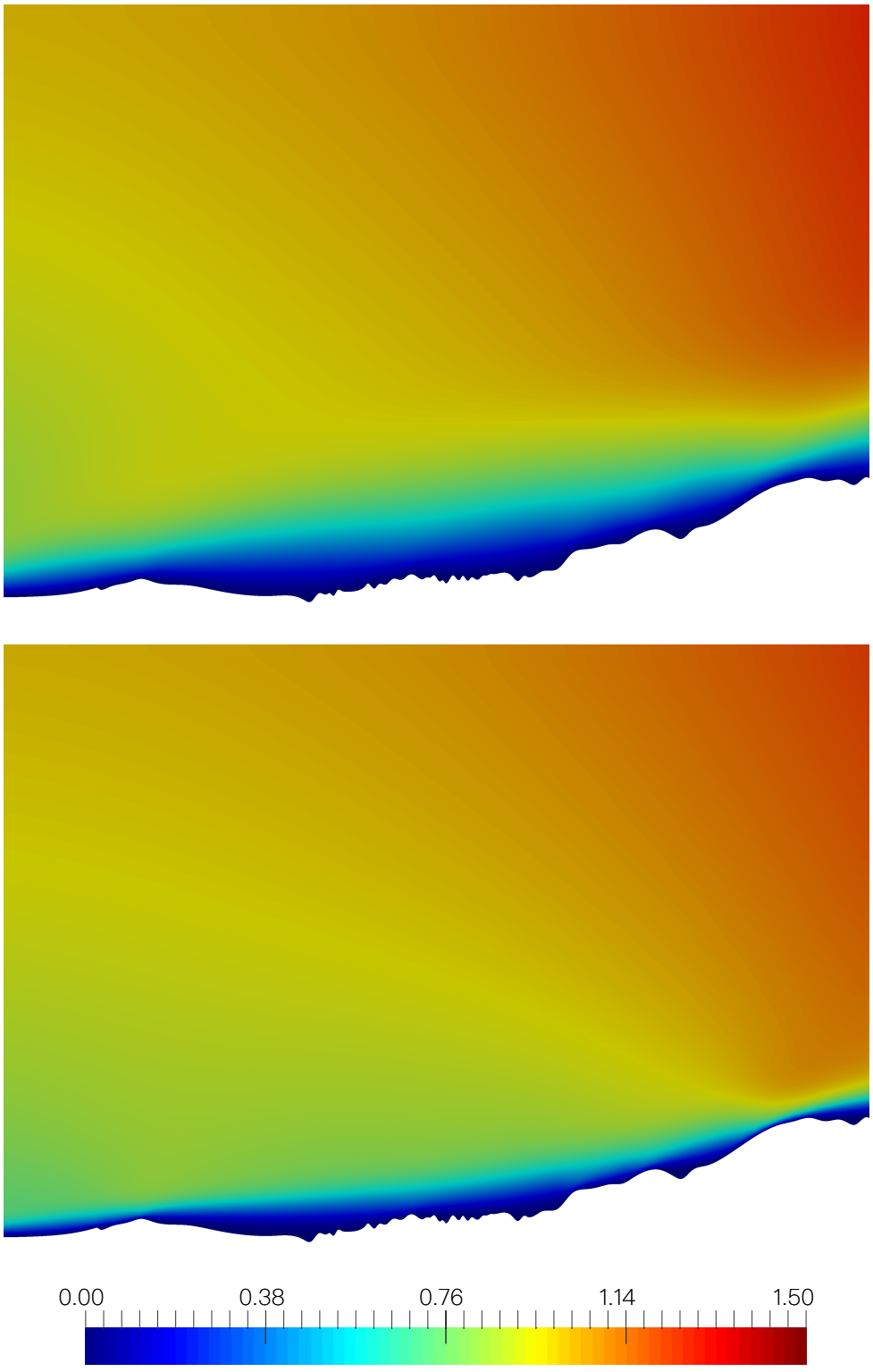

Figure 5.41: Velocity fields belonging to Topography 2 for (a) Re = 200 and (b) Re = 2000.

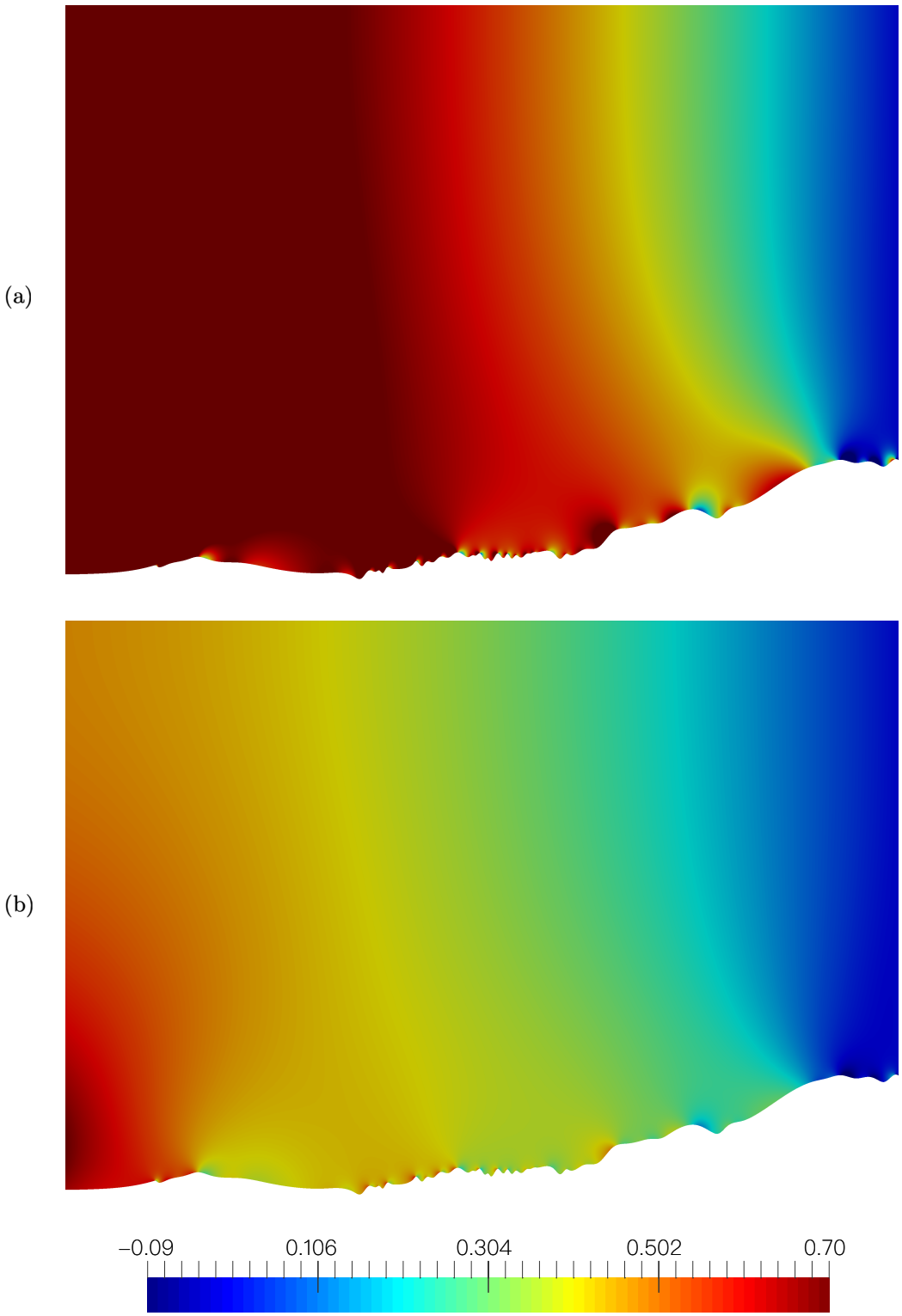

Figure 5.42: Pressure fields belonging to Topography 2 for (a) Re = 10 and (b) Re = 40.

(a)

(b)

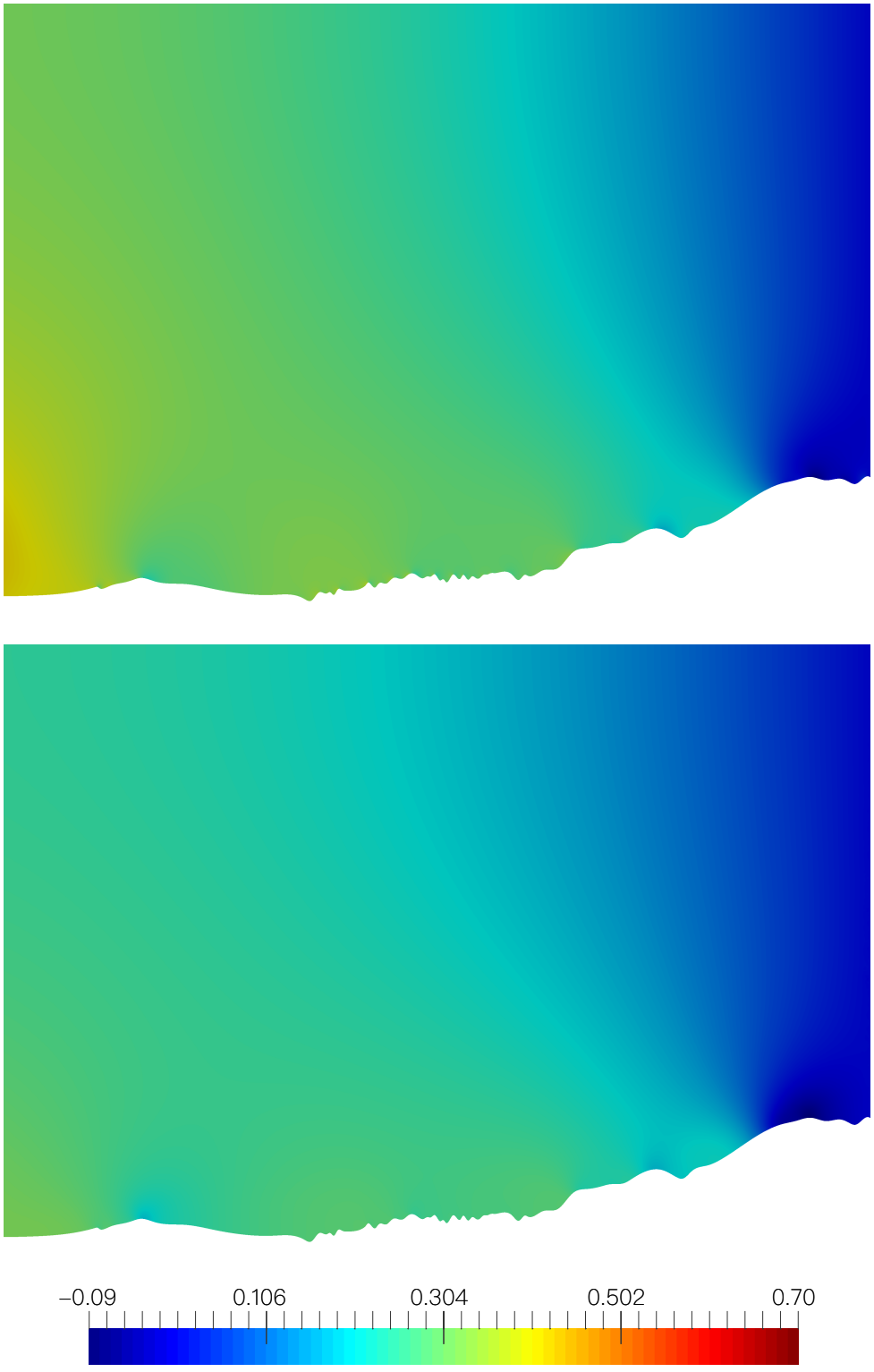

Figure 5.43: Pressure fields belonging to Topography 2 for (a) Re = 200 and (b) Re = 2000.

(a)

(b)

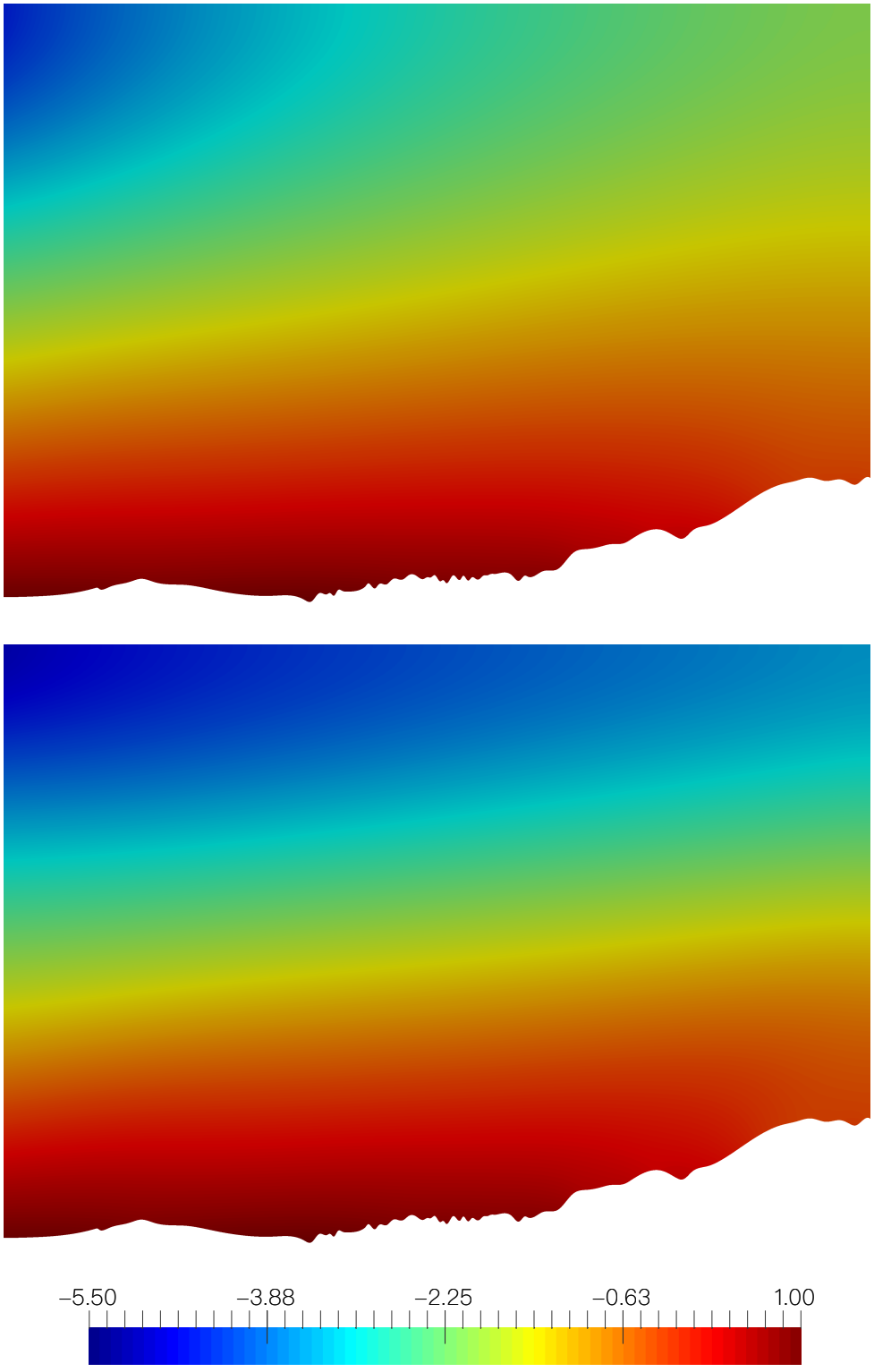

Figure 5.44: Temperature fields belonging to Topography 2 for (a) Re = 10 and (b) Re = 40.

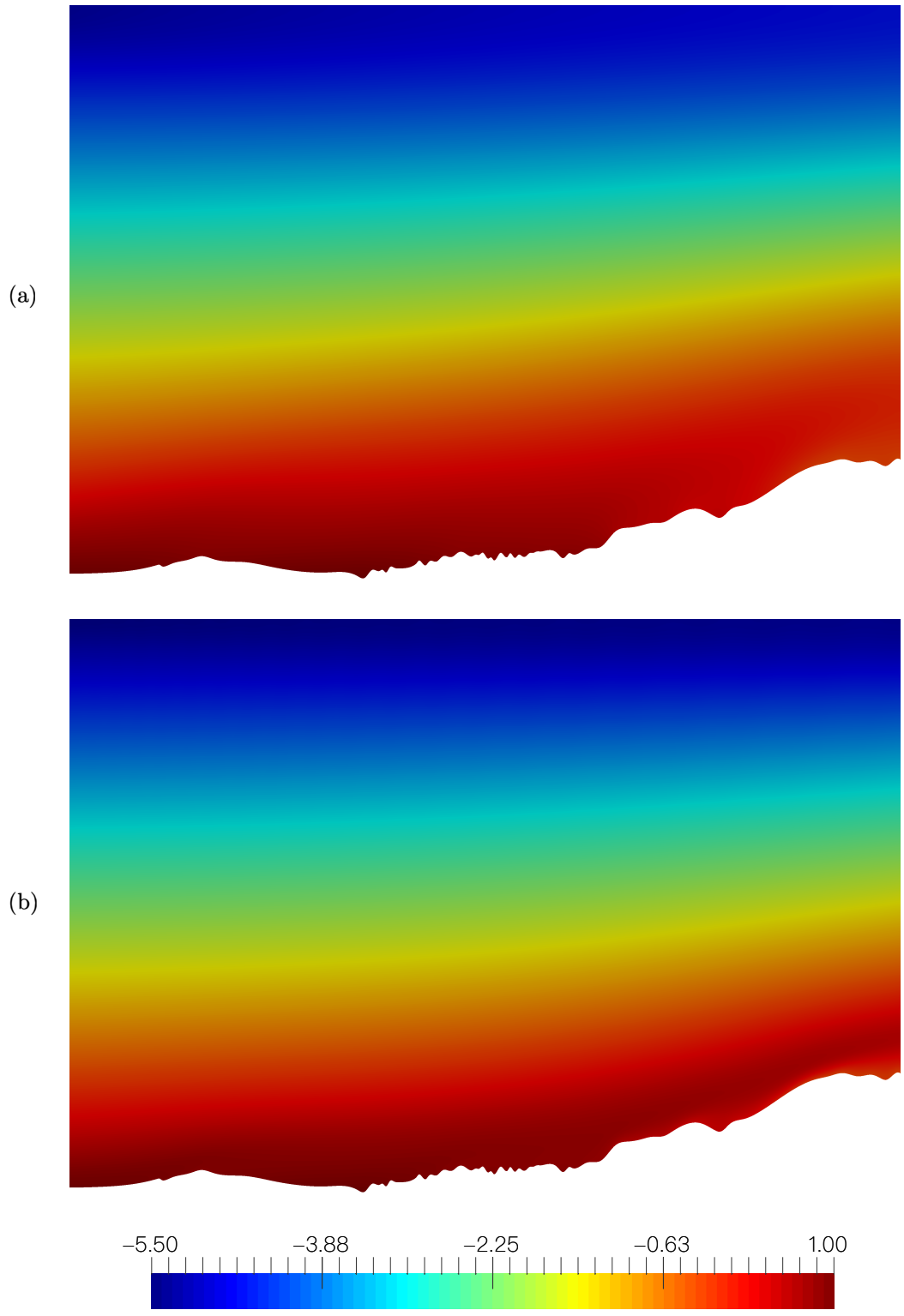

Figure 5.45: Temperature fields belonging to Topography 2 for (a) Re = 200 and (b) Re = 2000.

Chapter 6

Conclusions

In the present work, the modeling and reconstruction of temperature, wind, and atmospheric pressure fields in a two-dimensional area were accomplished by a model for laminar and incompressible flow with heat transfer. The Navier-Stokes and energy equations were solved using a FEniCS based Taylor-Hood finite element discretization based on Prof. Jaroslav Hron implementation [12], and the Gmsh finite element mesh generator. Different studies were considered for the two-dimensional case and one for the three-dimensional case to validate the finite element solution of the model. The validation focused on known problems studied by many authors, showing our results an excellent agreement with previous works.

A workflow was provided to the company, where the steps to extract spatial data from a GeoTIFF file to generate the physical domain where the calculations will be performed were explained, as well as the Python scripts that contain the model to solve the velocity, the pressure and temperature fields. From a GeoTIFF dataset provided by OpenTopography, more complex domains were created and the model was calculated for more realistic scenarios. As shown in these results, the model is only valid for very low mean velocity in the case of a characteristic length of 1 km or 500 m. Therefore, the model could be more useful for domains with a not so high characteristic length, as the results shown in the first scenario. Although the workflow was applied for the two-dimensional case, it follows the same steps for the three-dimensional case with the difference that the Python script for the three-dimensional case, which has also been provided to Microflown Technologies, must be used instead of the one used for the two-dimensional case, as well as a set of three-dimensional data to generate the 3D domain needs to be employed. As a suggestion for additional work, a turbulence model for high wind velocities and characteristic length would be required, such as the $k - \epsilon$ model considering that more powerful computational requirements would be needed to correctly solve a three-dimensional turbulent model.

Bibliography

[1] James Ahrens, Berk Geveci, and Charles Law. Paraview: An end-user tool for large data visualization. *The visualization handbook*, 717, 2005.

[2] Sabah FH Alhamdi and Sean CC Bailey. Universality of local dissipation scales in turbulent boundary layer flows with and without free-stream turbulence. *Physics of Fluids*, 29(11):115103, 2017.

[3] H Asan. Natural convection in an annulus between two isothermal concentric square ducts. *International communications in heat and mass transfer*, 27(3):367–376, 2000.

[4] Mohammed Bakkali and Yasunobu Ashie. Rans modelling for local climates, energy use and comfort predictions in cities. In *Intelligent Environments (Workshops)*, pages 76–88, 2019.

[5] G Biswas and Sandip Sarkar. Effect of thermal buoyancy on vortex shedding past a circular cylinder in cross-flow at low reynolds numbers. *International Journal of Heat and Mass Transfer*, 52(7-8):1897–1912, 2009.

[6] Alexander N Brooks and Thomas JR Hughes. Streamline upwind/petrov-galerkin formulations for convection dominated flows with particular emphasis on the incompressible navier-stokes equations. *Computer methods in applied mechanics and engineering*, 32(1-3):199–259, 1982.

[7] Tuncer Cebeci, Jian P Shao, Fassi Kafyeke, and Eric Laurendeau. *Computational fluid dynamics for engineers*. Springer Berlin Heidelberg, 2005.

[8] Ramon Codina. *A finite element model for incompressible flow problems*. Universitat Politecnica de Catalunya, 1992.

[9] Christophe Geuzaine and Jean-François Remacle. Gmsh: A 3-d finite element mesh generator with built-in pre-and post-processing facilities. *International journal for numerical methods in engineering*, 79(11):1309–1331, 2009.

[10] Sean Gillies et al. Rasterio: geospatial raster i/o for Python programmers. `https://github.com/mapbox/rasterio/`, 2013.

[11] Vivette Girault and Pierre-Arnaud Raviart. *Finite element methods for Navier-Stokes equations: theory and algorithms*, volume 5. Springer Science & Business Media, 2012.

[12] Jaroslav Hron. Navier-stokes + convection-difusion. `https://www.karlin.mff.cuni.cz/~hron/fenics-tutorial/stokes/doc.html#navier-stokes-convection-difusion`, 2015.

[13] SA Hsu, Eric A Meindl, and David B Gilhousen. Determining the power-law wind-profile exponent under near-neutral stability conditions at sea. *Journal of Applied Meteorology*, 33(6):757–765, 1994.

[14] Salam Hadi Hussain and Ahmed Kadhim Hussein. Numerical investigation of natural convection phenomena in a uniformly heated circular cylinder immersed in square enclosure filled with air at different vertical locations. *International Communications in Heat and Mass Transfer*, 37(8):1115–1126, 2010.

[15] BS Kim, DS Lee, MY Ha, and HS Yoon. A numerical study of natural convection in a square enclosure with a circular cylinder at different vertical locations. *International journal of heat and mass transfer*, 51(7-8):1888–1906, 2008.

[16] Mats G Larson and Fredrik Bengzon. *The finite element method: theory, implementation, and applications*, volume 10. Springer Science & Business Media, 2013.

[17] Ben Q Li. *Discontinuous finite elements in fluid dynamics and heat transfer*. Springer Science & Business Media, 2006.

[18] Anders Logg, Kent-Andre Mardal, and Garth Wells. *Automated solution of differential equations by the finite element method: The FEniCS book*, volume 84. Springer Science & Business Media, 2012.

[19] John E. Oliver. *Standard atmosphere*, pages 801–803. Springer US, Boston, MA, 1987.

[20] Li Qin, Shi Liu, Teng Long, Muhammad Ali Shahzad, H Inaki Schlaberg, and Song An Yan. Wind field reconstruction using dimension-reduction of cfd data with experimental validation. *Energy*, 151:272–288, 2018.

[21] Lixia Qu, Christoffer Norberg, Lars Davidson, Shia-Hui Peng, and Fujun Wang. Quantitative numerical analysis of flow past a circular cylinder at reynolds number between 50 and 200. *Journal of Fluids and Structures*, 39:347–370, 2013.

[22] Wei Qu and Yong Liang. Stability and convergence of the crank-nicolson scheme for a class of variable-coefficient tempered fractional diffusion equations. *Advances in Difference Equations*, 2017(1):108, 2017.

[23] Rainier. West rainier seismic zone, wa and airborne lidar, distributed by opentopography. `https://doi.org/10.5069/G9CC0XMC`, 2005.

[24] BN Rajani, A Kandasamy, and Sekhar Majumdar. Numerical simulation of laminar flow past a circular cylinder. *Applied Mathematical Modelling*, 33(3):1228–1247, 2009.

[25] Héctor Redal, Jaime Carpio, Pablo A García-Salaberri, and Marcos Vera. Dynamfluid: Development and validation of a new gui-based cfd tool for the analysis of incompressible non-isothermal flows. *Processes*, 7(11):777, 2019.

[26] Niles Ritter, Mike Ruth, Brett Borup Grissom, George Galang, John Haller, Gary Stephenson, Steve Covington, Tim Nagy, Jamie Moyers, Jim Stickley, et al. Geotiff format specification geotiff revision 1.0. *SPOT Image Corp*, 1, 2000.

[27] Hideo Takami and Herbert B Keller. Steady two-dimensional viscous flow of an incompressible fluid past a circular cylinder. *The Physics of Fluids*, 12(12):II–51, 1969.

[28] Frank M White and Isla Corfield. *Viscous fluid flow*, volume 3. McGraw-Hill New York, 2006.

[29] FENG Xinlong and HE Yinnian. Convergence of the crank-nicolson/newton scheme for nonlinear parabolic problem. *Acta Mathematica Scientia*, 36(1):124–138, 2016.